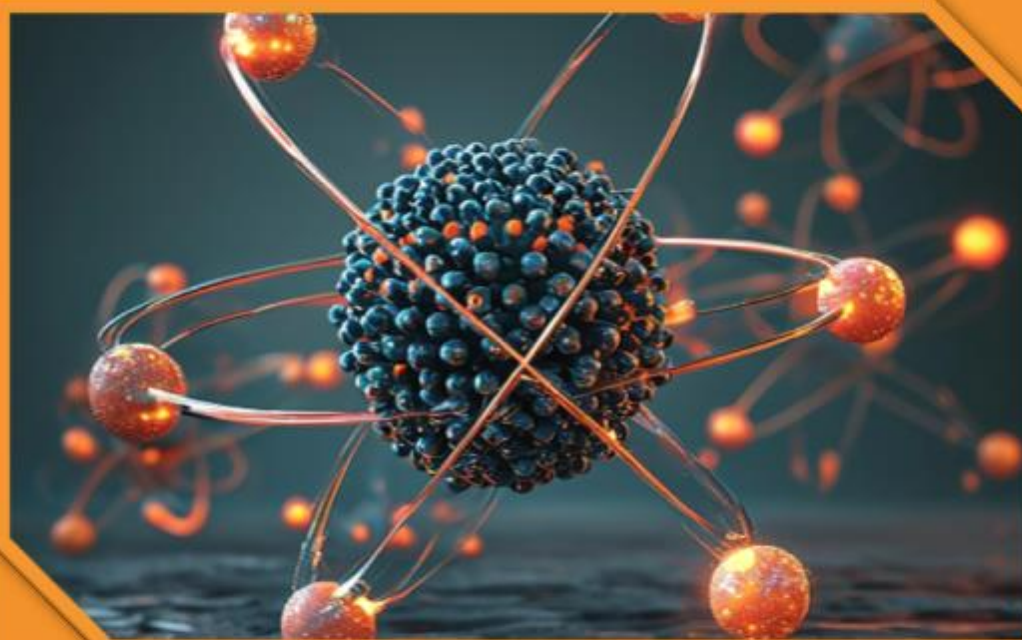




All Sciences Academy



CONTEMPORARY RESEARCH IN NATURAL SCIENCE AND MATHEMATICS

CONTEMPORARY RESEARCH IN NATURAL SCIENCE AND MATHEMATICS

Editor
Prof. Dr. Canan ÖZDEMİR





Contemporary Research in Natural Science and Mathematics
Prof. Dr. Canan ÖZDEMİR

Design: All Sciences Academy Design

Published Date: August 2025

Publisher's Certification Number: 72273

ISBN: 978-625-5794-06-2

© All Sciences Academy

www.allsciencesacademy.com

allsciencesacademy@gmail.com

CONTENT

1. Chapter	5
Theoretical Degradation Mechanism of Selected Molecules Used for Therapeutic Purposes in Two Phases by DFT Method <i>Bahar EREN, Yelda YALÇIN GÜRKAN</i>	
2. Chapter	28
Synthesis And Characterization Of Nickel Orthoborate Nanopowders <i>Eray SÖNMEZER, Ayşe MORKAN</i>	
3. Chapter	43
Investigation of Sterilization Technology-A Brief Overview <i>Neşe KEKLİKÇİOĞLU ÇAKMAK</i>	
4. Chapter	52
Çinko Ftalosiyanın Yüklü MCM-41 Heterojen Katalizörü ile Çevre Dostu Koşullarda 1,4-Naftakinon Eldesi <i>Yaşar GÖK, Recep ERDEM</i>	
5. Chapter	65
A Functional-Analytic Approach to HyersUlam Stability of n-th Order Differential Equations <i>Emel Biçer</i>	
6. Chapter	75
Harnessing Plasmonic Resonance: Metal Nanoparticles in Modern Technology <i>İlhan CANDAN, Sezai ASUBAY</i>	
7. Chapter	90
Stability of Impulsive Systems with Generalized Piecewise Constant Argument: A Lyapunov-Based Approach <i>Duygu ARUĞASLAN ÇİNÇİN</i>	

8. Chapter	103
Electronic Structure, Reactivity, and Intermolecular Interaction Studies on a Coumarin Derivative via DFT and Hirshfeld Surface Analysis	
<i>Sevgi KANSIZ, Okan ŞİMŞEK</i>	
9. Chapter	116
A Photocatalytic Investigation of Benzyl Alcohol Oxidation	
<i>Osman Tayyar ARLI, Halil Zeki GÖK</i>	
10. Chapter	127
On Non-Newtonian Closed Metric Intervals	
<i>Ahmadou DIALLO, Birsen SAĞIR</i>	
11. Chapter	140
A Complete Quadrangle-Based Approach to Complete (k,4)-Arcs in PG(2,4)	
<i>Elif ALTINTAŞ KAHRİMAN, Ayşe BAYAR</i>	
12. Chapter	152
Preparation of Electrodes through Pseudocapacitors, Electric double layer capacitance and Hybrid Supercapacitor Systems	
<i>Murat ATES</i>	
13. Chapter	164
On the Study of Parabolas in the Maximum Plane	
<i>Süheyla EKMEKÇİ</i>	

Theoretical Degradation Mechanism of Selected Molecules Used for Therapeutic Purposes in Two Phases by DFT Method

Bahar EREN¹

Yelda YALÇIN GÜRKAN²

1- Dr.; Tekirdağ Namık Kemal Üniversitesi Rektörlük.
beren@nku.edu.tr ORCID No: 0000-0002-1523-274X

2- Prof. Dr.; Tekirdağ Namık Kemal Üniversitesi Fen Edebiyat Fakültesi Kimya Bölümü.
yyalcin@nku.edu.tr ORCID No: 0000-0002-8621-2025

ABSTRACT

In this study, three molecules, namely Piroxicam (PR), Escitalopram (ES) and Verapamil HCl (V), were selected from three different groups as anti-inflammatory, antidepressant and calcium channel blocker, respectively, and were theoretically examined according to their pharmaceutical effects, that is, treatment groups and sites of action. Selected molecules are used for therapeutic purposes, but their fate in nature is not taken seriously when they are eliminated from the body or become waste when they are not used. The aim of this study is to theoretically elucidate the fate of both the main molecule and its hydroxylated fragments in nature as they enter the natural cycle as a result of mixing with wastewater.

Geometric optimizations of the fragments were made on the DFT/B3LYP/6-31G(d) basic set of Quantum Mechanical Density Functional Theory (DFT) to theoretically determine all possible reaction pathways of the selected molecules with the OH radical. Since the reactions of molecules with the OH radical are important for both water purification and atmospheric chemistry, calculations were carried out both in the gas phase and in the water phase by modeling with CPCM in the COSMO (conductor-like screening solvation model) solvent model.

The Mulliken charges of the molecules, the electronegative atoms in the molecule and the arrangement of the atoms around them, stable double bonds, weak bonds at the end of the molecule, calculated energies, bond lengths and bond angles between atoms were examined; and these data helped us to select all the fragments that would determine the degradation mechanism. As a result of examining the molecules in terms of their reaction with OH radicals in air or water, the fragmentation reaction of each molecule was written, starting from the low-energy fragments, and their fate in nature was determined.

Keywords – DFT, Anti-Inflammatory, Antidepressant, And Calcium Channel Blocker

INTRODUCTION

A pharmaceutical product, also known as a drug, is a finished dosage form containing active ingredients, usually formulated with one or more excipients, used in humans for disease prevention, diagnosis, treatment, or the correction or modification of a function. Every drug consists of two main parts: the active ingredient(s) and the base. The active ingredient is the component of the drug that provides diagnostic and therapeutic purposes. The drug may contain one or more active ingredients. Pharmaceutical raw materials are either natural or synthetic. Drugs derived from plant, animal, organic, or inorganic mineral sources, microorganisms, and DNA

recombination are natural; those synthesized in laboratories using chemical methods are synthetic. The base is the carrier material. Bases in pharmaceutical formulations are a single substance or a mixture of several substances. Of course, there are also excipients added to pharmaceutical formulations as flavour, odour, and palatability enhancers, which help the medication be easily measured and administered, and which help it work quickly and as intended (Baron et al, 2023; Alenghat and Golan, 2017; Bade et al, 2010).

Pharmaceutical products, colloquially known as drugs, are used for therapeutic purposes, but their fate in nature, whether excreted from the body or unused and becoming waste, is often neglected. This study aimed to shed light on this uncertainty and was conducted under theoretical conditions, without harming nature or the environment. The molecules were selected from three different groups based on their pharmaceutical effects, that is, their therapeutic groups and sites of action: anti-inflammatory, antidepressant, and calcium channel blocker, to provide examples for each group. In this study, three of the five molecules we investigated in our scientific research project titled "Investigation of Theoretical Degradation Mechanisms of Selected Pharmaceutical Product Active Ingredients", respectively, Piroxicam (PR), Escitalopram (ES) and Verapamil HCl (V), were selected from, three different groups as anti-inflammatory, antidepressant and calcium channel blocker, according to their pharmaceutical effects, in other words, treatment groups and sites of action (Ommaty, 2006).

Piroxicam (PR) active ingredient, trade name Cycladol or Felden, is a nonsteroidal anti-inflammatory drug used to relieve symptoms of primary dysmenorrhea, postoperative pain, rheumatoid arthritis, and osteoarthritis. Rheumatoid arthritis (RA) has traditionally been defined as a chronic, inflammatory autoimmune disorder that causes the immune system to attack the joints. It is a disabling and painful inflammatory condition that can lead to significant loss of mobility due to pain and joint wear. The disease is often systemic, affecting many extra-articular tissues in the body, such as the skin, blood vessels, heart, lungs, and muscles. PR can cause mild elevations in serum aminotransferases and, in rare cases, lead to clinically apparent acute liver injury, which can be serious and even fatal. Overdose symptoms are drowsiness, nausea, stomach pain or vomiting (Camlibel et al., 2019). PR with IUPAC name, (8E)-8-[hydroxy-(pyridin-2-ylamino) methylidene]-9-methyl-10,10-dioxo-10 λ 6-thia-9-azabicyclo [4.4.0] deca-1,3,5-trien-7-one, chemical formula C₁₅H₁₃N₃O₄S, molecular weight 331.348 g/mol has a half-life of 30-86 hours (O'Neil, 2013).

Escitalopram (ES), commonly known as Cipralex and Citoles, is an antidepressant in the selective serotonin reuptake inhibitor (SSRI) class. It is approved for the treatment of depression and anxiety in adults over the age of 12. The medication is also used in the treatment of panic disorder, social

anxiety disorder, and obsessive-compulsive disorder. It is effective in reducing the symptoms of premenstrual syndrome. Like other SSRIs, escitalopram has a negative effect on sexual function. There is evidence that SSRIs may cause an increase in suicidal ideation, but this increase is not statistically significant. Headache, nausea, somnolence, insomnia, and ejaculatory dysfunction are common side effects. Taking escitalopram in larger amounts than needed causes relatively minor adverse effects such as tachycardia (Clayton et al., 2006). The IUPAC name of ES is (1S)-1- [3-(dimethyl amino) propyl]-1-(4-fluorophenyl)-3H-2-benzofuran-5-carbonitrile and the molecular formula is $C_{20}H_{21}FN_2O$. The melting temperature of ES is 147-152°C, the half-life is 27-32 hours, and the molecular weight is 324.399 g/mol (O'Neil, 2013).

Isopitin, marketed as Verapamil HCl (V), is a calcium channel blocking agent widely used in the treatment of supraventricular tachyarrhythmias, angina (chest pain caused by insufficient blood flow to the heart), supraventricular tachycardia, pectoris, hypertrophic cardiomyopathy, and hypertension. It can also be used to prevent migraines and headaches. It is administered orally or by injection into a vein. Common side effects include headache, low blood pressure, nausea, and constipation. Other side effects include allergic reactions and muscle aches. It is not recommended in people with a slow heart rate or heart failure. It is believed to cause problems for the embryo if used during pregnancy (Bhatia et al., 2013). Its IUPAC name is 2-(3,4-dimethoxyphenyl)-5-[2-(3,4-dimethoxyphenyl) ethyl-methylamino]-2-propan-2-ylpentanenitrile, molecular formula is $C_{27}H_{38}N_2O_4$, molecular weight is 454.6 g/mol, it is a viscous, pale yellow oil structure and its water solubility is 83 mg/mL (O'Neil M.J., 2013; Haynes, 2014-2015).

The molecules to be studied are organic compounds. Recent studies indicate that organic pollutants are present in very low concentrations in water. Therefore, purifying drinking water of organic pollutants is crucial. Sunlight on Earth helps naturally purify water systems like lakes, rivers, and other water systems. Large organic molecules are broken down into smaller molecules by sunlight (Matthews et al. 1993; Verschueren 1996; Eren and Yalçın Gürkan, 2017).

Organic compounds undergo photolysis, reacting with OH radicals, and this reaction is the most predominant degradation reaction in the atmosphere. Biomolecules, which are hydroxyl scavengers at various rates, are specific detectors for hydroxyl radicals due to their hydroxylation capabilities. Any hydroxyl radical attack on an aromatic compound results in the formation of a hydroxylated product, and these newly formed products can be much more harmful than the original products at the beginning of the process, so monitoring these products is crucial. The OH radical acts as an electrophile in its reaction with any organic molecule and therefore readily binds to unsaturated bonds, whereas the O radical is a nucleophile and

therefore cannot interact with these bonds. If an aliphatic side chain is attached to an aromatic molecule, the OH radical prefers the aromatic ring for binding (Anbar et al., 1967; Buxton et al., 1988; Halliwell et al., 1998; Aschmann et al., 2005, 2010; Ashmann and Atkinson, 2006; Atkinson et al., 1998; Atkinson and Arey, 2003; Eren and Yalcin Gürkan, 2017).

The primary objective of this study is to monitor new products that may be more hazardous than the product initially released into the environment and to elucidate the degradation reaction. During the degradation reactions of organic pollutants, products that are more harmful than the main pollutants can be formed. Therefore, there is a great need to know the intermediate products in air and water treatment. The reactions that cause organic pollutants to disappear in the atmosphere are reactions with OH, NO₃ radicals, O₃, and Cl atoms. Among these radicals, the most active are reactions with OH radicals. Knowing the half-life of these substances in the troposphere is the most important factor providing information about whether they will be transported to the stratosphere (Eren and Yalcin Gürkan, 2021, 2022, 2023a, b).

MATERIALS AND METHODS

Theoretically, to determine all possible reaction pathways for the investigated molecules, geometric optimizations were performed using the DFT/B3LYP/6-31G(d) basis set of Quantum Mechanical Density Functional Theory (DFT), a method of electronic structure. For all fragments, energy values were calculated using the Gauss View 5.0.8 molecular representation program and the Gaussian 09 program for orbital calculations, and geometric optimizations were performed (Gaussian 09, 2009). The fragmentation reaction energy is affected by water molecules in the aqueous environment. In addition, geometry stretching in solutions is induced by H₂O. In other words, the presence of a dielectric medium such as H₂O causes relaxation of the solute-related geometry and has a stabilizing effect, reducing the energy for this mechanism (Eren and Yalcin Gürkan, 2017). Therefore, in this study, the CPCM in the COSMO (conductor-like screening solvation model) solvent model in the Gaussian 09 package was used to explain the solvent effect of H₂O on the energetics of the molecule + OH reaction (Gaussian 09, 2009).

The Gaussian 09 programs are the latest in the Gaussian series. They provide state-of-the-art capabilities for electronic structure modelling. Gaussian 09 is licensed for a wide range of computer systems. Gaussian 09 is a comprehensive program that includes molecular mechanics, semi-empirical, and ab initio methods. It offers a wide range of theory and basis set options for all three methods. The Gaussian 09 program allows the

calculation of atom and molecule energies, geometric optimizations, and calculation of vibrational frequencies, force constants, and dipole moments. Gauss View 5.0.8 is a graphical interface designed for creating input files and visualizing outputs for Gaussian package programs. Gauss View visualizes molecules, allowing us to rotate, move, and manipulate them as desired. It also easily prepares input files for even complex calculations. It allows us to graphically examine the results calculated by the Gaussian program. These results can include optimized molecular structures, molecular orbitals, electrostatic potential surfaces, atomic charges, IR, Raman, and NMR spectra, and normal mode animations based on vibrational frequencies (Gaussian 09, 2009).

RESULTS AND DISCUSSION

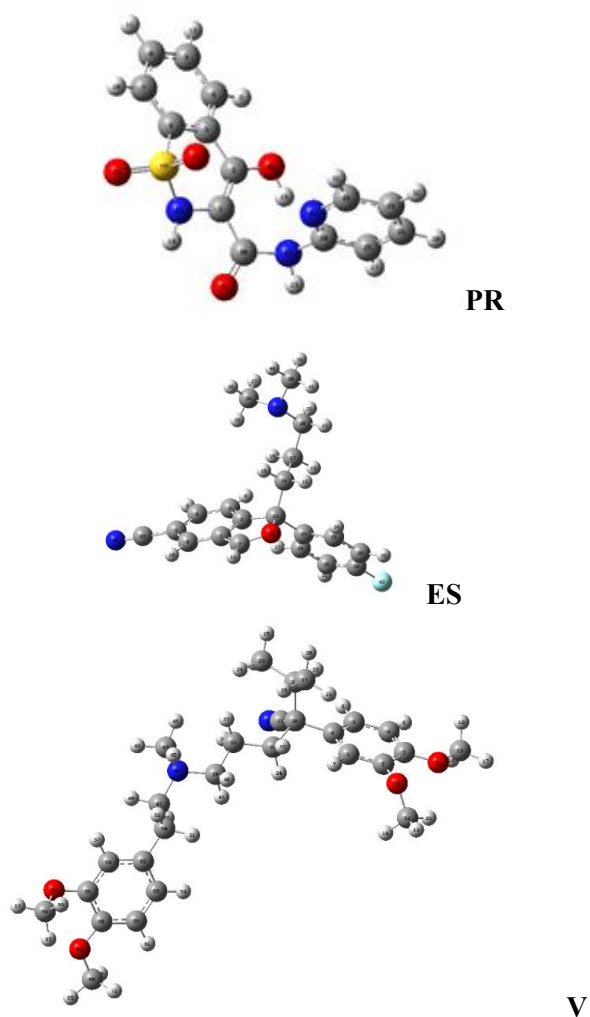
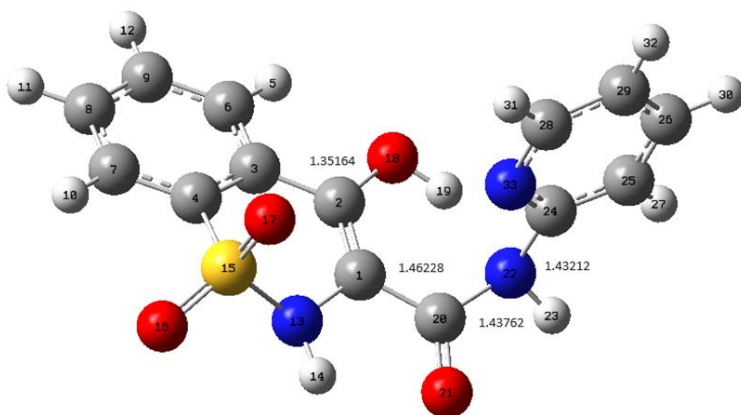
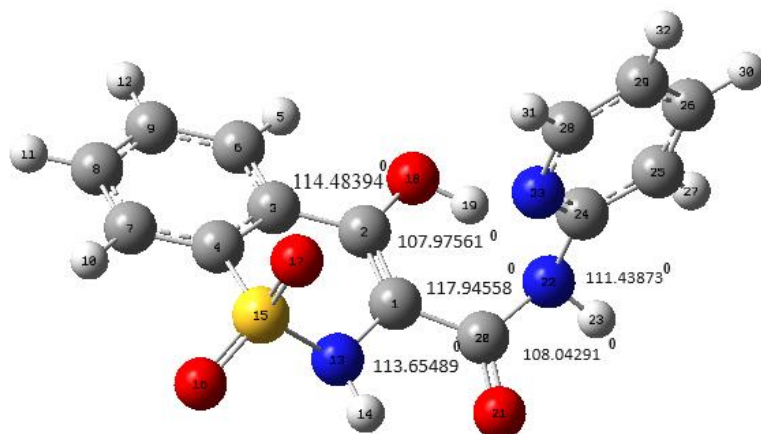


Figure 1: Geometric structure of PR, E, and V molecules optimized by the DFT method (C atom is represented in grey, O atom is represented in red, N atom is represented in dark blue, F atom is represented in blue, S atom is represented in yellow, and H atom is represented in white)



PR (a)



PR (b)

Figure 2: Bond lengths PR (a) and bond angles PR (b) between atoms in the PR molecule (C atom is represented in grey, O atom in red, N atom in dark blue, S atom in yellow and H atom in white)

Although it is predicted that the longest bond and widest bond angle will break first for any molecule, the determination of the fragmentation pathway is made by observing the energy values and environments of electronegative atoms. It should be noted that structures with double bonds or closed rings are more stable than others, and that if fragmentation occurs, the breakage from these stable structures will be the final stage (Eren and Yalcin Gürkan, 2023b).

Table 1: Bond lengths and bond angles between atoms in the PR molecule and Mulliken atom charges of the PR molecule

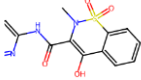
 PR	Bond lengths	(Å)	Bond angles	(°)	Mulliken atom charges
	C ₂₄ N ₂₂	1.43212	C₃C₂O₁₈	114.48394	C ₄ -0.217406
	C ₂₀ N ₂₂	1.43762	C ₂ O ₁₈ H ₁₉	107.97561	C ₆ -0.153878
	C₂₀C₂₁	1.46228	N ₁₃ C ₁ C ₂₀	113.65489	C ₇ -0.158379
	C ₂ O ₁₈	1.35164	N₂₂C₁C₂₀	117.94558	C ₈ -0.116532
			C₂₀N₂₂H₂₃	108.04291	C ₉ -0.128762
			C₂₄N₂₂H₂₃	111.43873	N ₁₃ -0.778460
					S ₁₅ 1.190085
					O₁₆ -0.517974
					O₁₇ -0.484478
					O₁₈ -0.647946
					O₂₁ -0.479692
					N₂₂ -0.745003
					C ₂₅ -0.169808
					C ₂₆ -0.098766
					C ₂₉ -0.146186
					N₃₃ -0.460291

Table 2: ΔE (energy), ΔH (enthalpy) and ΔG (Gipps free energy) values of the PR molecule and its fragments in the gas and water phases

(Au)	PR	PR1	PR2	PR3
ΔE	-1403.115563	-1156.104523	-1100.741683	-1025.537895
Gas phase ΔH	-1403.114619	-1156.103579	-1100.740739	-1025.536951
ΔG	-1403.181235	-1156.157405	-1100.792716	-1025.586550
Water phase	-1403.137181	-1156.124152	-1100.760342	-1025.553220
	-1403.136237	-1156.123208	-1100.759398	-1025.552275
	-1403.202549	-1156.177343	-1100.811954	-1025.601958
	PR4	PR5	PR6	PR7
	-987.424532	-912.221025	-1327.907680	-1080.896811
	-987.423587	-912.220081	-1327.906736	-1080.895867
	-987.471105	-912.265168	-1327.971661	-1080.948544
	-987.441817	-912.235735	-1327.928317	-1080.917087
	-987.440873	-912.234791	-1327.927373	-1080.916143
	-987.488356	-912.279847	-1327.992153	-1080.969517
	PR8	PR9	PR10	
	-416.862598	-303.536656	-248.191670	
	-416.861654	-303.535712	-248.190726	
	-416.902352	-303.571230	-248.223340	
	-416.872683	-303.544373	-248.196479	
	-416.871738	-303.543429	-248.195535	
	-416.912489	-303.578936	-248.228147	

The energy values of the possible reaction pathways for each studied molecule and all its fragments were calculated in both the gas phase and the water phase. Every fragment that could be formed by the interaction of the parent molecules with the OH radical was included in the study. The energy values calculated for each molecule are given in atomic mass units (Au) because the numbers after the decimal point are very close when converting the results to SI units, and the energy differences between the fragments are not easily observed.

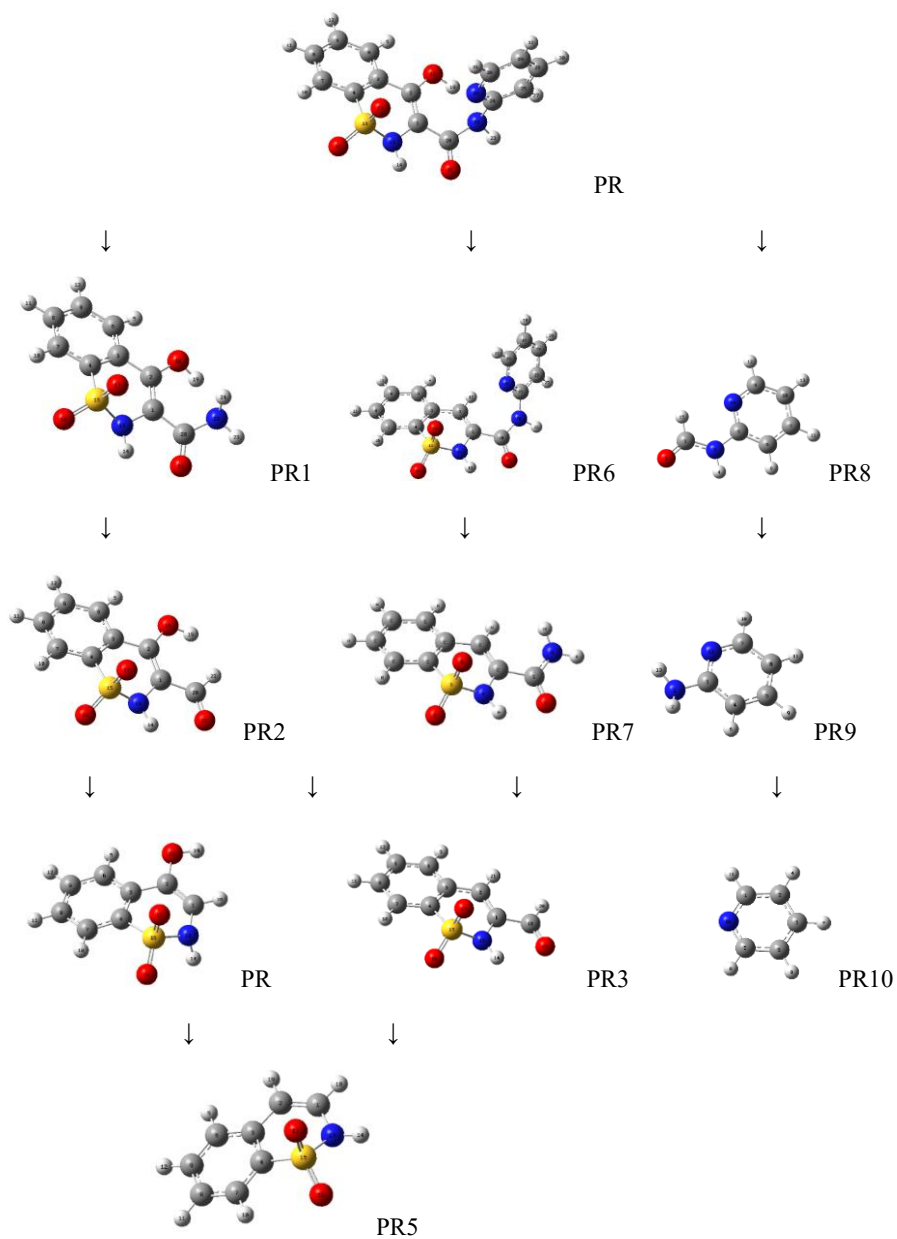
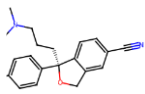


Figure 3: The degradation pathway (degradation mechanism) of the PR molecule (in the geometric structures of the PR molecule and all fragments optimized by the DFT method, the C atom is represented in grey, the O atom in red, the N atom in dark blue, the S atom in yellow, and the H atom in white)



16

Table 3: Bond lengths and bond angles between atoms in molecule ES and Mulliken atom charges of molecule ES



ES	Bond lengths	(Å)	Bond angles	(°)	Mulliken atom charges
	C ₃₈ N ₃₃	1.45725	C ₂₀ N ₃₃ C ₃₄	112.72454	C ₂ -0.097081
	C ₃₄ N ₃₃	1.45782	C ₂₀ N ₃₃ C ₃₈	111.32834	C ₄ -0.135495
	C ₂₀ N ₃₃	1.46331	C ₃₄ N ₃₃ C ₃₈	110.79615	C ₆ -0.031043
	C₂₀C₁₇	1.53630	N ₃₃ C ₂₀ C ₁₇	113.91263	O₁₂ -0.766233
	C₁₄C₁₇	1.53253	C ₂₀ C ₁₇ C ₁₄	112.27957	C ₁₄ -0.005782
	C₁₄C₁₃	1.54909	C₁₇C₁₄C₁₃	115.82259	C ₁₇ -0.005734
	C₂₃C₁₃	1.53119	C ₁₄ C ₁₃ C ₂₃	112.91547	C ₂₃ -0.100330
	C ₃₀ F ₄₂	1.34847			C ₂₆ -0.066436
	C₄₃N₄₄	1.16331			C ₂₈ -0.061176
					N₃₃ -0.642997
					F₄₂ -0.593329
					N₄₄ -0.379025

Figure 1 shows the optimized version of the ES molecule using the DFT method. First, we must examine the Mulliken charges of the atoms in this molecule, as shown in Table 3. In this table, O₁₂, N₃₃, F₄₂, and N₄₄ are the most electronegative atoms with values of -0.766233, -0.642997, -0.593329, and -0.379025, respectively.

For all atoms around these atoms, the bond lengths and bond angles between the atoms attached to them, which are visually shown in Figure 4, ES (a and b) and given in Table 3, respectively, should be examined. Under normal conditions, a compound would be expected to begin to decompose at the point with the longest bond length or the largest bond angle, but this is not sufficient to decide where the decomposition pathway will begin.

The energy values of the compound and its fragments for fragmentation pathway determination are also a feature that contributes to deliberate fragmentation.

Table 3 According to the data presented in Figure 4, if only bond length is considered, the longest bond, C₁₄C₁₃, with a bond length of 1.54909 Å, is expected to break first. If only bond angle is considered, the bond with the longest bond angle, C₁₇C₁₄C₁₃, with a bond angle of 115.82259°, is expected to break first.

Table 4: ΔE (energy), ΔH (enthalpy) and ΔG (Gipps free energy) values of molecule ES and its fragments in the gas and water phase

(Au)	ES	E ₁	E ₂	E ₃
ΔE	-1058.287432	-1019.006223	-979.727904	-924.407026
Gas phase ΔH	-1058.286488	-1019.005279	-979.726960	-924.406082
ΔG	-1058.363136	-1019.079871	-979.797351	-924.473031
Water phase	-1058.299230	-1019.018867	-979.740594	-924.417502
	-1058.298285	-1019.017923	-979.739650	-924.416557
	-1058.375430	-1019.091994	-979.809158	-924.483744
	E ₄	E ₅	E ₆	E ₇
	-885.123502	-845.841757	-845.266601	-997.753793
	-885.122557	-845.840813	-845.265657	-997.752848
	-885.186079	-845.901128	-845.326168	-997.829206
	-885.133878	-845.852315	-845.278389	-997.765597
	-885.132934	-845.851370	-845.277445	-997.764653
	-885.196659	-845.911738	-845.338059	-997.841006
	E ₈	E ₉	E ₁₀	
	-766.795395	-1004.750251	-905.509577	
	-766.794451	-1004.749307	-905.508633	
	-766.860589	-1004.823628	-905.580604	
	-766.806100	-1004.757610	-905.516797	
	-766.805156	-1004.756666	-905.515853	
	-766.871451	-1004.831338	-905.588658	

If only Mulliken charges are considered, the fracture is predicted to begin around the oxygen atom, due to the -0.766233 value of O₁₂, the most electronegative atom. Without comparing the energy values given in Table 4, the data in Table 3 alone are meaningless.

The energy values in Table 4, in air, or in other words, in the gas phase, and additionally in the water phase, are crucial data for making a robust prediction about the order in which the compound and its fragments will decompose spontaneously, in other words without requiring any energy.

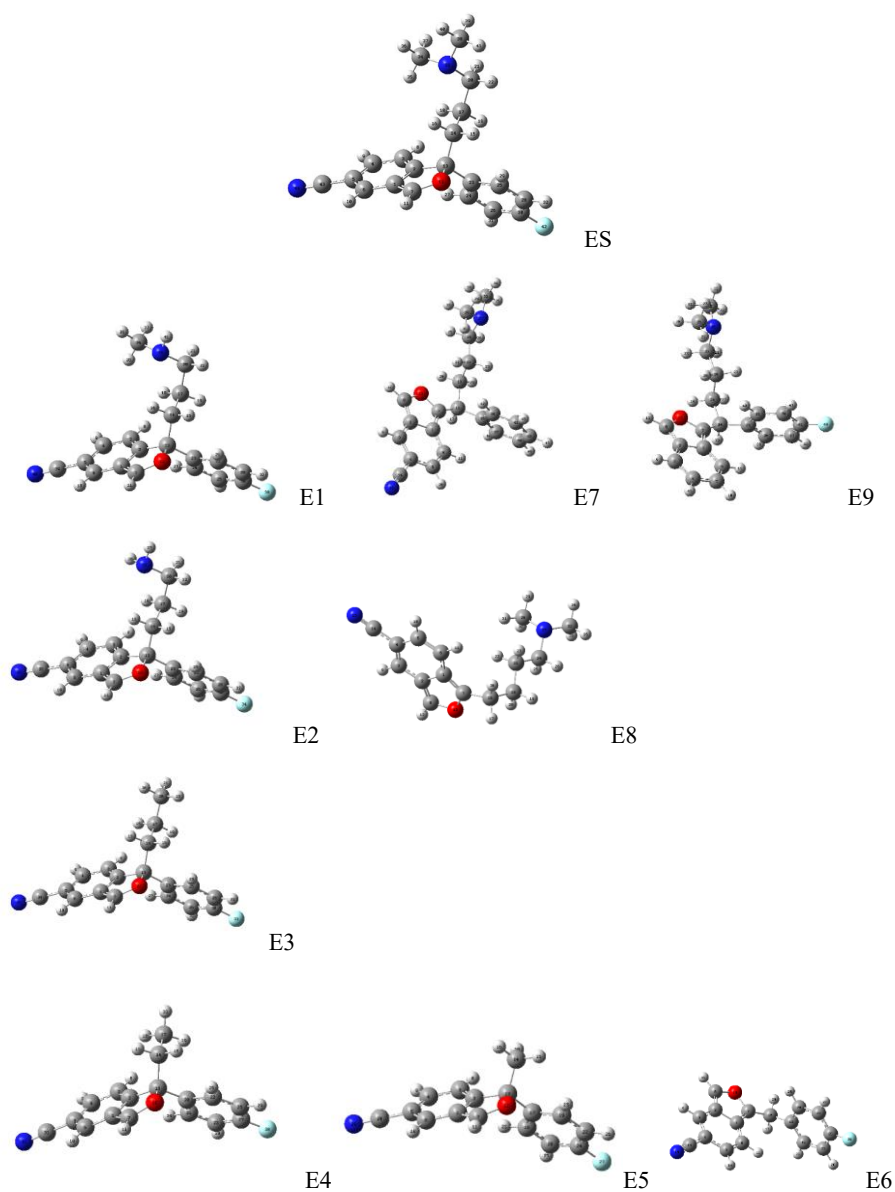


Figure 5: Fragmentation pathway (degradation mechanism) of molecule E (In the geometric structures of molecule E and all fragments optimized by the DFT method, the C atom is represented in grey, the O atom in red, the N atom in dark blue, the F atom in blue and the H atom in white)

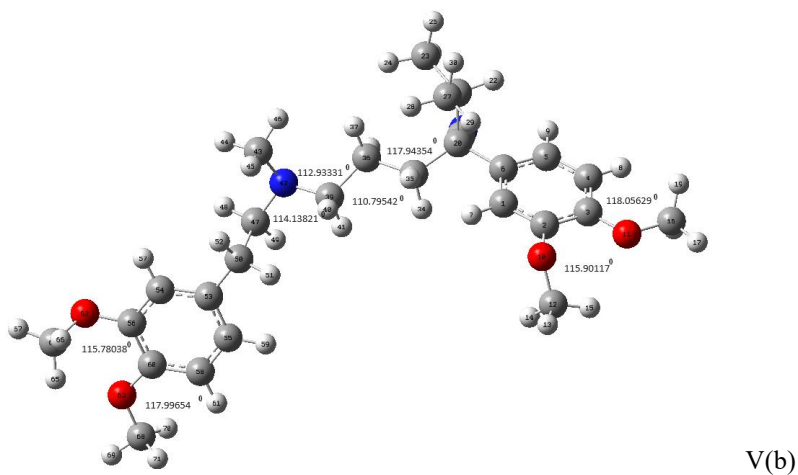
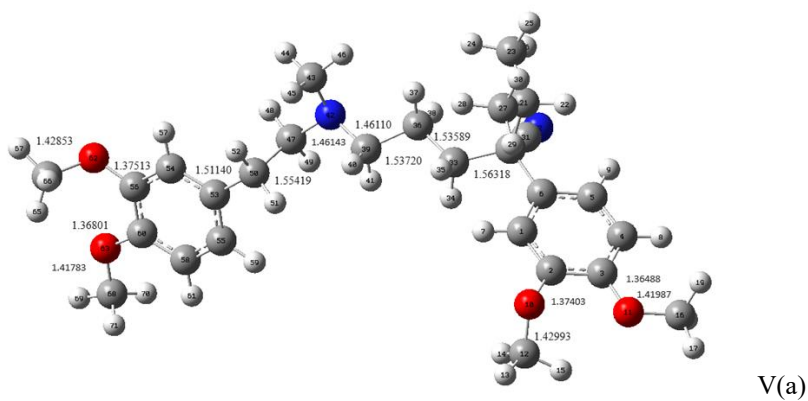
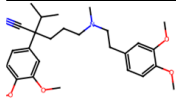


Figure 6: Bond lengths V(a) and bond angles V(b) between atoms in molecule V (C atom is represented in grey, O atom in red, N atom in dark blue and H atom in white)

Table 4: Bond lengths and bond angles between atoms in molecule V and Mulliken atom charges of molecule V



Chemical structure of molecule V is shown, featuring a central carbon atom bonded to a cyano group, a phenyl ring, and a side chain containing a nitrogen atom and another phenyl ring with methoxy groups.

	Bond lengths	(Å)	Bond angles	(°)	Mulliken atom charges
	O ₆₃ C ₆₈	1.41783	C₃O₁₁C₁₆	118.05629	C ₁ -0.233449
	O ₆₂ C ₆₄	1.42853	C₂O₁₀C₁₂	115.90117	C ₄ -0.212078
	O ₆₂ C ₅₆	1.37513	C ₅ O ₂₀ C ₃₃	110.59618	C ₅ -0.181062
	O ₆₃ C ₅₇	1.36801	C ₂₀ O ₂₁ C ₂₇	111.97656	O₁₀ -0.520530
	C₅₀C₅₃	1.51140	C ₂₃ O ₂₁ C ₂₇	110.69769	O₁₁ -0.508682
	C₄₇C₅₀	1.55419	C₂₀O₃₃C₃₆	117.94354	C ₁₂ -0.211808
	C ₄₇ N ₄₂	1.46143	C ₃₃ O ₃₆ C ₃₉	110.79542	C ₁₆ -0.217527
	C ₃₉ N ₄₂	1.46110	C ₃₆ O ₃₉ N ₄₂	112.93331	C ₂₀ -0.053821
	C₃₉C₃₆	1.53720	C ₃₉ N ₄₂ C ₄₇	114.13821	C ₂₁ -0.068388
	C₃₃C₃₆	1.53589	C ₄₃ N ₄₂ C ₄₇	113.55979	C₂₃ -0.467751
	C₃₃C₂₈	1.56318	N₄₂C₄₇C₅₀	117.05844	C₂₇ -0.462342
	O ₁₀ C ₁₂	1.42993	C ₄₇ C ₅₀ C ₅₃	111.91574	N₃₂ -0.512856
	O ₁₁ C ₁₆	1.41987	C₅₆O₆₂C₆₄	115.78038	C ₃₃ -0.294416
	C₆C₂₈	1.55091	C₆₇O₆₃C₆₈	117.99654	C ₃₆ -0.280567
	O ₁₀ C ₂	1.37403	O₆₂C₅₆C₅₇	121.50094	C ₃₉ -0.118438
	O ₁₁ C ₃	1.36488	O₆₃C₅₇C₅₈	124.88860	N₄₂ -0.368777
	C ₃₁ C ₂₈	1.47879			C ₄₃ -0.306045
	C₂₁C₂₇	1.53492			C ₄₇ -0.133744
	C₂₁C₂₃	1.53840			C ₅₀ -0.366942
	C₂₀C₂₁	1.59161			C ₅₄ -0.233387

Table 5: ΔE (energy), ΔH (enthalpy) and ΔG (Gipps free energy) values of molecule V and its fragments in the gas and water phases

(Au)	V	V1	V2	V3
ΔE	-1461.419410	-1422.151890	-1382.874885	-752.129548
Gas phase ΔH	-1461.418466	-1422.150945	-1382.873940	-752.128604
ΔG	-1461.528592	-1422.257547	-1382.976921	-752.198486
Water phase	-1461.438103		-1382.895676	-752.137508
	-1461.437159		-1382.894732	-752.136564
	-1461.547010		-1382.998122	-752.206442
	V4	V5	V6	V7
	-712.846017	-673.561744	-634.281419	-595.004130
	-712.845072	-673.560800	-634.280475	-595.003186
	-712.911090	-673.623308	-634.340093	-595.059226
	-712.853890	-673.569635	-634.290529	-595.014602
	-712.852946	-673.568691	-634.289585	-595.013658
	-712.918953	-673.631492	-634.349227	-595.069831
	V8	V9		
	-634.285567	-595.017138		
	-634.284623	-595.016194		
	-634.343917	-595.071615		
	-634.295396	-595.027040		
	-634.294452	-595.026095		
	-634.353615	-595.081480		

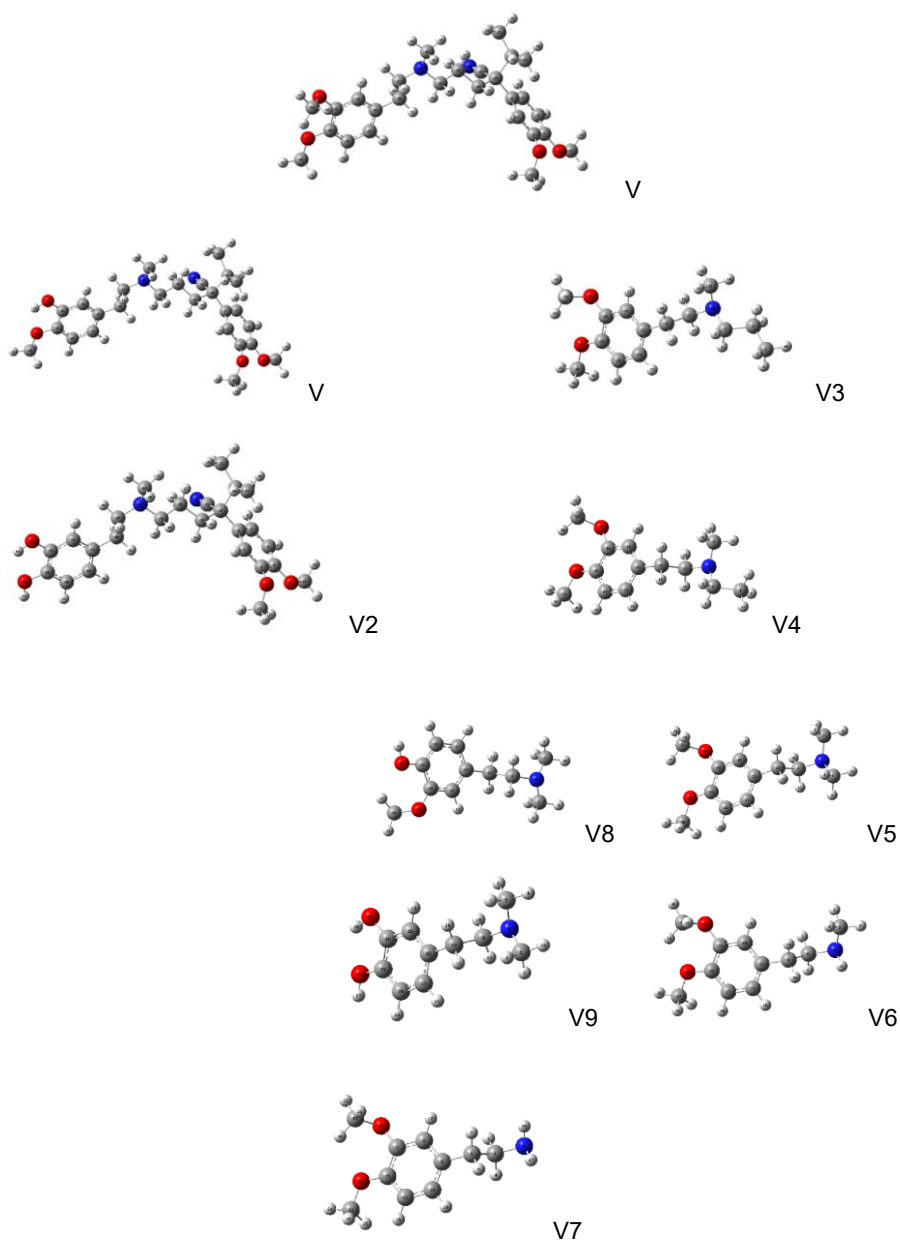


Figure 7: Fragmentation pathway (degradation mechanism) of molecule V (In the geometric structures of molecule V and all fragments optimized by the DFT method, the C atom is represented in grey, the O atom in red, the N atom in dark blue and the H atom in white)

DISCUSSION AND CONCLUSION

Selected pharmaceutical product active ingredients have a water-soluble structure due to oral administration when the product is completed and released to the market. Whether used for therapeutic purposes, unused, or discarded at the end of its shelf life, these organic compounds enter the natural cycle due to the lack of awareness in our country. Waste, whether medical or regular, is still recycled, resulting in these organic compounds entering the natural cycle. These water-soluble compounds constitute a significant group of air and water pollutants. Their degradation mechanisms must be elucidated before residues can be removed from air and water.

Experimental kinetic information on the gas-phase and water-phase reactions of active pharmaceutical ingredients with OH radicals is available in the literature. However, the reaction mechanisms of these substances have not been fully determined. In this study, we examined the reactions of selected molecules with OH radicals and calculated their degradation mechanisms using the DFT method. First, the gas-phase reactions were concluded, and due to their potential to cause pollution in wastewater, their mechanisms in aqueous environments were also investigated under the influence of solvents. The mechanism of the reactions of compounds with OH radicals in the atmosphere and in water was fully elucidated, and the reaction products were also fully identified. By examining the Mulliken Charges of the atoms in the molecule, the arrangement of electronegative atoms and surrounding atoms, stable double bonds, weak bonds at the ends of the molecule, calculated energies, bond lengths, and bond angles between atoms helped us select all the components that would determine the degradation mechanism. Figures 3, 5, and 7 show the degradation reaction pathways of all selected pharmaceutical molecules, respectively.

Before pharmaceutical products are released to the market, all necessary research experiments are conducted, all potential side effects are identified, and these studies are ultimately used for human treatment. An overlooked or underestimated issue is the fate of many pharmaceutical products used for therapeutic purposes if they enter the environment. This research, conducted solely on a theoretical basis without using any chemical products, illuminated the pathways of the active ingredients in the product, just as they would in nature, in water, or in the atmosphere, namely, the theoretical degradation reactions involving OH radicals. In addition to the three molecules examined in this study, research on the molecule Apranax (AP), marketed as the active ingredient of naproxen or naproxen sodium (NS), from our study within the same project, has been published, and degradation mechanism has been identified for this molecule (Eren and Yalcin Gürkan, 2024). The study on the molecule Paxil, marketed as the active ingredient of paroxetine HCl (PA), also included in the same study, has been

completed and is currently in the process of being published in the same journal.

The results obtained can be compared with the fragments we obtained in our degradation reactions, if desired, by collecting the necessary wastewater samples and analysing them with HPLC. We previously completed a scientific research project on the removal of carbamate and organophosphate pesticides from nature using advanced oxidation techniques (Eren and Yalcin Gürkan, 2021, 2022, 2023a). The same method can be used at the end of this study and form the basis for further research.

ACKNOWLEDGEMENTS

Produced from the TNKU BAP project titled “Theoretical investigation of degradation mechanisms of selected pharmaceutical product active ingredients” numbered NKUBAP.00.GA.23.506.

REFERENCE

- Alenghat, F.J., Golan D.E. (2017). Drug-receptor interactions. In *Fundamental Principles of Pharmacology: The Pathophysiological Basis of Drug Therapy*, 4th ed.
- Anbar, M., Neta, P. (1967). *Int J Appl Radiat Isot*, 18: 493.
- Aschmann, S.M., Tuazon, E.C. and Atkinson, R. (2005). *J. Phys. Chem. A*, 109, 2282.
- Aschmann S M, Atkinson R (2006). *J. Phys. Chem. A*, 110, 13029.
- Aschmann, S.M., Tuazon, E.C., Long, W.D., and Atkinson, R. (2010). *J. Phys. Chem. A*, 114, 3523.
- Atkinson, R., Aschmann, S.M., Goodman, M.A., and Winer, A.M. (1988). *Int. J. Chem. Kinet.*, 20, 273.
- Atkinson, R., Arey, J. (2003). *Chem. Rev.*, 103, 4605.
- Bade, R., Chan, H., and Reynisson, J. (2010). Characteristics of known drug space. Natural products, their derivatives, and synthetic drugs. *European Journal of Medicinal Chemistry*, 45(12), 5646–52.
- Baron, S., Linton, S., and O'Malley M.A. (2023). *The Journal of Medicine and Philosophy: A Forum for Bioethics and Philosophy of Medicine*, 48, 551–564.
- Bhatia, N.M., Pathade, P.A., More, H.N., Choudhar P.B., Jadhav, S.D., and Bhatia M.S. (2013). *Journal of Analytical Chemistry* 68 (10), 924-930.
- Buxton, V.G., Greenstock, L.C., and Helman, P.W. (1988). *Journal of Physical and Chemical Reference Data*, 17, 513.
- Camlibel, M., Erdur, B., Yilmaz, A., Ozen, M., and Uyanik, A. (2019). Comparison of the effects of piroxicam and diclofenac sodium as treatments for primary

- dysmenorrhea, *Medical science monitor: international medical journal*, 25,157.
- Clayton, A., Kelle, A., McGarvey, A., and Elizabeth, L (2006). *Journal of Affective Disorders*, 91(1), 27-32.
- Eren, B., Yalcin Gurkan, Y. (2017). Possible reaction pathways of the lincomycin molecule according to the DFT calculation method, *J. Serb. Chem. Soc.*, 82(3), 277–287.
- Eren, B., Yalcin Gurkan, Y. (2021). Theoretical and experimental photodegradation of Phosmet via oxidation techniques in the presence of aqueous TiO₂ suspension, *Bulgarian Chemical Communications*, 53, 456-463.
- Eren, B., Yalcin Gurkan, Y. (2022). Possible reaction pathways of selected organophosphorus and carbamate pesticides according to the DFT calculation method, *Bulgarian Chemical Communications*, 54, 224-234.
- Eren, B., Yalcin Gurkan, Y. (2023a), Theoretical study of the Azinphos-methyl, Monocrotophos and Omethoate compounds in two phases: Mechanism and DFT study. *Innovative Research in Engineering*, Duvar Publishing, İzmir Turkey, 4,49-71.
- Eren, B., Yalcin Gurkan, Y. (2023b). Experimental Photodegradation of OPsand CBs by Advanced Oxidation Techniques in the Aqueous TiO₂ Suspensions, (IJANSER) *International Journal of Advanced Natural Sciences and Engineering Research*, 7, 31-38.
- Eren, B., Yalcin Gurkan, Y. (2024). Theoretical study of possible reaction pathways with the OH radical of the Apranax (AP) molecule with naproxen sodium (NS) as an active ingredient, *Bulgarian Chemical Communications*, vol. 56, 242-246.
- Gaussian 09, Revision B.04 (2009). Gaussian, Inc., Pittsburgh: PA.
- Halliwell, B., Grootveld, M., Gutteridge, J.M.C. (1998). *Methods Biochem. Anal.*, 33, 59.
- Haynes WM (ed.) (2014-2015) *CRC Handbook of Chemistry and Physics*, 95th Edition: CRC Press LLC, Boca Raton: FL, 3-546.
- Matthews, R.W., Ollis, D., Al Ekabi, H. (1993). Elsevier 121, New York.
- Ommaty, R. (2006). *Vademecum Modern Drug Guide*: Pelikan Medical and Technical Bookselling Co. Ltd.
- O'Neil M.J (ed.) (2013). *The Merck Index - An Encyclopaedia of Chemicals, Drugs, and Biologicals*. Cambridge, UK: Royal Society of Chemistry.
- Verschuere, K. (1996). *Handbook of Environmental Data on Organic Chemicals*. Wiley 2nd ed., New York.

Synthesis And Characterization Of Nickel Orthoborate Nanopowders

Eray SÖNMEZER ^{*1}

Ayşe MORKAN ¹

¹Department of Chemistry, Bolu Abant İzzet Baysal University, Türkiye

^{*}(eraysonmezer@gmail.com) Email of the corresponding author

ABSTRACT

In this study, nickel orthoborate ($\text{Ni}_3(\text{BO}_3)_2$) nanopowder materials were synthesized using the solution combustion synthesis (SCS) method with two different organic fuels (tartaric acid and HMTA). Nickel nitrate and boric acid were used as starting materials, and reaction conditions were optimized through stoichiometric calculations. The obtained products were calcined at 400°C and 900°C and subsequently characterized. XRD analyses confirmed the successful production of the $\text{Ni}_3(\text{BO}_3)_2$ phase for both fuel types. Characteristic vibrational bands of BO_3 units were identified in the FTIR spectra. The results demonstrated that both fuel type and calcination temperature significantly influence the crystalline structure and thermal stability of the products. Samples synthesized with tartaric acid exhibited more stable structures at higher temperatures, while HMTA-derived samples showed better efficiency at lower temperatures. These findings provide valuable data for optimizing nickel orthoborate materials for industrial applications.

Keywords – Nanosized, Nickel Orthoborate, Solution Combustion Synthesis Method (SCS), XRD, FTIR Spectroscopy.

INTRODUCTION

Transition metal borates have garnered increasing attention in recent years due to their versatile structural, electronic, and catalytic properties, which make them promising candidates for applications such as batteries, supercapacitors, electrocatalysis, and electrochemical sensors [1–3]. Although borates exhibit desirable physicochemical characteristics, their utilization in energy-related fields remains limited compared to other transition metal compounds. Theoretically, transition metals readily form various borates and borides by combining with boron, enabling the design of materials with tunable properties [4,5].

Multiple synthesis methods have been employed to fabricate transition metal borates, including electrodeposition, solvothermal synthesis, solid-state reactions, in situ co-reduction, microwave irradiation, direct precipitation, liquid-phase reactions, and hydrothermal techniques. Each approach offers distinct advantages in controlling particle size, morphology, and phase purity [6–19].

Among nickel-containing borates, nickel orthoborate ($\text{Ni}_3(\text{BO}_3)_2$), a member of the kotoite family $\text{M}_3(\text{BO}_3)_2$ (where $\text{M} = \text{Mg}, \text{Ni}, \text{Co}, \text{Zn}, \text{Cu}$, etc.), exhibits unique magnetic, catalytic, and photoluminescence properties [14,15]. The chemical stability and multiple oxidation states of nickel in $\text{Ni}_3(\text{BO}_3)_2$ enable

efficient charge storage and redox activity, as demonstrated by changes in nickel valence states from +2 to +3.6 under applied potentials, making it a promising electrode material for energy storage devices [10,11,16].

Despite these advantages, nickel borates have been less explored than other nickel compounds, and reports on their synthesis and electrochemical applications are limited. Various synthesis techniques such as thermal decomposition, hydrothermal treatment, surfactant-assisted thermal conversion, self-assembly strategies, electrodeposition, coprecipitation, and solid-state reactions have been employed to prepare $\text{Ni}_3(\text{BO}_3)_2$ [10,13–20]. Among these, solution combustion synthesis (SCS) is a rapid, cost-effective, and energy-efficient method capable of producing nanostructured materials with controlled morphology.

In this study, $\text{Ni}_3(\text{BO}_3)_2$ nanopowders was synthesized via the SCS method using two different fuels. The effects of fuel type on the structural properties of the resulting materials were systematically investigated through X-ray diffraction (XRD) and Fourier-transform infrared spectroscopy (FTIR). This work aims to elucidate the relationship between synthesis parameters and material properties to optimize $\text{Ni}_3(\text{BO}_3)_2$ for potential applications in optoelectronics and sensing.

MATERIALS AND METHOD

Nickel orthoborate ceramic nanopowders were prepared using the solution combustion synthesis (SCS) method [20]. The starting materials, $\text{Ni}(\text{NO}_3)_2$, H_3BO_3 (boric acid), and the fuels were mixed in stoichiometric amounts and dissolved in a minimum amount of distilled water. The resulting mixture was continuously stirred on a magnetic stirrer at 370°C until a gel-like consistency formed, allowing the water to evaporate. The resulting gel-like structure was then held in a preheated furnace at 400°C for 5 minutes. It was observed that the as-prepared product displayed different colors depending on the fuel types used. The annealing process was performed at two distinct temperatures: 400°C for 1 hour and 900°C for 1 hour.

Finally, the obtained products were characterized by XRD and FTIR techniques. To examine the structural properties of the obtained compounds, the Rigaku miniflex and multiflex X-ray powder diffractometer with $\text{CuK}\alpha$ (30-40kV, 1020mA, $\lambda=1.54056 \text{ \AA}$) radiation was used and the obtained data were compared with the JCPDS data cards. The infrared spectra and corresponding bond vibrations of the obtained products were analyzed using a PerkinElmer Fourier Transform Infrared (FT-IR) spectrophotometer,

operating in the spectral range of 4000–400 cm^{-1} . For the measurements, the samples were prepared in pellet form by thoroughly mixing the product with potassium bromide (KBr) at a weight ratio of 0.1500:0.0010 (KBr: product, wt/wt), ensuring optimal transparency and uniform distribution for accurate spectral analysis.

RESULTS AND DISCUSSION

In this study, the Solution Combustion Synthesis (SCS) technique was employed for the synthesis of nickel orthoborate compound. In the experimental studies, different organic fuels (hexamethylenetetramine and tartaric acid) were selected as one of the reaction parameters, and the process temperature was set within the range of 400-900°C. The reaction duration was determined to be one hour.

During the synthesis process, various physicochemical changes were observed in the system depending on the type of fuel used. Particularly notable were the observed gas emissions during combustion reactions and the resulting distinct differences in the color and morphological properties of the products. This demonstrates that the type of fuel used plays a determining role in the final product characteristics.

Tartaric Acid:

The homogeneous solution exhibited a turbid appearance and transformed into a green-colored gel at 370°C. A normal amount of gas was released during the process. After 5 minutes of preheating at 400°C, a rigid brown form was obtained.



Photo.1 The images of $\text{Ni}_3\text{B}_2\text{O}_6$ samples prepared with tartaric acid fuel a) gel form
b) synthesis

HMTA:

When the starting materials were dissolved in a small amount of distilled water, the resulting homogeneous solution was initially light green. However, as the temperature reached 370°C, a dark green, gel-like structure formed in the solution. The gas evolution observed during this process was at expected levels. Subsequently, after a 5-minute preheating stage at 400°C, the product turned a dark brownish-black color. Some difficulties were encountered when trying to remove this solidified product from the evaporating dish.

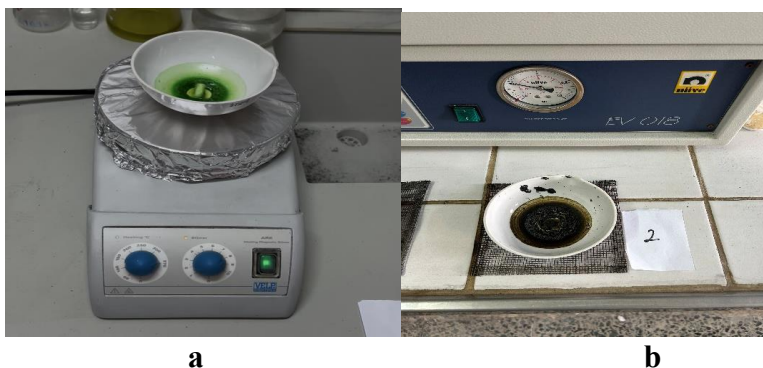


Photo.2 The images of $\text{Ni}_3\text{B}_2\text{O}_6$ samples for HMTA fuel a) gel form b) synthesis

Structural Characterization Studies of Nickel Orthoborate

The structural properties of nickel orthoborate were determined using products synthesized at 400°C for 10 minutes and subsequently heated at both 400°C and 900°C. Characterization was performed using X-Ray Diffraction (XRD) to examine the crystallite size and crystal structures, and FT-IR to identify the vibrational modes.

FT-IR Spectroscopy Studies

The FT-IR spectra of the synthesized by SCS technique, pure $\text{Ni}_3\text{B}_2\text{O}_6$ compound, as illustrated in Figures 1 to 6, reveal a series of distinct absorption bands corresponding to specific vibrational modes within the structure. These bands have been carefully analyzed and their assignments were made by comparing them with well-established vibrational data previously reported in the scientific literature [21], providing insights into the molecular structure and bonding environment of the borate compound.

The weak absorption bands assigned at 3431 cm^{-1} and 1635 cm^{-1} are most likely due to a small amount of physically adsorbed water on the surface of

the sample, which is a common occurrence in metal borate materials exposed to ambient conditions.

A prominent and sharp band at 1303 cm^{-1} is attributed to the asymmetric stretching vibrations of the B–O bonds, indicating the presence of BO_3 units in the crystal structure. Another strong absorption band appearing at 1186 cm^{-1} is tentatively assigned to the stretching vibrations of Ni–O bonds, suggesting strong metal–oxygen coordination within the lattice. Additionally, the absorption bands observed at 723 cm^{-1} and 633 cm^{-1} correspond to the out-of-plane bending modes of the B–O groups, further confirming the exclusive presence of trigonal planar BO_3 units in the compound.

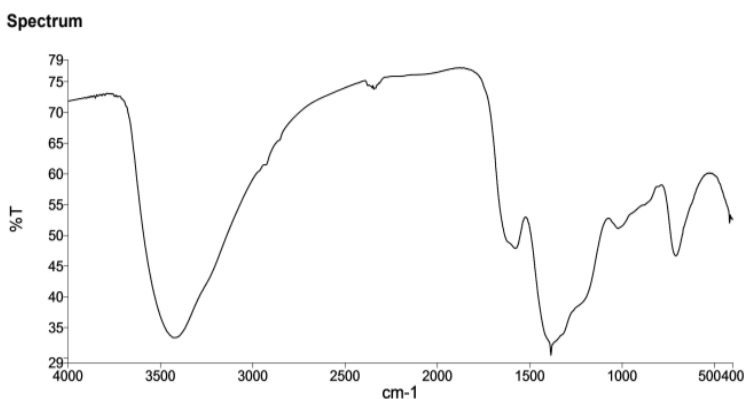


Fig.1 FT-IR Spectrum of as-prepared $\text{Ni}_3\text{B}_2\text{O}_6$, Using TA Fuel

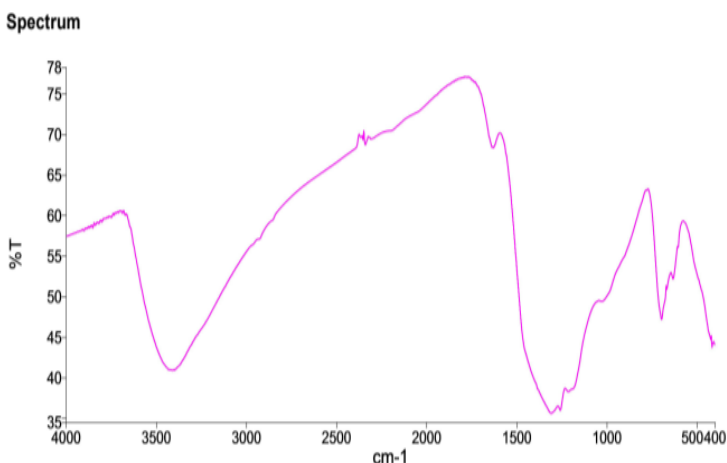


Fig.2 FT-IR Spectrum of as-prepared $\text{Ni}_3\text{B}_2\text{O}_6$, Using HMTA Fuel

These vibrational band assignments are in excellent agreement with the expected structural features of nickel orthoborate, $\text{Ni}_3\text{B}_2\text{O}_6$, which is

known to contain only BO_3 groups rather than tetrahedral BO_4 units, supporting the integrity and phase purity of the synthesized material.

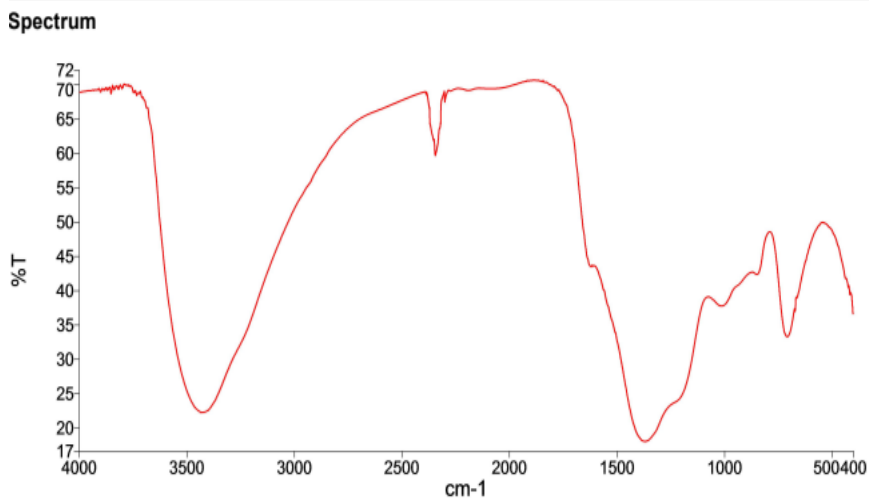


Fig. 3 FT-IR Spectrum of $\text{Ni}_3\text{B}_2\text{O}_6$ heated at 400°C using TAFuel

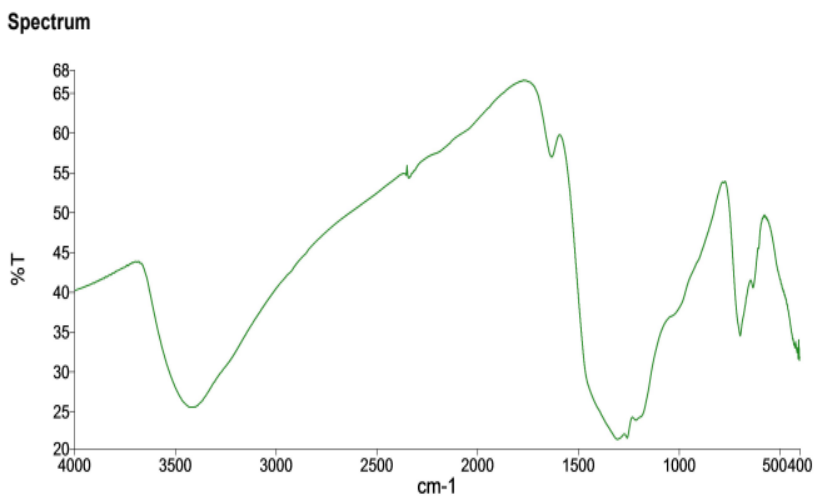


Fig.4 FT-IR Spectrum of $\text{Ni}_3\text{B}_2\text{O}_6$ heated at 400°C using HMTA Fuel

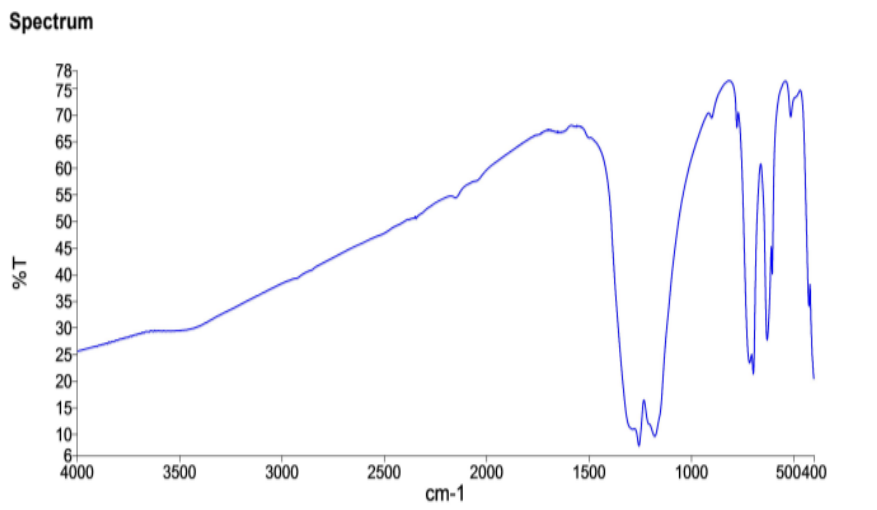


Fig.5 FT-IR Spectrum of $\text{Ni}_3\text{B}_2\text{O}_6$ heated at 900°C Using TA Fuel

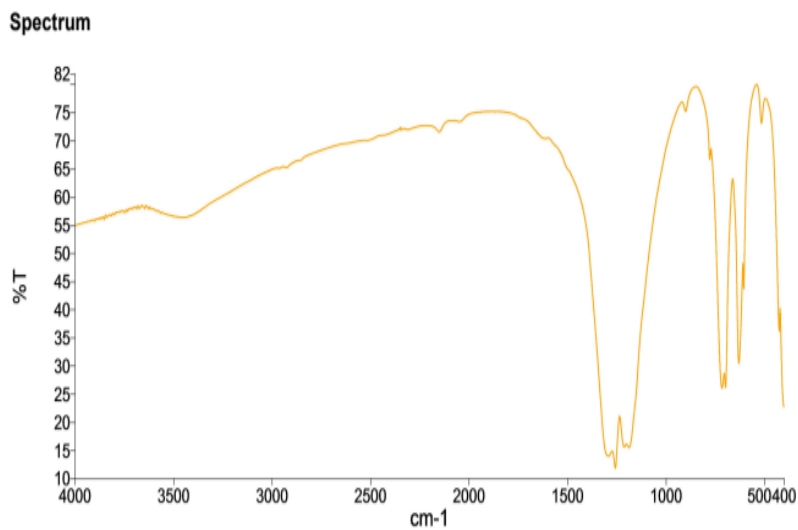


Fig.6 FT-IR Spectrum of $\text{Ni}_3\text{B}_2\text{O}_6$ heated at 900°C Using HMTA Fuel

X-Ray Diffraction (XRD) Studies

The crystallinity and phase composition of the synthesized $\text{Ni}_3\text{B}_2\text{O}_6$ material were thoroughly investigated using powder X-ray diffraction (XRD) analysis.

This technique was employed to examine the structural evolution of the as-prepared nickel orthoborate samples subjected to calcination at different temperatures.

The XRD patterns corresponding to the samples sintered at 400 °C and 900 °C, utilizing TA and HMTA as fuels, are presented in Figures 7 and 8, respectively. At the relatively low calcination temperature of 400 °C, the recorded diffraction pattern revealed a broad and diffuse background without any distinct peaks, indicating the presence of an amorphous phase and suggesting that the crystallization process had not yet commenced at this stage. However, upon increasing the calcination temperature to 900 °C, a significant transformation in the phase structure was observed. Well-defined and sharp diffraction peaks emerged, signifying the formation of a highly crystalline material.

The peak positions and intensities clearly indicated the successful synthesis of phase-pure $\text{Ni}_3\text{B}_2\text{O}_6$ with no detectable secondary phases. This observation confirms that 900 °C is a sufficient temperature for complete crystallization and phase stabilization of $\text{Ni}_3\text{B}_2\text{O}_6$.

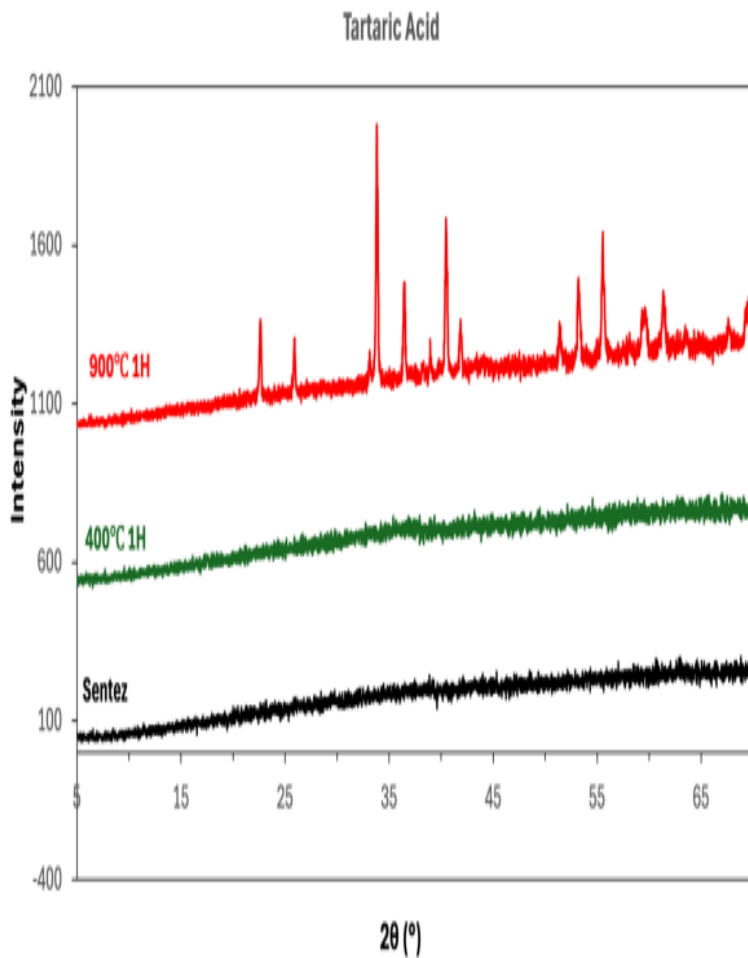


Fig.7 XRD Patterns of $\text{Ni}_3\text{B}_2\text{O}_6$ produced by SCS method Using TA Fuel

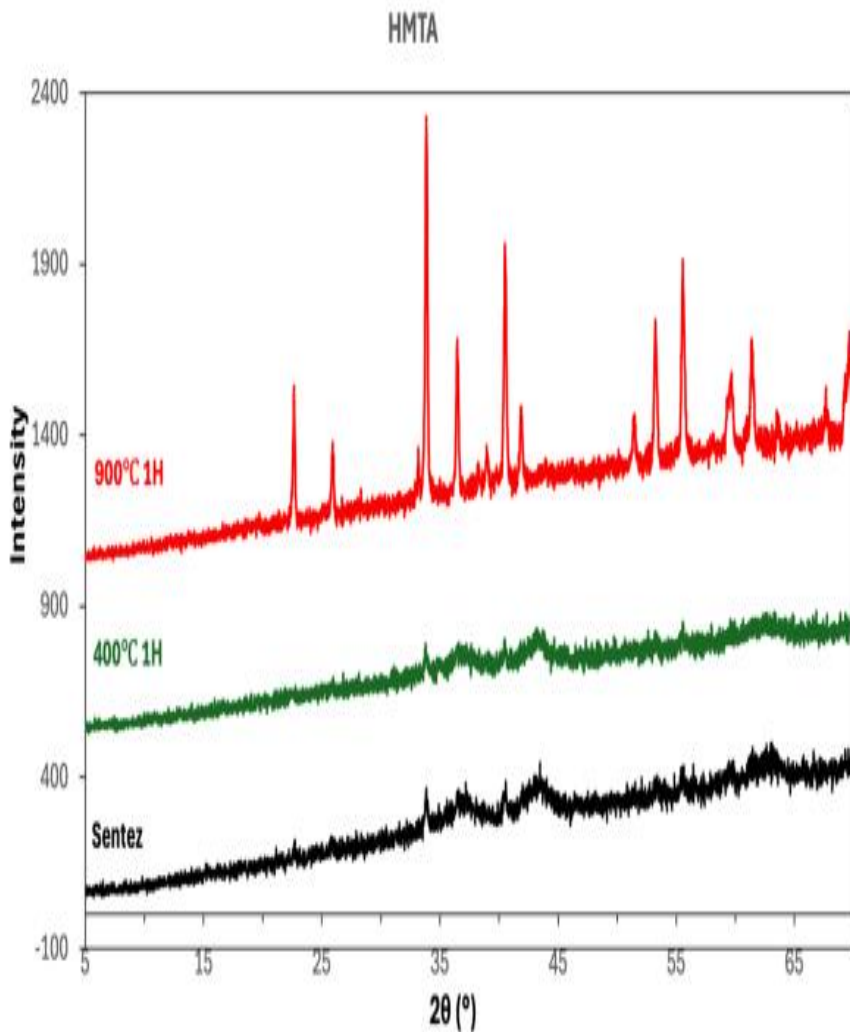


Fig.8 XRD Patterns of $\text{Ni}_3\text{B}_2\text{O}_6$ produced by SCS method Using HMTA Fuel

The XRD powder diffraction patterns obtained at 900°C exhibited characteristic reflections at 2θ values of 22.6° , 25.8° , 33.8° , 36.7° , 40.5° , 43.3° , 53.2° , 55.5° , 59.5° , 62.2° , and 69.5° , which correspond to the (011), (101), (121), (211), (131), (040), (202), (132), (321), (330), and (251) crystallographic planes, respectively. These diffraction peaks are in excellent agreement with those of orthorhombic $\text{Ni}_3\text{B}_2\text{O}_6$ [20] and all observed reflections can be successfully indexed to this structure based on the Joint Committee on Powder Diffraction Standards (JCPDS) card No. 22-0745. The data conclusively confirm that the product obtained at 900°C exhibits a single-phase orthorhombic crystal structure with high crystallinity,

demonstrating the efficiency of the calcination process in promoting phase formation and structural ordering.

In addition to confirming the formation of orthorhombic $\text{Ni}_3\text{B}_2\text{O}_6$ at elevated temperatures, further analysis of the XRD data provides valuable insight into the material's structural characteristics. The sharpness and intensity of the diffraction peaks obtained at 900 °C indicate a high degree of crystallinity, which reflects the enhanced atomic ordering within the lattice as a result of sufficient thermal energy during the calcination process. The absence of any secondary phases or impurity peaks across the entire diffraction pattern further confirms the high phase purity of the synthesized product.

To estimate the average crystallite size of the $\text{Ni}_3\text{B}_2\text{O}_6$ particles, the Scherrer equation was applied to the most intense diffraction peak, typically located around $2\theta \approx 33.8^\circ$, corresponding to the (121) plane. The calculated crystallite size was found to be in the nanometer range, suggesting that while the material exhibits high crystallinity, it still retains a fine microstructure, which may be advantageous for various applications, such as catalysis or electrochemical energy storage, due to the increased surface area.

Moreover, a comparative assessment of the XRD patterns obtained using different fuels—Tartaric Acid (TA) and Hexamethylenetetramine (HMTA)—reveals subtle differences in peak broadening and relative intensities. Samples synthesized using HMTA as fuel tend to exhibit slightly narrower and more intense peaks compared to those prepared with TA, implying a marginally higher crystallinity and possibly larger crystallite domains. This observation can be attributed to differences in combustion behavior: HMTA, being a nitrogen-rich compound, generally promotes a more uniform and energetic combustion process, thereby enhancing thermal decomposition and crystal growth during synthesis.

In summary, XRD analysis confirms that calcination at 900 °C results in the successful formation of phase-pure, orthorhombic $\text{Ni}_3\text{B}_2\text{O}_6$ with well-developed crystallinity. The choice of fuel plays a secondary but noticeable role in crystallite growth and structural uniformity. These findings highlight the importance of thermal treatment parameters and fuel chemistry in directing the structural evolution and phase purity of metal borate materials.

CONCLUSION

Nickel orthoborate ($\text{Ni}_3(\text{BO}_3)_2$) was successfully synthesized using both tartaric acid (TA) and hexamethylenetetramine (HMTA) as fuels via the solution combustion synthesis (SCS) method. The reactions were efficiently carried out with short processing times and at moderate temperature ranges (400-900°C). Stoichiometric calculations and experimental masses (0.9631 g for TA and 0.7988 g for HMTA) confirmed the expected yields, with a 4% excess of H_3BO_3 ensuring complete reaction.

XRD analyses revealed distinct phase formations at different temperatures. At 400°C, amorphous or low-crystallinity phases were dominant, while at 900°C, well-crystallized $\text{Ni}_3(\text{BO}_3)_2$ phases characterized by sharp diffraction peaks were observed.

FT-IR spectra confirmed the presence of BO_3 groups through bands at 695-720 cm^{-1} (bending), 1010-1065 cm^{-1} (symmetric stretching), and 1220-1245 cm^{-1} (asymmetric stretching). HMTA-derived samples exhibited sharper peaks at 900°C, indicating better structural ordering compared to TA.

This study demonstrates that HMTA is more suitable for producing high-crystallinity products, highlighting the versatility of the SCS method for $\text{Ni}_3(\text{BO}_3)_2$ synthesis.

REFERENCES

1. Yamada, A.; Lwane, N.; Harada, Y.; Nishimura, S. I.; Koyama, Y.; Tanaka, L. Lithium Iron Borates as High-Capacity Battery Electrodes. *Adv. Mater.* **2010**, *22*, 3583–3587
2. Zhou, K.; Xu, G.; Chen, Y.; Chen, Z.; Huang, J.; Zhen, Y.; Huang, Z.; Hong, Z. Carbon Coated Transition Metal Borates as Anode Materials for Na-Ion Batteries. *Chem. Eng. J.* **2019**, 375
3. Tao, L.; Neilson, J. R.; Melot, B. C.; McQueen, T. M.; Masquelier, C.; Rousse, G. Magnetic Structures of LiMBO_3 (M = Mn, Fe, Co) Lithiated Transition Metal Borates. *Inorg. Chem.* **2013**, *52*, 11966–11974
4. Beckett, M. A. Recent Advances in Crystalline Hydrated Borates with Non-Metal or Transition-Metal Complex Cations. *Coord. Chem. Rev.* **2016**, *323*, 2–14
5. Sun, Y.; Liu, Z.; Zheng, X.; Wang, C.; Wang, J.; Jiang, M.; Jiang, D.; Liu, J. Construction of $\text{KCu}_7\text{S}_4@ \text{NiMoO}_4$ Three-Dimensional Core-Shell Hollow Structure with High Hole Mobility and Fast Ion Transport for High-Performance Hybrid Supercapacitors. *Composites, Part B* **2023**, *249*, 110409
6. Yan, J.; Fan, Z.; Sun, W.; Ning, G.; Wei, T.; Zhang, Q.; Zhang, R.; Zhi, L.; Wei, F. Advanced Asymmetric Supercapacitors Based on $\text{Ni}(\text{OH})_2/\text{Graphene}$ and Porous Graphene Electrodes with High Energy Density. *Adv. Funct. Mater.* **2012**, *22*, 2632–2641

7. Ma, X.; Zhang, L.; Xu, G.; Zhang, C.; Song, H.; He, Y.; Zhang, C.; Jia, D. Facile Synthesis of NiS Hierarchical Hollow Cubes via Ni Formate Frameworks for High Performance Supercapacitors. *Chem. Eng. J.* **2017**, *320*, 22– 28,
8. Hou, S.; Xu, X.; Wang, M.; Xu, Y.; Lu, T.; Yao, Y.; Pan, L. Carbon-Incorporated Janus-Type Ni 2P/Ni Hollow Spheres for High Performance Hybrid Supercapacitors. *J. Mater. Chem. A* **2017**, *5*, 19054– 19061
9. Shwetha, K. P.; Manjunatha, C.; Sudha Kamath, M. K.; Rastogi, C. K.; Chaudhary, V.; Maurya, G.; Athreya, Y.; Shivaraj, B. W.; Khosla, A. Fabrication of super-high energy density asymmetric supercapacitor prototype device employing NiCo_2S_4 @f-MWCNT nanocomposite. *J. Energy Storage* **2023**, *72* (D), 108657
10. Qin, W.; Liu, Y.; Liu, X.; Yang, G. Facile and Scalable Production of Amorphous Nickel Borate for High Performance Hybrid Supercapacitors. *J. Mater. Chem. A* **2018**, *6*, 19689– 19695
11. Sun, X.; Zhao, K.; Liu, Z.; Feng, Z.; Wang, Z.; Cui, L.; Liu, J. Facile Electrodeposition of $\text{Ni}_3(\text{BO}_3)_2$ Nanospheres on Ti Mesh for High-Performance Asymmetric Supercapacitors. *J. Energy Storage* **2022**, *55*, 105763
12. Becker, P. Borate Materials in Nonlinear Optics. *Adv. Mater.* **1998**, *10*, 979– 992
13. Liang, P.; Du, L.; Wang, X.; Liu, Z. H. Preparation of $\text{Ni}_3\text{B}_2\text{O}_6$ Nanosheet-Based Flowerlike Architecture by a Precursor Method and Its Electrochemical Properties in Lithium-Ion Battery. *Solid State Sci.* **2014**, *37*, 131– 135
14. Lofland, S. E.; Ramanujachary, K. V.; Ganguli, A. K. A New Low Temperature Methodology to Obtain Pure Nanocrystalline Nickel Borate. *J. Organomet. Chem.* **2010**, *695*, 1002– 1005
15. Sivakumar, G.; Natarajan, S. Structural Evolution of Transition Metal Orthoborates ($\text{Zn}_3\text{B}_2\text{O}_6$ – $\text{Co}_3\text{B}_2\text{O}_6$) with the Kotoite Mineral Structure: Synthesis, Structure and Properties. *Z. Anorg. Allg. Chem.* **2022**, *648*, e202200017
16. Bediako, D. K.; Lassalle-Kaiser, B.; Surendranath, Y.; Yano, J.; Yachandra, V. K.; Nocera, D. G. Structure-Activity Correlations in a Nickel-Borate Oxygen Evolution Catalyst. *J. Am. Chem. Soc.* **2012**, *134*, 6801– 6809
17. Liu, X.; Zhu, W.; Cui, X.; Liu, T.; Zhang, Q. Facile Thermal Conversion Route Synthesis, Characterization, and Optical Properties of Rod-like Micron Nickel Borate. *Powder Technol.* **2012**, *222*, 160– 166
18. Ge, J.; Han, B.; Liang, S.; Liu, Z.; Xiao, Y.; Kuang, J.; Guan, M.; Liu, X. Rational Design of Three-Dimensional Nickel Borate/Graphene Nanoarrays for Boosted Photoconversion of Anthropogenic CO_2 . *Surf. Interfaces* **2021**, *27*, 101497
19. Pang, H.; Lu, Q.; Chen, C.; Liu, X.; Gao, F. Facile Synthesis of $\text{Ni}_3(\text{BO}_3)_2$ Nanoribbons and Their Antimicrobial, Electrochemical and Electrical Properties. *J. Mater. Chem.* **2011**, *21*, 13889– 13894
20. Beena Somanath, Manjunatha C, Yash Athreya, Shwetha KP, Nelsa Abraham, Suresh Babu Viswanathan, Sudha Kamath MK, S. Girish Kumar, and Ajit Khosla . Scalable Synthesis of $\text{Ni}_3\text{B}_2\text{O}_6$ Nanograins and Fabrication of a Coin Cell Supercapacitor for Powering Temperature Sensor Devices. *ACS Applied Electronic Materials* **2023**, *5*, 9, 5005-5016
21. Morkan, A.; Gul, E.; Morkan, I.; Kahveci, G. Effect of magnesium source on the fabrication of kotoite $\text{Mg}_3\text{B}_2\text{O}_6$ ceramic. *International Journal of Applied Ceramic Technology*, **2018**, *15*(6), 1584–1593.

Investigation of Sterilization Technology- A Brief Overview

Neşe KEKLİKÇİOĞLU ÇAKMAK^{1*}

Department of Chemical Engineering, Faculty of Engineering, Sivas Cumhuriyet University,
58140 Sivas, Türkiye

^{*}(nkeklikcioglu@cumhuriyet.edu.tr)

ABSTRACT

Sterilization is a critical process in medical technology, ensuring the elimination of viable microorganisms from materials and devices to prevent contamination before clinical application. This study provides an in-depth look into various sterilization methods. While methods like heat and ethylene oxide have long been utilized, their drawbacks, such as material degradation and toxicity, have spurred the development of advanced alternatives like gas plasma and pulsed light. Understanding these effects is paramount for selecting the optimal sterilization method to ensure both product safety and long-term material integrity for biomedical applications.

Keywords – Sterilization, Ethylene Oxide, Poly(Lactic-Acid) (PLA).

INTRODUCTION

Sterilization plays a vital role in ensuring the safety of medical devices, pharmaceuticals, and healthcare facilities. Its purpose is to eliminate all forms of microbial life, including bacteria, viruses, spores, and fungi, from surfaces, instruments, and materials [1]. While traditional sterilization methods like moist heat (autoclaving), dry heat, and chemical sterilants have been used for decades, the emergence of new polymeric materials and the demand for low-temperature processes have driven innovations in sterilization technologies. This paper explores conventional and advanced sterilization methods and analyzes their effects on biocompatible polymer materials, particularly poly(lactic acid) (PLA) and cyclic olefin copolymers (COCs) [2-3].

Medical devices utilized in patient diagnostics and treatments can serve as carriers of infectious microorganisms, leading to hospital-acquired infections (HAIs) through direct or indirect contact. HAIs affect millions of patients annually in countries, incurring substantial healthcare costs and significantly impacting patient well-being and quality of life. Severe HAIs can escalate to life-threatening organ dysfunction such as sepsis, underscoring the urgent need for effective sterilization and disinfection. In light of the recent COVID-19 epidemic, the importance of these techniques for human health has gained even greater attention [4]. Therefore, applying economical and effective sterilization techniques is essential to control environmental pollution and safeguard lives. Sterilization is crucial for controlling microorganisms in liquids, gases, and on surfaces, and their widespread use has played a major role in reducing the incidence of infectious diseases like pneumonia, gastroenteritis, and healthcare-associated illnesses [3].

OVERVIEW OF STERILIZATION METHODS

There are two types of sterilizing methods utilized in healthcare facilities: high-temperature and low-temperature. But the most recent advancements in sterilization technology used in medical facilities have mostly concentrated on low temperature sterilization systems. Low-temperature procedures are typically used for medical equipment that can not tolerate high temperatures ($>60\text{ }^{\circ}\text{C}$) and high humidity levels. Ethylene oxide and hydrogen peroxide are examples of gaseous chemical sterilants used in low temperature sterilization procedures. Hot steam under pressure (autoclaving) is typically used in high temperature sterilizing procedures [1].

High-Temperature Sterilization

These processes typically utilize hot steam under pressure (autoclaving). They are primarily applied to medical and surgical devices made of heat-stable materials.

Dry Heat Sterilization: This method is generally performed at high temperatures, approximately $160\text{ }^{\circ}\text{C}$ for about 2 hours, though duration and temperature vary based on targeted microorganisms. The mechanism involves the coagulation of microbial proteins. Advantages include less operational complexity, no need for pressure vessels or exterior jackets, and lighter weight. However, it requires more time, is a slower process, and is specific to certain materials. It can be used for heat-resistant polymers, but high temperatures can cause thermal transitions like melting or softening, so temperatures must be below the polymer's melting and degradation points. Dry heat is suitable for materials damaged by steam, such as powders, sharp instruments, petroleum products, and certain containers where steam cannot be used. It is also used in hospitals, space technology, and the pharmaceutical industry for steel instruments, glass syringes, and metal scalpels. Ovens are the simplest source for dry heat sterilization, requiring even temperature distribution, often aided by a fan. Infrared heaters and microwave radiation have also been used for dry heat sterilization, though microwaves can result in uneven heating. Dry heat is not as effective as steam sterilization at the same temperature [4].

Moist Heat Sterilization (Autoclaving): This is considered the oldest and safest known method of sterilizing medical equipment, using very high temperatures. In a steam sterilization autoclave, temperatures can reach $121\text{--}148\text{ }^{\circ}\text{C}$ with approximately 15 P.S.I. pressure. Steam under pressure has a greater penetration effect on microorganisms and their spores. The process has an inverse relationship between time and temperature, with cycle time depending on equipment size and temperature. Autoclaving is effective for hard items, surgical instruments (not moisture sensitive), wrapped items, liquids in vented containers, waste, and glassware. The basic mechanism is

the destruction of microorganisms by irreversible coagulation and denaturation of enzymes and structural proteins by high-temperature steam. Moist heat, in the form of steam, is widely used, being non-toxic, inexpensive, sporicidal, and rapidly microbicidal. The effectiveness of steam sterilizers is monitored using biological indicators containing *Geobacillus stearothermophilus* spores. Gravity displacement autoclaves (GDA) and high-speed pre-vacuum autoclaves (HSPA) are the basic types of steam sterilizers [4,5].

Low-Temperature Sterilization (LTS)

These processes are generally applied to medical devices that can not withstand high temperatures (>60 °C) and high humidity. LTS relies on chemicals rather than physical treatments for sterilization. Common examples of gaseous chemical sterilants include ethylene oxide (ETO) and hydrogen peroxide.

Ethylene Oxide (ETO): Used as a sterilant for LTS processes since the 1950s for temperature and moisture-sensitive devices. It can be used in combination with stabilizing gases like carbon dioxide, hydrochlorofluorocarbons, immersion in peracetic acid, and gas plasmas. ETO is effective for porous materials due to its penetration capability. It has virucidal, sporicidal, fungicidal, and bactericidal properties, acting as an alkylating agent [1,6].

Hydrogen Peroxide (H₂O₂): Hydrogen peroxide-based sterilizers are used in LTS processes. The Sterrad Sterilizer System, for example, uses hydrogen peroxide vapors and plasma to sterilize heat and moisture-sensitive devices. Another sterilizer, STERIZONE VP4, uses a multiphase process with both ozone and hydrogen peroxide, where ozone reacts with residual hydrogen peroxide to form hydroxyl radicals. Hydrogen peroxide is eco-friendly, degrading into oxygen and water. It deactivates various microorganisms, including fungi, yeast, bacteria, spores, and viruses. It oxidizes the outer cell of bacteria or viruses, damaging their outer walls [7].

Nitrogen Dioxide (NO₂) gas sterilization: This is a recent advancement, offering advantages like low sterilant concentration, operation at room temperature, fewer sterilant residues, and fast microbicidal activity. It works as a powerful oxidizing agent at room temperature and requires about one percent of ambient pressure gas, preventing condensation. NO₂ sterilization is effective under vacuum conditions due to improved gas flow, penetration rate, and air elimination.

Radiation-Based Sterilization

Gamma irradiation and electron beam sterilization are used extensively for pre-packaged disposable medical products. Ionizing radiation disrupts microbial DNA, rendering them nonviable. Gamma rays, typically emitted from cobalt-60 sources, penetrate deep into materials, making them suitable for bulk sterilization. However, the high energy levels involved can damage sensitive polymers, causing chain scission and oxidation [8].

STERILIZATION EFFECTS ON PLA-BASED BIOPLASTICS

Poly(lactic acid) (PLA) is a biodegradable, biocompatible thermoplastic derived from renewable sources. It is increasingly used in medical applications, including surgical implants and drug delivery systems. PLA's response to sterilization is highly dependent on the method employed.

Krug et al. (2024) investigated the degradation behavior of PLA after EtO and gamma irradiation sterilization, followed by accelerated aging [11]. The study found that:

- Gamma irradiation caused significant molecular weight reduction due to chain scission in the amorphous regions.
- Crystallinity increased as degraded chains reorganized.
- Thermal and mechanical properties declined, leading to embrittlement.
- Discoloration occurred, particularly in PLA types containing plasticizers.

In contrast, EtO-sterilized PLA exhibited only minor moisture uptake and slight crystallinity increase, with no substantial degradation. These results suggest that EtO is a more compatible sterilization option for maintaining PLA's structural and functional integrity during shelf-life.

EFFECTS OF GAMMA IRRADIATION ON COC MATERIALS

Cyclic olefin copolymers (COCs) are a class of amorphous thermoplastics valued for their optical clarity, chemical resistance, and low moisture absorption. Their application in diagnostic devices and pharmaceutical packaging has grown, especially where sterilization is required.

Zhang et al. (2024) evaluated the impact of gamma radiation (up to 30 kGy) on COCs with varying norbornene contents [12]. The findings indicated:

- Increased norbornene content led to higher concentrations of radiation-induced free radicals.
- Oxidative degradation intensified, resulting in color changes (yellow-green tint) and lowered glass transition temperatures.
- Cross-linking dominated in COCs with lower norbornene levels, while chain scission prevailed in those with higher norbornene.
- Melt flow index and thermal stability shifted significantly, indicating macromolecular structural changes.

These changes highlight the need to tailor sterilization doses and methods based on COC composition to preserve desired material properties.

IMPLICATIONS FOR MEDICAL DEVICE DESIGN AND SHELF-LIFE

Sterilization compatibility is a critical consideration in the design of polymer-based medical devices. The sterilization method not only affects immediate functionality but also influences long-term aging, shelf-life, and regulatory approval.

Accelerated aging studies (ASTM F1980-21) simulate long-term storage conditions to assess degradation. Krug et al. (2024) used this approach to demonstrate that sterilization-induced changes in PLA significantly influenced aging kinetics [11]. The degradation proceeded in two stages, with a rapid decline in mechanical properties during the second phase, especially in gamma-irradiated samples.

For manufacturers, this means:

- Selecting sterilization techniques based on polymer sensitivity.
- Conducting aging tests post-sterilization.

- Adjusting packaging and storage conditions to mitigate degradation.

EMERGING TRENDS IN STERILIZATION TECHNOLOGIES

Recent innovations aim to combine multiple sterilization mechanisms to enhance efficacy and material compatibility. Examples include:

- Dual sterilant systems (ozone + H₂O₂) for broad-spectrum action.
- Plasma-enhanced disinfection for complex geometries.
- Microwave-assisted sterilization for PPE reuse.

Such hybrid systems are promising for next-generation biodegradable and high-performance polymers but require more research into their long-term effects on device materials and function [1-5].

CONCLUSION

Sterilization technologies have evolved to meet the growing demands of modern healthcare, especially with the increasing use of sensitive polymeric materials. While traditional methods like autoclaving remain relevant, low-temperature and radiation-based techniques offer greater flexibility for advanced materials. However, they can significantly impact the structural and functional integrity of polymers like PLA and COC. Therefore, material-specific sterilization protocols and aging assessments are essential to ensure safety, performance, and regulatory compliance. In conclusion, the goal of sterilization techniques is to eliminate all living germs by the use of low-temperature chemical treatments like ethylene oxide, hydrogen peroxide, and nitrogen dioxide gas, or high-temperature approaches. Pulsed light, ultrahigh pressure, gas plasma, supercritical fluid sterilization, and photocatalytic/catalytic ozone oxidation are examples of advanced procedures that provide efficient solutions and typically have the benefits of reduced processing times and the lack of hazardous consequences. They may, nevertheless, also have certain restrictions. For the particular sample under study, each needs to be meticulously designed. Especially, impacts of materials on surfaces should be assessed in sterilization investigations since certain alterations may reduce the material's lifespan or alter its characteristics. Additionally, better sterilizing methods can even enhance surface cleaning qualities.

ACKNOWLEDGMENT

The authors are grateful to thank company Estaş for coming up with the idea of such a study while performing experimental sterilization.

REFERENCES

- [1] Bharti, B., Li, H., Ren, Z., Zhu, R., & Zhu, Z. (2022). Recent advances in sterilization and disinfection technology: A review. *Chemosphere*, 308, 136404.
- [2] Rutala, W. A., & Weber, D. J. (2013). Disinfection and sterilization: an overview. *American journal of infection control*, 41(5), S2-S5.
- [3] Dempsey, D. J., & Thirucote, R. R. (1988). Sterilization of medical devices: a review. *Journal of biomaterials applications*, 3(3), 454-523.
- [4] Barcelo, D. (2020). An environmental and health perspective for COVID-19 outbreak: meteorology and air quality influence, sewage epidemiology indicator, hospitals disinfection, drug therapies and recommendations. *Journal of Environmental Chemical Engineering*, 8(4), 104006.
- [5] Rutala, W. A., Donskey, C. J., & Weber, D. J. (2023). Disinfection and sterilization: New technologies. *American Journal of Infection Control*, 51(11), A13-A21.
- [6] Rodrigues, M. M., Baldin, E. K. K., Fontoura, C. P., Leidens, L. M., Barbieri, R. A., Frassini, R., ... & Aguzzoli, C. (2020). Overview of sterilization methods for UHMWPE through surface analysis. *Materials Advances*, 1(9), 3243-3255.
- [7] Gardner, M. G., & Serpell, M. (2022). Disinfection, sterilization and single use. *Anaesthesia & Intensive Care Medicine*, 23(10), 571-574.
- [8] Gomes, A. D., de Oliveira, A. A., Houmard, M., & Nunes, E. H. (2021). Gamma sterilization of collagen/hydroxyapatite composites: Validation and radiation effects. *Applied Radiation and Isotopes*, 174, 109758.
- [9] Babaei, M., Ebrahim-Najafabadi, N., Mirzadeh, M., Abdali, H., Farnaghi, M., Gharavi, M. K., ... & Poursamar, S. A. (2024). A comprehensive bench-to-bed look into the application of gamma-sterilized 3D-printed polycaprolactone/hydroxyapatite implants for craniomaxillofacial defects, an in vitro, in vivo, and clinical study. *Biomaterials Advances*, 161, 213900.
- [10] Rodrigues, M. M., Baldin, E. K. K., Fontoura, C. P., Leidens, L. M., Barbieri, R. A., Frassini, R., ... & Aguzzoli, C. (2020). Overview of sterilization methods for UHMWPE through surface analysis. *Materials Advances*, 1(9), 3243-3255.
- [11] Krug, N., Zarges, J. C., & Heim, H. P. (2024). Influence of ethylene oxide and gamma irradiation sterilization processes on the degradation behaviour of poly (lactic acid)(PLA) in the course of artificially accelerated aging. *Polymer Testing*, 132, 108362.
- [12] Zhang, F., Dong, C., Lei, H., Guo, F., Shen, R., Xing, Z., & Wu, G. (2024). Effects of gamma radiation on cyclic olefin copolymers with varied norbornene content: Impacts on structure and properties at sterilization doses. *Polymer Degradation and Stability*, 227, 110881.

Çinko Ftalosiyanın Yüklü MCM-41 Heterojen Katalizörü ile Çevre Dostu Koşullarda 1,4-Naftakinon Eldesi

Yaşar GÖK¹
Recep ERDEM²

- 1- Prof. Dr.; Burdur Mehmet Akif Ersoy Üniversitesi Fen Edebiyat Fakültesi Kimya Bölümü. yasargok@mehmetakif.edu.tr ORCID No: 0000-0003-3134-7560
- 2- Yüksek Lisans Öğrenci; Burdur Mehmet Akif Ersoy Üniversitesi Fen Bilimleri Enstitüsü, Kimya Anabilim Dalı. mail@mehmetakif.edu.tr ORCID No:

ÖZET

Organik sentez kimyasında, çevre dostu, ekonomik ve sürdürülebilir tekniklerin geliştirilmesi oldukça önemlidir. Özellikle seçici oksidasyon süreçlerinde, geleneksel oksitleyici maddeler yerine ışıqla aktive edilen moleküler oksijenin kullanılması, yeşil kimya prensipleriyle uyumlu yenilikçi yöntemler ortaya koymaktadır. Bu tür görünür ışık destekli foto-oksidasyon tepkimelerinde, metalloftalosiyeninler fotosensitizer olarak ön plana çıkmakta; yüksek ışık soğurma kapasiteleri, kimyasal dayanıklılıkları ve çevreye duyarlı yapıları sayesinde tercih edilmektedir. Bu çalışmada, MCM-41 destekli çinko ftalosiyenin (ZnPc) içeren heterojen fotokatalizörün 1-naftolün fotooksidasyonu ile 1-naftakinonun elde edildiği model reaksiyondaki katalitik performansının incelenmesi sunulmaktadır. Heterojen katalizör, MCM-41'in 3-kloropropiltrietoksilan (CPTES) ile fonksiyonelleştirilmesiyle elde edilen MCM-41-Cl üzerinde ZnPc'nin hareketsizleştirilmesi ile hazırlanmıştır. Elde edilen MCM-41-ZnPc fotokatalizörünün fotokatalitik performansı, görünür ışık altında 1-naftolün 1,4-naftokinona seçici oksidasyonunda değerlendirilmiştir. Fotooksidasyon deneyleri laboratuvar tipi bir fotoreaktör kullanılarak gerçekleştirilmiştir. Işık kaynağı olarak ise ticari olarak temin edilebilen, 630–660 nm dalga boyuna sahip 200 W gücünde kırmızı LED ışık kullanılmıştır.

Heterojen fotokatalizör, oksidant olarak hava kullanıldığında, 15 dakikada %78 dönüşüm ve %99'dan fazla seçicilik sağlamıştır. Kontrol deneyleri, ışık, oksijen ve ftalosiyenin bileşiminin 1-naftolün fotooksidasyonu için temel gereksinimler olduğunu göstermiştir. Katalizör, birden fazla kullanımda yüksek kararlılık ve sürdürülebilir özellik göstermektedir. Farklı tip çözücülerde iyi performans göstermesine karşın en yüksek aktivite asetonitril çözücüsünde elde edilmiştir. MCM-41'in destek olarak kullanılması, agregasyon sorunlarını etkili bir şekilde en aza indirmekte ve katalizör dispersiyonunu iyileştirerek fotokatalitik verimliliği artırmaktadır. Bu çalışma, yeşil kimyasal sentez için pratik ve ölçeklenebilir çözümler olarak özel fotoreaktörlerle birleştirilmiş düşük maliyetli heterojen sistemlerin potansiyelinin vurgulanmasında önemli bir yer tutmaktadır.

Anahtar Kelimeler – Fotokatalizör, Ftalosiyenin, Organik Sentez, Fotoreaktör, Yükseltgenme.

GİRİŞ

Tarım, gıda ve sağlık gibi birçok alanda kullanılan işlevsel moleküllerin üretimi, organik sentetik kimyanın temel uygulama alanlarından birini oluşturmaktadır (Chojnacka, 2024:100898). Bu alanda önemli teknolojik ilerlemeler sağlanmış olmasına rağmen, hedef bileşiklerin sentezi hâlâ zaman açısından oldukça maliyetli ve zahmetli bir süreçtir

(Devanshi vd., 2024:246). Üstelik, uygulanan bazı sentetik yöntemler çevreye zarar verebilecek unsurlar barındırmaktadır (Dutta vd., 2024:120103). Bu nedenle hem doğayla uyumlu hem de insan sağlığına olumsuz etkisi olmayan alternatif üretim stratejilerinin geliştirilmesi gerekliliği gün geçtikçe daha da önem kazanmaktadır.

Fotokataliz, yeşil kimya kapsamında, ışık enerjisini kimyasal enerjiye dönüştürebilme özelliğiyle öne çıkan etkili bir yöntemdir (Oh ve Stache, 2022:5745). Bu yaklaşım, organik tepkimelerin daha az enerji tüketen, daha hafif koşullarda ve çevresel etkileri en aza indirerek gerçekleşmesine imkân tanır. Özellikle görünür ışık altında yürütülen fotooksijenasyon reaksiyonları, organik bileşiklere oksijen kazandırarak, ilaç üretiminde değerlendirilebilecek önemli yapıların sentezine katkı sağlar. Bu yöntem, geleneksel olarak kullanılan hidrojen peroksit veya tert-butil hidroperoksit gibi oksitleyicilere ihtiyaç duymadan daha çevre dostu bir çözüm sunmaktadır (Yu vd., 2025:774).

Fotooksijenasyon reaksiyonunun gerçekleşmesi için yalnızca moleküler oksijen ve görünür ışık spektrumunu soğurabilen bir katalizör yeterlidir. Ancak çoğu organik bileşik görünür ışığı doğrudan absorplayamaz; bu nedenle, bu tür dönüşümler için ışığı etkin biçimde yakalayabilen özel kimyasal yapılar gereklidir. Bu yapılar, "fotosensitizer" olarak adlandırılır (Nguyen vd., 2022:3324). Porfirinler (Akbar vd., 2023:114648), Rose Bengal (Body vd., 2023:114648), fullerener (Hou vd., 2022:13), Ru(II) kompleksleri (Ankathatti Munegowda vd., 2022:214712) ve metaloftalosiyeninler (Channabasavana Hundi Puttaningaiah ve Hur 2024:113491) yaygın olarak kullanılan fotosensitizer örnekleridir. Bu bileşikler, görünür ışığı emdikten sonra enerjiyi moleküler oksijene aktararak singlet oksijen üretimini sağlar ve bu da seçici ve çevreyle uyumlu oksidasyon reaksiyonlarının gerçekleşmesine olanak tanır. Singlet oksijen, çevre dostu ve ekonomik organik sentez yöntemlerinin temel bileşenlerinden biridir. Bunun yanı sıra, su arıtımı (Nidheesh vd., 2025:195) ve fotodinamik kanser tedavisi (Cui vd., 2024:1274) gibi doğrudan insan yaşam kalitesine etki eden alanlarda da önemli bir rol oynamaktadır.

Metaloftalosiyeninler, görünür spektrumun kırmızı bölgesinde yüksek molar absorpsiyon katsayılarına sahip olmaları (Moreira vd., 2008:741; Gök, 2014:750; Gök vd., 2023:1887), Ru(II) komplekslerine (Ravelli vd., 2013:97) kıyasla çevreye duyarlı yapıları ve diğer organik boyalara göre üstün termal ve foto kararlı özellikleri sayesinde oldukça çekici fotosensitizerlerdir (Zheng vd., 2021:213548). Ancak, yaygın çözücülerde düşük çözünürlükleri ve çözeltide agregasyon eğilimleri, bu bileşiklerin pratik uygulamalarını sınırlayan temel sorunlar arasında yer almaktadır (Li vd., 2018:2098; Gök ve Gök, 2019:55). Homojen fotokataliz sistemlerinde bu sınırlayıcı özellikler; katalizörün geri kazanım zorluğu, yüksek konsantrasyonlarda ışık penetrasyonunun azalması ve foto kararlılığının düşmesi gibi problemlere yol açmaktadır (Croxall vd., 2023:1463). Bu

sorunlara çözüm olarak, son yıllarda heterojen fotokatalizörler büyük ilgi görmüştür. Geri dönüştürülebilirlikleri, artırılmış kararlılıkları ve endüstriyel uygulamalarda maliyet etkinlikleri nedeniyle heterojen sistemler tercih edilmektedir (Kou vd., 2017:1445).

Heterojen fotokatalizörler, katalitik olarak aktif türlerin uygun bir destek malzemesi üzerinde hareketsizleştirilmesi yoluyla hazırlanır. Günümüze kadar nanopartiküller (Schätz vd., 2010:8950), magnezyum oksit (Julkapli ve Bagheri 2016:1), titanyum dioksit (Bagheri vd., 2014:727496), grafen (Julkapli ve Bagheri 2015:948) ve mezogözenekli malzemeler (Pal 2015:24363) gibi çeşitli destek malzemeleri kullanılmıştır. Destek malzemesinin seçimi, hedef uygulamaya ve istenen özelliklere göre değişiklik göstermektedir. MCM-41 (Mobil Composition of Matter No. 41), düzenli mezogözenekli yapıya sahip silika bazlı bir malzemedir. 1992 yılında Mobil Oil Corporation araştırmacıları tarafından keşfedilmiş, gözenek boyutları 2 ila 10 nanometre arasında değişen, oldukça düzenli ve büyük yüzey alanına sahip bir malzemedir (Beck vd., 1992:10834). Yapısal olarak hekzagonal mezogözenek yapısı ile bilinir, bu da düzenli silindirik gözenekler anlamına gelir. MCM-41, kimyasal ve yapısal özellikleri sayesinde çok çeşitli uygulamalarda kullanılabilecek esnek bir malzemedir. Yüksek yüzey alanı, düzenli mezogözenek yapısı ve kimyasal kararlılığı ile kataliz, ilaç taşıma, çevresel temizlik ve sensör teknolojileri gibi birçok alanda büyük bir potansiyele sahiptir. Literatür, heterojen fotokatalizörlerin zaman zaman homojen muadillerine kıyasla daha yüksek katalitik aktivite gösterebildiğini ortaya koymuştur (Ma vd., 2023:4285).

Bu bağlamda, çözünürlük ve agregasyon sorunları nedeniyle homojen sistemlerde düşük aktiviteye sahip ftalosiyanın bileşiklerinin uygun bir yüzeyde hareketsizleştirilmesi, fotokatalitik performanslarının artırılması açısından etkili bir strateji olarak değerlendirilmektedir. Nitekim literatürde, farklı destek malzemeleri kullanılarak ftalosiyanın bazlı heterojen fotokatalizörlerin sentezine ve bu malzemelerin çeşitli organik dönüşüm reaksiyonlarındaki performansına dair birçok çalışma mevcuttur (Szymczak ve Kryjewski 2022:2532; Aralekallu ve Koodlur Sannegowda 2024: 2400088). Bu çalışmalardan bazıları, 1-naftolün fotooksidasyonu üzerine odaklanmıştır (Chen ve Ng 2022:3567; Gök vd., 2025: e202500207). Özellikle destek malzemesi olarak MCM-41'in bir ftalosiyanın bileşiği ile birleştirilmesiyle elde edilen bir heterojen fotokatalizörün, 1-naftolün fotooksidasyonu üzerindeki etkisi dikkate değer önem taşımaktadır.

Bu çalışmada, MCM-41 destek malzemesine immobilize edilmiş bir heterojen fotokatalizör olan MCM-41-ZnPc'in fotokatalitik performansı sunulmaktadır. Katalizör, 1-naftolün görünür ışık altında gerçekleştirilen fotooksidasyonu için test edilmiştir. Tüm deneyler, 3B yazıcı teknolojisi kullanılarak üretilen ve kırmızı güç LED'i ile donatılmış, özel tasarlanmış düşük maliyetli bir fotoreaktörde gerçekleştirilmiştir.

Deneysel Çalışmalar

Materyal ve Metot

Çalışmada kullanılan MCM-41, daha önce grubumuz tarafından yapılan çalışma kapsamında sentezlenmiş bu çalışmada da kullanılmıştır (Gök ve Gök, 2024:e7359). MCM-41-ZnPc heterojen fotokatalizörü literatürde sunulan çalışma kapsamında sentezlenmiş olup (Gök vd., 2025:e00411), 1-naftolün fotooksidasyonundaki aktivitesi bu çalışma kapsamında incelenmiştir. Çalışma kapsamında kullanılan ticari kimyasallar yurtdışı kimyasal tedarikçilerinden temin edilmiş olup, çözücüler Armarego'da verilen yöntemler takip edilerek saflaştırıldı veya kurutuldu (Armarego, 2022).

Çalışma kapsamında elde edilen malzemelerin FT-IR spektrumları, Shimadzu IR Affinity-1S cihazında KBr disk tekniği yardımı ile 400-4000 cm^{-1} aralığında kaydedilmiştir. Malzemelerin hazırlanmasında IKA RCT Basic marka ısıtıcılı manyetik karıştırıcı kullanılmıştır. Kurutma işlemleri, Memmert marka etüvde, yakma işlemleri ise Nükleon marka kül fırınında yapılmıştır. Çözücü uzaklaştırma işlemlerinde IKA RV8 model döner buharlaştırıcı kullanılmıştır. 1-naftolün 1,4-naftokinon'a dönüşümü, diyet dizisi dedektörü (DAD) ve YMC Amiloz-C kolonu ile donatılmış bir Shimadzu Prominence LC-20A yüksek performanslı sıvı kromatografisi sistemi kullanılarak izlendi. Fotokatalitik çalışmalar için 200 W gücünde kırmızı güç LED'i kullanıldı.

1-naftolün MCM-41-ZnPc ile Fotooksidasyonu

1-naftolün 1,4-naftokinona fotooksidasyonu, heterojen katalizör MCM-41-ZnPc 'in fotokatalitik verimliliğini değerlendirmek için bir model reaksiyon olarak kullanılmıştır. Her deneyde, atmosferik oksijene maruz bırakılan açık tüplere MCM-41-ZnPc (8 mg), değişen miktarlarda 1-naftol (0,03-0,6 mmol) ve uygun bir reaksiyon çözücüsü eklenmiştir. Reaksiyon karışımları daha sonra ilgili tablolarda belirtilen süreler boyunca kırmızı LED ışıkla (640 nm) ışınlanmıştır. Reaksiyon tamamlandıktan sonra 0,1 mL numune alınmış, izopropil alkol ile 1 mL'ye seyreltilmiş ve bir şırınga filtresi kullanılarak filtrelenmiştir. Elde edilen çözeltiler, DAD detektörlü bir Shimadzu Prominence LC-20A HPLC sistemi veya Rxi-5 ms kolonu ile donatılmış bir Shimadzu GC-2010 gaz kromatografisi kullanılarak analiz edildi. Dönüşüm oranları ve ürün seçiciliği, ekteki tablolarda sunulduğu gibi, kromatografik pik alanlarının entegre edilmesiyle hesaplandı.

BULGULAR VE TARTIŞMA

Önceki çalışmalar, çinko ftalosiyanın bileşiklerinin, uygun dalga boyundaki ışıkla ışınlığında bir enerji transfer mekanizması yoluyla temel haldeki moleküler oksijeninden singlet oksijen üretebildiğini göstermiştir (Wysocki vd., 2025:112751). MCM-41-ZnPc fotokatalizörünün 684 nm'de güçlü bir emilim bandı sergilediği göz önüne alındığında, uygun ışık ışınlımı altında aerobik oksidasyon reaksiyonlarında katalitik aktivite gösterebileceği düşünülebilir. Bunu test etmek için, 1-naftolün 1,4-naftokinon'a fotooksijenasyonu model bir reaksiyon olarak seçilmiştir. Başlangıçta, MCM-41-ZnPc 'nin fotokatalitik aktivitesi, asetonitril içinde 100:1'lik bir substrat-katalizör mol oranı kullanılarak açık havada değerlendirilmiştir (Tablo 1, 1–5. denemeler).

Tablo 1 Heterojen fotokatalizör MCM-41-ZnPc, MCM-41 varlığında ve katalizörsüz ortamda açık havada 1-naftolün fotokatalitik oksidasyonu^a

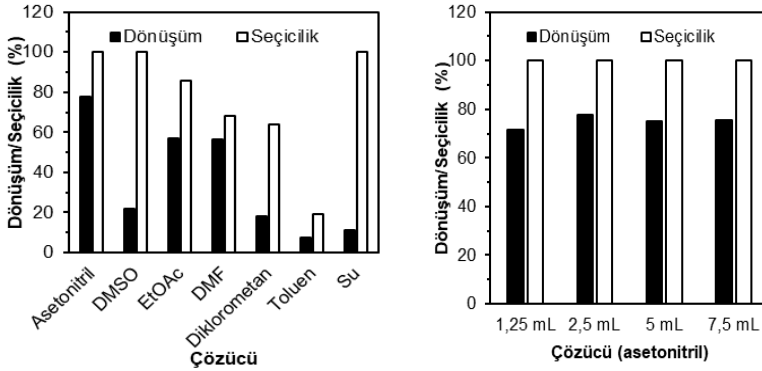
Deneme	Katalizör	Dönüşüm (%) ^b	1,4- naftakinon (%)	Seçicilik (%)
1	-	6,88	6,88	100
2	MCM-41	11	11	100
3	MCM-41-ZnPc	77,63	77,63	100
4	MCM-41-ZnPc ^c	13,46	13,46	100
5	MCM-41-ZnPc ^d	13,41	13,41	100

^aReaksiyon şartları: çözücü: asetonitril (1,25 mL), 1-naftol (0,03 mmol), katalizör (8 mg), substrat/katalizör oranı: 100/1, 200W LED 15 dakika için O₂ varlığında (hava). ^bDönüşüm HPLC ile belirlendi. ^cFotoreaktör kullanılmadan ortam ışığında. ^dKaranlıkta

Sonuçlar, hem MCM-41-ZnPc katalizörünün varlığının hem de ışık ışınlımının verimli fotooksidasyon için gerekli olduğunu ortaya koymuştur. 15 dakikalık ışık maruziyeti altında sistem, %100 seçicilikle %77,63'lük yüksek bir dönüşüm değerine ulaşmıştır (Tablo 1, deneme 3). Buna karşılık, MCM-41-ZnPc, çıplak MCM-41 ile değiştirildiğinde (dönüşüm: %11) veya tamamen çıkarıldığında (dönüşüm: %6,88) dönüşümlerde büyük oranda düşüş kaydedilmiştir; bu da ZnPc kısmının fotoaktif merkez olarak önemli bir role sahip olduğunu göstermektedir (Tablo 1, deneme 1 ve 2). Karanlıkta veya ortam ışığında, herhangi bir dönüşüm elde edilememiştir (Tablo 1, deneme 4 ve 5), bu da reaksiyonun ışığa bağlı olduğunu göstermektedir. Bu bulgular, ışık ışınlımının, havanın (oksijen kaynağı olarak) ve MCM-41-ZnPc

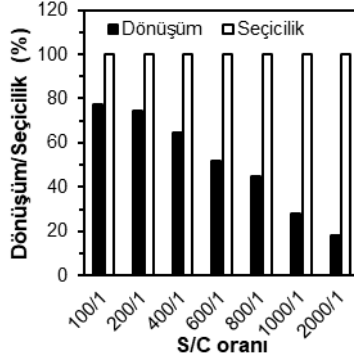
fotokatalizörünün varlığının, 1-naftolün etkili ve seçici fotooksidasyonu için gerekli olan parametreler olduğunu doğrulamaktadır.

İdeal çözücüü belirlemek için reaksiyon aynı koşullar altında farklı çözücüler içinde gerçekleştirildi (Şekil 1a). Ürün seçiciliğinin tüm durumlarda yüksek kaldığı gözlenirken, dönüşüm verimliliğinin önemli ölçüde değiştiği gözlenmiştir. En yüksek dönüşümün asetonitrilin çözücüsü içinde olduğu belirlenmiştir. Farklı hacimlerde asetonitril ile tekrarlanan reaksiyonlar, çözücü hacmindeki değişimin dönüşüm ve seçicilik değerlerini etkilemediğini göstermiştir (Şekil 1b).



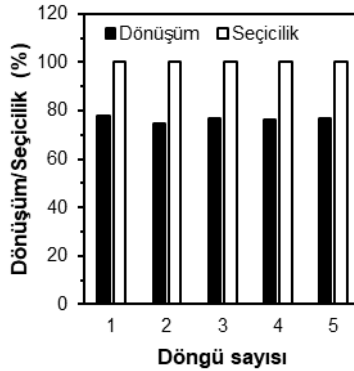
Şekil 1 a) Çözücü türünün ve b) asetonitril çözücü miktarının dönüşüm ve seçicilik üzerindeki etkisi.

Ayrıca, substrat konsantrasyonunun etkisi yine aynı şartlarda incelendi. 1-naftol miktarının artırılmasının, seçiciliği etkilemese de dönüşümde bir azalmaya neden olduğu gözlenmiştir (Şekil 2). 100:1'lik substrat-katalizör oranında, 15 dakikadaki en yüksek dönüşüm %77,63 olurken, 2000:1 gibi daha yüksek oranda, seçicilik aynı kalmasına karşın dönüşümün ciddi oranda düştüğü (%17,85) belirlenmiştir. Test edilen tüm koşullarda, ürün seçiciliği yüksek elde edilmiş fakat substrat oranının artırılmasıyla dönüşümün azaldığı belirlenmiştir.



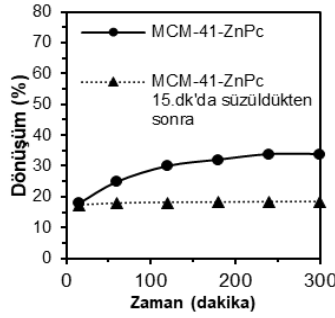
Şekil 2 Heterojen fotokatalizör MCM-41-ZnPc ile 1-naftolün fotokatalitik oksidasyonunda substrat/katalizör oranının dönüşüm seçicilik üzerine etkisi

Sürdürülebilir heterojen kataliz için temel gereklilik, katalizörün yeniden kullanılabilirliğidir. MCM-41-ZnPc'nin kararlılığını ve tekrar kullanılabilirliğini değerlendirmek için süzme ve yeniden kullanım testleri gerçekleştirildi. Fotokatalitik reaksiyon sonrası katalizör süzme işlemi ile geri kazanıldı ve beş ardışık fotokatalitik döngüde tekrar kullanıldı. Elde edilen sonuçlar, her döngü sonrası yüksek dönüşüm ve seçicilik değerlerinin korunduğunu ortaya koymuştur. Bu da katalizörün kararlılığını göstermektedir (Şekil 3).



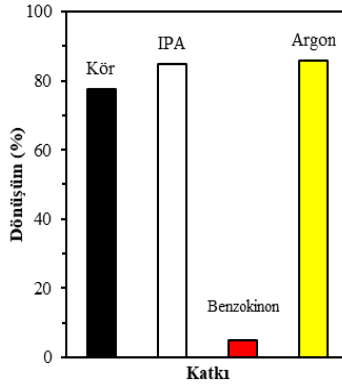
Şekil 3 MCM-41-ZnPc'nin yeniden kullanılabilirlik testi

Katalizörün heterojen yapısını bütünlüğünü görmek ve reaksiyonun ilerleyişi sırasında ortamdan uzaklaştırılması durumunda reaksiyon ilerleyişinin durup durmadığını belirlemek için sıcak süzme testi gerçekleştirildi. MCM-41-ZnPc reaksiyon karışımından 15 dakika sonunda süzülerek uzaklaştırılması durumunda, ürün oluşumunun durduğu görülmüştür (Şekil 4). Bu da aktif türlerin katı destek üzerinde hareketsiz olarak kaldığını ve heterojen bütünlüğün bozulmadığını göstermektedir.



Şekil 4 Heterojen katalizör MCM-41-ZnPc için sıcak filtrasyon testi

1-naftolün fotokatalitik oksidasyonundan sorumlu aktif türleri belirlemek için, radikal süpürücüler kullanılarak bir dizi kontrol deneyi yürütülmüştür. Işık ile uyarılma sonrası oluşan pozitif boşlukları (h^+), süperoksit radikallerini ($\bullet O_2^-$) ve hidroksil radikallerini ($\bullet OH$) söndürmek için sırasıyla etilendiamintetraasetik asit (EDTA), benzokinon ve izopropanol (IPA) kullanılmıştır. Elde edilen sonuçlar Şekil 5'de gösterilmektedir. EDTA ve IPA ilavesinin reaksiyon hızı üzerinde ihmal edilebilir bir etkisi olmuştur. Buna karşılık, benzokinon varlığı ürün oluşumunu önemli ölçüde engellemiş ve reaksiyonu neredeyse tamamen bastırmıştır. Bu sonuçlar, süperoksit radikallerinin ($\bullet O_2^-$) fotokatalitik süreci yönlendirmede baskın bir rol oynadığını açıkça göstermektedir.



Şekil 5 Heterojen katalizör MCM-41-ZnPc için radikal süpürme testi

SONUÇ

Bu çalışma, MCM-41 destekli ZnPc heterojen fotokatalizörünün görünür ışık altında, hava atmosferinde 1-naftolün yüksek verim ve seçicilikle 1,4-naftokinona dönüştürülmesinde oldukça etkili olduğunu ortaya koymuştur. Reaksiyon koşullarının optimize edilmesiyle sistemin katalitik etkinlik değerleri oldukça yüksek bulunmuş, ayrıca yeniden kullanılabilirlik açısından güçlü bir performans sergilemiştir.

Bu bulgular, çevre dostu, düşük maliyetli ve pratik olarak uygulanabilir fotokatalitik sistemlerin geliştirilmesine önemli bir katkı sağlamaktadır. Grubumuzun çalışmaları bu yönde devam etmektedir.

REFERANSLAR

- Akbar, A., Khan, S., Chatterjee, T., Ghosh, M. (2023). Unleashing the power of porphyrin photosensitizers: Illuminating breakthroughs in photodynamic therapy. *J. Photochem. Photobiol. B* 248, 112796.
- Ankathatti Munegowda, M., Manalac, A., Weersink, M., McFarland, S. A., Lilge, L. (2022). Ru (II) containing photosensitizers for photodynamic therapy: A critique on reporting and an attempt to compare efficacy. *Coord. Chem. Rev.* 470, 214712.
- Aralekallu, K. P. C P, S., Koodlur Sannegowda, L. (2024). Efficacy of Phthalocyanine-Based Catalysts in Electrochemical Sensors: A Comprehensive Review. *Adv. Sens. Res.* 3, 2400088.
- Armarego, W. L. (2022). *Purification of laboratory chemicals: Part 2 inorganic chemicals, catalysts, biochemicals, physiologically active chemicals, nanomaterials*. Butterworth-Heinemann.
- Bagheri, S., Muhd Julkapli, N., Bee Abd Hamid, S. (2014). Titanium Dioxide as a Catalyst Support in Heterogeneous Catalysis. *Sci. World J.* 2014, 727496.
- Beck, J. S., Vartuli, J. C., Roth, W. J., Leonowicz, M. E., Kresge, C. T., Schmitt, K. D., Schlenker, J. (1992). A new family of mesoporous molecular sieves prepared with liquid crystal templates. *Journal of the American Chemical Society*, 114(27), 10834-10843.
- Body, N., Lefebvre, C., Eloy, P., Haynes, T., Hermans, S., Riant, O. (2023). Impact of silica nanoparticles architectures on the photosensitization of O₂ by immobilized Rose Bengal. *J. Photochem. Photobiol. A: Chem.* 440, 114648.
- Channabasavana Hundi Puttaningiah, K. P., Hur, J. (2024). Opportunities and challenges of metal phthalocyanines composites in photodynamic therapy as photosensitizers: A comprehensive review. *Inorg. Chem. Commun.* 170, 113491.
- Chen, X.-F., Ng, D. K. P. (2021). β -Cyclodextrin-conjugated phthalocyanines as water-soluble and recyclable sensitizers for photocatalytic applications. *Chem. Commun.* 57, 3567-3570.

- Chojnacka, K. (2024). Sustainable chemistry in adaptive agriculture: A review. *Curr. Opin. Green Sustain. Chem.* 46, 100898.
- Croxall, M., Lawrence, R., Goh, C. (2023). Heterogeneous vs homogenous photocatalysis: what dominates in the degradation of methyl orange and methylene blue mixtures? *Photochem. Photobiol. Sci.* 22, 1463-1474.
- Cui, S., Guo, X., Wang, S., Wei, Z., Huang, D., Zhang, X., Zhu, T. C., Huang, Z. (2024). Singlet oxygen in photodynamic therapy. *Pharmaceuticals*, 17, 1274.
- Devanshi, M., Anju, S., Shruti, G., Reena, J., Soma Mondal, G., Yashna, D., Sumedha, S., Soni, R. (2024). Developments in synthesis strategies of spiro-barbiturate compounds: A classified study. *Mini Rev. Org. Chem.* 21, 246-270.
- Dutta, S., Adhikary, S., Bhattacharya, S., Roy, D., Chatterjee, S., Chakraborty, A., Banerjee, D., Ganguly, A., Nanda, S., Rajak, P. (2024). Contamination of textile dyes in aquatic environment: Adverse impacts on aquatic ecosystem and human health, and its management using bioremediation. *J. Environ. Manage.* 353, 120103.
- Gök, H. Z., Dönmez, S., Gök, Y. (2025). Photodegradation of Methylene Blue Using Zinc Phthalocyanine Supported on MCM-41 Under Visible Light in Low-Cost 3D Printed Photoreactor. *ChemistrySelect*, 10, e00411.
- Gök, Y., & Gök, H. Z. (2024). Preparation of mesoporous silica and organosilica nanostructures functionalized with C2-symmetric diol and their catalytic performance in diethylzinc addition to aromatic aldehydes. *Applied Organometallic Chemistry*, 38(3), e7359.
- Gök, Y., Arlı, O. T., Gök, H. Z., & Türkaslan, T. (2023). Rational synthesis of pH-responsive mesoporous organosilica nanoparticles functionalized with 2-aminothiophenol for controlled release of curcumin. *Journal of Porous Materials*, 30(6), 1887-1896.
- Gök, Y., Dönmez, S., Erdem, R., Gök, H. Z. (2025) Green Photooxidation of 1-Naphthol Using a Zinc Phthalocyanine-Loaded MCM-41 Heterogeneous Catalyst. *ChemPlusChem*. e202500207.
- Gök, H. Z., & Gök, Y. (2019). Novel polymeric phthalocyanines bridged flexible 1, 5-pentanedithiol unit for metal ions extraction: synthesis, characterization and evaluation. *Journal of Inclusion Phenomena and Macrocyclic Chemistry*, 94(1), 55-63.
- Gök, H. Z. (2015). Synthesis of metal-free and metallophthalocyanines containing 18- and 21-membered macrocycles with mixed donor atoms and their metal-ion binding properties. *Turkish Journal of Chemistry*, 39(4), 750-763.
- Hou, W., Shi, G., Wu, S., Mo, J., Shen, L., Zhang, X., Zhu, Y. (2022). Application of fullerenes as photosensitizers for antimicrobial photodynamic inactivation: a review. *Front. Microbiol.* 13, 2022.
- Julkapli, N. M., Bagheri, S. (2015). Graphene supported heterogeneous catalysts: An overview. *Int. J. Hydrogen Energy*, 40, 948-979.
- Julkapli, N. M., Bagheri, S. (2016). Magnesium oxide as a heterogeneous catalyst support. *Rev. Inorg. Chem.* 36, 1-8.
- Kou, J., Lu, C., Wang, J., Chen, Y., Xu, Z., Varma, R. S. (2017). Selectivity Enhancement in Heterogeneous Photocatalytic Transformations. *Chem. Rev.* 117, 1445-1514.
- Li, X., Peng, X.-H., Zheng, B.-D., Tang, J., Zhao, Y., Zheng, B.-Y., Ke, M.-R., Huang, J.-D. (2018). New application of phthalocyanine molecules: from

- photodynamic therapy to photothermal therapy by means of structural regulation rather than formation of aggregates. *Chem. Sci.* 9, 2098-2014.
- Ma, Z., Guan, B., Guo, J., Wu, X., Chen, Y., Zhang, J., Jiang, Bao, S., Chen, L., Shu, K., Dang, H., Guo, Z., Li, Z., Yao, S., Huang, Z. (2023). State of the art and perspectives of heterogeneous photocatalysts based on metal–organic frameworks (MOFs): design, modification strategies, and their applications and mechanisms in photodegradation, water splitting, and CO₂ reduction. *Catal. Sci. Technol.* 13, 4285-4347.
- Moreira, I. M., Vieira dos Santos, F., Lyon, J. P., Maftoum-Costa, M., Pacheco-Soares, C., Soares da Silva, N. (2008). Photodynamic therapy: porphyrins and phthalocyanines as photosensitizers. *Aust. J. Chem.* 61, 741.
- Nguyen, V.-N., Zhao, Z., Tang, B. Z., Yoon, J. (2022). Organic photosensitizers for antimicrobial phototherapy. *Chem. Soc. Rev.* 51, 332-33404.
- Nidheesh, P. V., Boczkaj, G., Ganiyu, S. O., Oladipo, A. A., Fedorov, K., Xiao, R., Dionysiou, D. D. (2025). Generation, properties, and applications of singlet oxygen for wastewater treatment: a review. *Environ. Chem. Lett.* 23, 195-240.
- Oh, S., Stache, E. E. (2022). Chemical Upcycling of Commercial Polystyrene via Catalyst-Controlled Photooxidation. *J. Am. Chem. Soc.* 144, 5745-5749.
- Pal, N., Bhaumik, A. (2015). Mesoporous materials: versatile supports in heterogeneous catalysis for liquid phase catalytic transformations. *Rsc Adv.* 5, 24363.
- Ravelli, D., Fagnoni, M., Albini, A. (2013). Photoorganocatalysis. what for? *Chem. Soc. Rev.* 42, 97-113.
- Schätz, A., Reiser, O., Stark, W. J. (2010). Nanoparticles as Semi-Heterogeneous Catalyst Supports. *Chem. Eur. J.* 16, 8950-8967.
- Szymczak, J., Kryjewski, M. (2022). Porphyrins and Phthalocyanines on Solid-State Mesoporous Matrices as Catalysts in Oxidation Reactions. *Materials*, 15, 2532.
- Wysocki, M., Ziental, D., Biyiklioglu, Z., Jozkowiak, M., Baş, H., Długaszewska, J., Kempisty, H. P., Güzel, E., Sobotta, L. (2025) Non-peripheral octasubstituted zinc (II) phthalocyanines bearing pyridinepropoxy substituents–Antibacterial, anticancer photodynamic and sonodynamic activity, *J. Inorg. Biochem.*, 262, 112751.
- Yu, Y., Cai, R., Lv, L., Dong, H., Xu, Y., Zhang, Q., Shen, R. (2025). Recent advances in the oxidative activation of the C2–C3 π bond of indoles and its applications. *Org. Biomol. Chem.* 23, 774-792.
- Zheng, B.-D., He, Q.-X., Li, X., Yoon, J., Huang, J.-D. (2021). Phthalocyanines as contrast agents for photothermal therapy. *Coord. Chem. Rev.* 426, 213548.

A Functional-Analytic Approach to Hyers-Ulam Stability of n -th Order Differential Equations

Emel Biçer *

Department of Mathematics/Bingol University, Turkey
*(ekayabicer@gmail.com)

ABSTRACT

In this study, we investigate the Hyers-Ulam stability of a n th-order differential equation by employing the Open Mapping Theorem. The concept of Hyers-Ulam stability provides a framework to determine whether approximate solutions of a differential equation remain close to exact solutions under small perturbations. By formulating the problem in an appropriate Banach space setting, we transform the given n -th order differential equation into an equivalent operator equation. The application of the Open Mapping Theorem ensures the boundedness and surjectivity properties of the associated linear operator, which in turn yield explicit stability bounds for the solutions. The obtained results extend and generalize existing stability theorems for first and second-order equations to the n -th order case, and provide a rigorous functional-analytic approach for further stability analysis.

Keywords – Hyer-Ulam Stability, n -th Order, Banach Space, Open Mapping, Differential Equation.

INTRODUCTION

In 1940, Ulam discussed the problem of the stability of homomorphism. If the answer is affirmative, the functional equation for homomorphisms is said to have the Hyers-Ulam stability because the first result concerning the stability of functional equations was presented by D.H. Hyers (see [D.H. Hyers [4]).

The stability problems of various functional differential equations have been investigated by many authors (see [1]-[16]). In the literature, first, Obłozza [5] initiated the study of the Hyers stability for the ordinary differential equation $x' = f(t, x)$.

Later, Obłozza [8] considered two kinds of stability, Hyers stability and Lyapunov stability, for the ordinary differential equation $x' = f(t, x)$, where $f : \mathbb{R}^2 \rightarrow \mathbb{R}$ is a continuous function, Lipschitzian with respect to the second variable. The author discussed the Hyers stability and the Lyapunov stability.

In 2010, Jung and Brzdęk [12] investigated approximate solutions of the delay differential equation $y'(t) = \delta y(t - \tau)$ with an initial condition. The authors showed that approximate solutions can be “approximated” by solutions of the equation that are constants on the interval $[-\tau, 0]$ and, therefore, have quite simple forms. Their results correspond to the notion of stability introduced by Ulam.

In 2013, Otrocol and Ilea [13] explored the Hyers-Ulam stability of delay differential equation of the form

$$x'(t) = f(t, x(t), x(g(t))).$$

Otrocol and Ilea [13] obtained two results on the Hyers-Ulam stability of the solution on a compact interval $[a, b]$ and the generalized the Hyers-Ulam-Rassias stability on an interval $[a, \infty)$.

For more detailed definitions of the Hyers-Ulam stability and the Hyers-Ulam-Rassias stability refer to [1-6].

Huang and Li (2015) discussed stability of some classes of linear functional differential equations using open mapping theorem. They showed that the Hyers-Ulam stability holds true for

$$y^{(n)} = g(t)y(t - \tau) + h(t).$$

In this paper we investigate Hyers-Ulam stability of the neutral differential equation with variable delay of the form

$$y^{(n)}(t) = \sum_{i=1}^{n-1} a_i(t)y^{(i)}(t - \tau_i(t)) + g(t) \quad (1)$$

using open mapping theorem for $t \in [m(0), T]$,
 $a_1, a_2, \dots, a_{n-1}, g \in C[m(0), T]$, where
 $m_i(0) = \inf\{t - \tau_i(t), t \geq 0\}$, $m(0) = \min\{m_i(0), 1 \leq i \leq n-1\}$.

STABILITY

In this section, we study the Hyers- Ulam stability of functional differential equation (1) on $[0, T]$.

Let $P: A \rightarrow B$ be a bounded linear operator and let $\ker P$ denote the kernel of P . Define the induced one-to-one operator \tilde{P} from the quotient space $A/\ker P$ into B by

$$\tilde{P}(u + \ker P) := Pu, \quad \forall u \in A.$$

Definition 2.1. If there is a constant K with the following properties, then the operator P has the Hyers-Ulam stability:

For any $g \in P(A)$, $\varepsilon \geq 0$ and $f \in A$ satisfying $\|Pf - g\| \leq \varepsilon$, there exists $f_0 \in A$ such that $Pf_0 = g$ and $\|f - f_0\| \leq K\varepsilon$, where K is a Hyers-Ulam stability constant of operator P .

Definition 2.2. If there is a constant K with the following properties, then the equation $Pf = g$ has the Hyers-Ulam stability:

For any $\varepsilon \geq 0$ and $f \in A$ satisfying $\|Pf - g\| \leq \varepsilon$, there exists $f_0 \in A$ such that $Pf_0 = g$ and

$\|f - f_0\| \leq K\varepsilon$, where K is a Hyers-Ulam stability constant of equation $Pf = g$.

Remark. If operator P has the Hyers-Ulam stability and $g \in P(A)$, then equation $Pf = g$ has the Hyers-Ulam stability.

Theorem 2.1. Let A and B be Banach spaces and P be a bounded linear operator from A into B . Then the following statements are equivalent:

- (i) P has the Hyers-Ulam stability
- (ii) The range of P is closed
- (iii) \tilde{P}^{-1} is a bounded linear operator.

Definition 2.3. If there exists a constant $K > 0$ with the following property, then equation (1) with $g(t) = 0$ has the Hyers-Ulam stability. That is, for every $\varepsilon > 0$, $y \in C([m(0), b], \mathfrak{R})$, if

$$\left| y^{(n)}(t) - \sum_{i=1}^{n-1} a_i(t) y^{(i)}(t - \tau_i(t)) \right| \leq \varepsilon$$

for all $t \in [0, b]$, then there exists some $y_0 \in C([m(0), b], \mathfrak{R})$ satisfies

$$y_0^{(n)}(t) = \sum_{i=1}^{n-1} a_i(t) y_0^{(i)}(t - \tau_i(t))$$

for all $t \in [0, b]$, with $|y(t) - y_0(t)| \leq K\varepsilon$ for all $t \in [m(0), b]$.

Theorem 2.2. For $a_i \in [m(0), b]$, the equation of

$$y^{(n)}(t) = \sum_{i=1}^{n-1} a_i(t) y^{(i)}(t - \tau_i(t)) \quad (2)$$

has the Hyers-Ulam stability on $[m(0), b]$.

Proof. Let $y \in C([m(0), b], \mathfrak{R})$. Define

$$\|y\| = \max_{1 \leq i \leq n-1} \left(\sup_{x \in [m(0), b]} |y^{(i)}(x)| \right).$$

Then $(C([m(0), b], \mathfrak{R}), \|\cdot\|)$ is a Banach space. Define an operator $T : (C([m(0), b], \mathfrak{R}), \|\cdot\|) \rightarrow C[0, b]$ by

$$(Tf)(t) = f^{(n)}(t) - \sum_{i=1}^{n-1} a_i(t) f^{(i)}(t - \tau_i(t))$$

for all $f(t) \in C([m(0), b], \mathfrak{R})$.

Then T is well-defined and is a linear operator. Moreover,

$$\begin{aligned} \|T\| &= \sup_{\|f\|=1} \|Tf\| \\ &= \sup_{\|f\|=1} \sup_{t \in [0, b]} \left| f^{(n)}(t) - \sum_{i=1}^{n-1} a_i(t) f^{(i)}(t - \tau_i(t)) \right| \\ &\leq \sup_{\|f\|=1} \sup_{t \in [0, b]} \left(|f^{(n)}(t)| + \left| \sum_{i=1}^{n-1} a_i(t) f^{(i)}(t - \tau_i(t)) \right| \right) \\ &\leq 1 + \sup_{t \in [0, b]} (|a_1(t)| + |a_2(t)| + \dots + |a_{n-1}(t)|) < \infty, \end{aligned}$$

for $1 \leq i \leq n-1$. Since a_i are continuous functions on $[0, b]$, T is a linear bounded operator.

Moreover, it is clear that for every $f \in C([m(0), b], \mathfrak{R})$, $Tf \in C[0, b]$, $C[0, b]$ is a Banach space and for every $y \in C[0, b]$, there are some

$f \in C([m(0), b], \mathfrak{R})$ such that $Tf = y$ (from the basic theory of functional differential equations). Thus the range of T is closed.

From Theorem 2.1 we said that operator T has the Hyers Ulam stability. Then if for all $t \in [0, b]$, $f \in C([m(0), b], \mathfrak{R})$ satisfies

$$\left| f^{(n)}(t) - \sum_{i=1}^N a_i(t) f(t - \tau_i(t)) - \sum_{i=1}^N b_i(t) f'(t - \tau_i(t)) \right| \leq \varepsilon$$

So there is a constant K , for every $\varepsilon \geq 0$. Thus there exists a solution $f_0 \in C([m(0), b], \mathfrak{R})$ of Equation (1) with

$$\sup_{t \in [m(0), b]} |f_0(t) - f(t)| \leq \|f_0 - f\| \leq K\varepsilon,$$

from the definition of the norm in $C([m(0), b], \mathfrak{R})$. This completes our proof.

Corollary. The nonhomogenous equation

$$y^{(n)}(t) = \sum_{i=1}^{n-1} a_i(t) y^{(i)}(t - \tau_i(t)) + g(t)$$

also has the Hyers-Ulam stability.

Proof. Let

$$(Hy)(t) := y^{(n)}(t) - \sum_{i=1}^{n-1} a_i(t) y^{(i)}(t - \tau_i(t)) - g(t)$$

It suffices to show that the operator $(Hy)(t)$ has the Hyers-Ulam stability.

Since $g \in C[0, b]$ and the

operator T has the Hyers-Ulam stability, we obtain that for any $a_{i_0} \in C[0, b]$ ($1 \leq i \leq n-1$), $\varepsilon \geq 0$ and $f \in C([m(0), b], \mathfrak{R})$ with

$$\|Tf - (a_{i_0} + a_{2_0} + \dots + a_{(n-1)_0}) - g\| \leq \varepsilon$$

There exists an $f_0 \in C([m(0), b], \mathfrak{R})$ such that $Tf_0 - (a_{i_0} + a_{2_0} + \dots + a_{(n-1)_0}) - g = 0$

with a Hyers-Ulam constant K . That is:

For any $a_{i_0}, b_{i_0} \in C[0, b]$ ($1 \leq i \leq N$) $\varepsilon \geq 0$ and $f \in C([m(0), b], \mathfrak{R})$ with $\|Hf - (a_{1_0} + a_{2_0} + \dots + a_{(n-1)_0})\| \leq \varepsilon$, there exists an $f_0 \in C([m(0), b], \mathfrak{R})$ such that

$$Hf_0 - (a_{1_0} + a_{2_0} + \dots + a_{(n-1)_0}) = 0$$

with a Hyers-Ulam constant K . Thus H has the Hyers-Ulam stability.

Theorem. If a function $f \in C([m(0), t_m], \mathfrak{R})$ satisfies

$$\left| f^{(n)}(t) - \sum_{i=1}^{n-1} a_i(t) f(t - \tau_i(t)) - g(t) \right| \leq \varepsilon$$

for all $t \in [m(0), t_m]$, then there exists a solution $f_0 \in C([m(0), t_m], \mathfrak{R})$ of

$$y^{(n)}(t) = \sum_{i=1}^{n-1} a_i(t) y^{(i)}(t - \tau_i(t)) + g(t)$$

with

$$|f(t) - f_0(t)| \leq K\varepsilon$$

for all $t \in [m(0), t_m]$, where K is a positive constant.

Proof. Define a function $f_0 \in C([m(0), T], \mathfrak{R})$ by

$$f_0(t) = f(t), t \in [m(0), 0]$$

$$\begin{aligned} f_0(t) = & \int_{t_k}^t [\dots \int_{t_k}^{u_3} \int_{t_k}^{u_2} (\sum_{i=1}^{n-1} (a_i(u_1) f_0(u_1 - \tau_i(u_1)) + g(u_1)) du_1 + f_0^{(n-1)}(t_k)] du_2 \dots \\ & + f_0'(t_0)] du_n + f_0(t_k), \quad t \in [t_k, t_{k+1}] \end{aligned}$$

for every $k \in \{0, 1, \dots, m-1\}$ where $f_0^{(r)}(0) = f^{(r)}(0^+)$ for all $0 \leq r \leq n-1$ and $f_0^{(r)}(t_k) = f_0^{(r)}(t_k^-)$ for all $k \geq 1, 0 \leq r \leq n-1$.

Then, f_0 is well-defined and it is a solution of Eq. 1. and

$$|f_0(t) - f(t)| = 0$$

on $[m(0), 0]$,

$$\begin{aligned}
\left| f_0^{(n)}(t) - f^{(n)}(t) \right| &\leq \left| \sum_{i=1}^{n-1} a_i(t) f_0(t - \tau_i(t)) + g(t) - \sum_{i=1}^{n-1} a_i(t) f(t - \tau_i(t)) - g(t) \right| \\
&\quad + \left| f^{(n)}(t) - \sum_{i=1}^{n-1} a_i(t) f(t - \tau_i(t)) - g(t) \right| \\
&\leq \left| \sum_{i=1}^{n-1} a_i(t) f_0(t - \tau_i(t)) - \sum_{i=1}^{n-1} a_i(t) f(t - \tau_i(t)) \right| + \varepsilon \\
&\leq \sum_{i=1}^{n-1} |f_0(t - \tau_i(t)) - f(t - \tau_i(t))| \cdot \sup_{t \in [t_{j-1}, t_j]} |a_i(t)| + \varepsilon
\end{aligned}$$

on $[t_{j-1}, t_j]$ for all $1 \leq j \leq m$ and

$$\begin{aligned}
\sup_{t \in [t_{j-1}, t_j]} \left| f_0^{(r)}(t) - f^{(r)}(t) \right| &\leq \sup_{t \in [t_{j-1}, t_j]} \left| f_0^{(r+1)}(t) - f^{(r+1)}(t) \right| (t_j - t_{j-1}) \\
&\quad + \left| f_0^{(r)}(t_{j-1}) - f^{(r)}(t_{j-1}) \right|
\end{aligned}$$

for all $0 \leq r \leq n-1$ and $1 \leq j \leq m$. We define a sequence $\{a_{r,j}\}_{\substack{0 \leq r \leq n \\ 0 \leq j \leq m}}$ by

$$\begin{aligned}
a_{r,0} &= 0, \quad \forall 0 \leq r \leq n \\
a_{n,j} &= a_{0,j-1} \cdot \sup_{t \in [t_{j-1}, t_j]} |a_i(t)| + 1, \quad \forall 1 \leq j \leq m \\
a_{r,j} &= a_{r+1,j} + a_{r,j-1}, \quad \forall 0 \leq r < n-1.
\end{aligned}$$

From this, we obtain

$$\left| f_0^{(r)}(t) - f^{(r)}(t) \right| \leq a_{r,j} \varepsilon$$

on $[t_{j-1}, t_j]$ for each $0 \leq r \leq n$ and each $1 \leq j \leq m$.

For all $0 \leq j \leq m$, since every $a_{r,j}$ is nonnegative, $a_{0,m} \geq a_{0,j}$. So,

$$\left| f_0(t) - f(t) \right| \leq a_{0,m} \varepsilon$$

for all $t \in [m(0), t_m]$.

REFERENCES

- [1] Ulam, S. M., *Problems in Modern Mathematics*. Science Editions John Wiley & Sons, Inc., New York, 1964.
- [2] Hyers, Donald H., *On the Stability of the Linear Functional Equation*. Proc. Nat. Acad. Sci. U.S.A., **27**, pp. 222–224, 1941.
- [3] Rassias, Themistocles M., *On the Stability of the Linear Mapping in Banach Spaces*. Proc. Amer. Math. Soc., **72**(2), 297–300, 1978.
- [4] Alsina, C. & Ger, R., *On some Inequalities and Stability Results Related to the Exponential Function*, J. Inequal. Appl., **4**, pp. 373–380, 1998.
- [5] Obłoza, M., *Hyers Stability of the Linear Differential Equation*. RocznikNauk.-Dydakt. Prace Mat., **13**, pp. 259–270, 1993.
- [6] Hyers, Donald H., George Isac. & Rassias, Themistocles M., *Stability of Functional Equations in Several Variables*. Progress in Nonlinear Differential Equations and their Applications, **34**, 1998.
- [7] Hyers, Donald H., & Rassias, Themistocles M., *Approximate Homomorphisms*. Aequationes Math, **44**, pp. 125–153, 1992.
- [8] Obłoza, M., *Connections between Hyers and Lyapunov Stability of the Ordinary Differential Equations*. Rocznik Nauk-Dydakt. Prace Mat. **14**, pp. 141–146, 1997.
- [9] Cădariu, L. & Radu, V., *On the stability of the Cauchy Functional Equation: A Fixed Point Approach*, Iteration theory (ECIT'02), Grazer Math. Ber., 346 pp. 43–52, 2004.
- [10] Cădariu, L. & Radu, V., *Fixed Points and the Stability of Jensen's Functional Equation*, J. Inequal. Pure Appl. Math., **4**, pp. 1–7, 2003.
- [11] Jung, S. M., *A Fixed Point Approach to the Stability of Differential Equations $y' = F(x, y)$* . Bull. Malays. Math. Sci. Soc., **33**, pp. 47–56, 2010.
- [12] Jung, S. M., & Brzdęk, J., *Hyers-Ulam Stability of the Delay Equation $y'(t) = \lambda y(t - \tau)$* . Abstr. Appl. Anal., pp. 1–10, 2010.
- [13] Otrocol, D., & Ilea, V., *Ulam Stability for a Delay Differential Equation*. Cent. Eur. J. Math., **7**, pp. 1296–1303, 2013.
- [14] Rassias, Themistocles M., *On the Stability of Functional Equations and a Problem of Ulam*. Acta Appl. Math., **1**, pp. 23–130, 2000.
- [15] Tunc, C., & Biçer, E., *Hyers-Ulam-Rassias Stability for a First order Functional Differential Equation*. J. Math. Fund. Sci. **2**, pp. 143–153, 2015.
- [16] Huang, J., & Li, Y., *Hyers-Ulam Stability of Linear Functional Differential Equation*. J. Math. Anal. Appl., pp. 1192–1200, 2015.

Harnessing Plasmonic Resonance: Metal Nanoparticles in Modern Technology

İlhan CANDAN¹
Sezai ASUBAY²

- 1- Asst. Prof. Dr.; Dicle Üniversitesi Fen Fakültesi Fizik Bölümü. ilhancndn@gmail.com ORCID No: 0000-0001-9489-5324
- 2- Prof. Dr.; Dicle Üniversitesi Fen Fakültesi Fizik Bölümü. sezai.asubay@gmail.com ORCID No: 0000-0003-2171-8479.

ABSTRACT

Plasmonic metal nanoparticles, particularly those composed of gold, silver, and other noble metals, have emerged as powerful nanomaterials capable of manipulating light at subwavelength scales. This chapter explores the fundamental principles of localized surface plasmon resonance (LSPR), a phenomenon where collective oscillations of conduction electrons in metallic nanoparticles lead to intense light absorption, scattering, and near-field enhancement. By tailoring the shape, size, composition, and dielectric environment of these nanoparticles, their optical properties can be finely tuned to meet the requirements of various technological applications. We highlight how these unique plasmonic effects are leveraged across modern disciplines, including biomedical imaging and photothermal therapy, ultrasensitive molecular sensing via surface-enhanced Raman scattering (SERS), and advanced solar energy harvesting through light trapping and hot carrier generation. The chapter also examines the role of plasmonic nanoparticles in catalysis, metasurfaces, and emerging quantum photonic systems, underscoring their versatility in bridging the gap between photonics and nanotechnology. In addition to reviewing key applications, we discuss material choices, synthesis strategies, and integration challenges associated with the deployment of plasmonic nanoparticles in real-world devices. Emerging trends—such as active plasmonics, bioplasmonics, and plasmon-enhanced environmental sensing—are also explored, revealing the dynamic evolution of this field. By presenting a comprehensive overview of both foundational concepts and state-of-the-art technologies, this chapter provides researchers, engineers, and technologists with a detailed understanding of how plasmonic resonance in metal nanoparticles is shaping the future of nanophotonics and modern optoelectronic applications.

Keywords – Plasmonics, Metal, LSPR, Gold, Silver, Nanoparticles.

INTRODUCTION

Plasmonics, the study of collective oscillations of free electrons in metallic nanostructures under electromagnetic excitation, has emerged as a transformative domain across physics, chemistry, and engineering (Halas, Lal, Chang, Link, & Nordlander, 2011; Krasavin, Ginzburg, & Zayats, 2018). Among its most exciting components are plasmonic metal nanoparticles—typically made of noble metals such as gold (Au) and silver (Ag)—which exhibit localized surface plasmon resonances (LSPRs) when illuminated by light (Khurana & Jaggi, 2021). These resonances amplify electromagnetic fields near the nanoparticle surface, enabling a wide range of phenomena and applications (Wang, Hasanzadeh Kafshgari, & Meunier, 2020).

In the realm of nanotechnology, few phenomena have sparked as much interest and innovation as plasmonic resonance (Babicheva, 2023; Roy, Sashikant, Basak, Ayaan, & Kumar, 2024). At the heart of this phenomenon lie metal nanoparticles—typically composed of noble metals like gold, silver, and aluminum—whose interaction with light gives rise to a collective oscillation of free electrons known as localized surface plasmon resonance (LSPR). This resonant behavior, observable at the nanoscale, imparts metal nanoparticles with extraordinary optical, electronic, and sensing capabilities, making them indispensable in modern technological advancements across diverse fields (Ghosh & Pal, 2007; Hartland, 2011; G. Liu, 2024b).

Plasmonics, as a discipline, emerged from the convergence of classical electromagnetism and quantum-scale phenomena (Fitzgerald, Narang, Craster, Maier, & Giannini, 2016; Savage, 2012). When light strikes a metal nanoparticle, it can excite the conduction electrons at specific frequencies, leading to strong electromagnetic field enhancement near the particle surface. This field amplification not only alters the particle's optical absorption and scattering properties but also facilitates various nonlinear and quantum effects. These properties can be precisely tuned by controlling the nanoparticle's size, shape, composition, and dielectric environment—an attribute that has made plasmonic nanoparticles central to the design of next-generation photonic and optoelectronic devices (Babicheva, 2023).

Historically, the optical properties of metal colloids have been noted since the Middle Ages, as evidenced by the vivid stained glasses of cathedrals and the Lycurgus Cup of ancient Rome (Patkar & Sharan, 2019). However, it was not until the advent of modern spectroscopy and electron microscopy that the underlying plasmonic principles were systematically explored. Today, metal nanoparticles are engineered with unprecedented precision, allowing researchers to leverage LSPR for applications in biosensing, photovoltaics, photocatalysis, optical data storage, and even cancer theranostics (Halawa, Ahmed, Abdelrazek, Nagy, & Abdelraouf, 2025; G. Liu, 2024a).

One of the most transformative applications of plasmonic nanoparticles lies in biosensing and medical diagnostics. The sensitivity of LSPR to changes in the local refractive index makes metal nanoparticles ideal for label-free detection of biomolecular interactions at extremely low concentrations. Platforms such as surface-enhanced Raman scattering (SERS) and plasmonic photothermal therapy (PPTT) exploit this capability to achieve both real-time detection and targeted treatment, particularly in cancer diagnostics and infectious disease monitoring (Huang, Zhao, Zhao, & Cheng, 2024).

In the field of energy conversion, plasmonic nanoparticles are being integrated into solar cells to improve light absorption and carrier generation. By enhancing the local electromagnetic field or facilitating hot electron

injection, these nanoparticles can surpass the Shockley–Queisser limit of traditional photovoltaic devices (Zanatta, 2022). Additionally, in photocatalysis, plasmonic nanostructures act as efficient antennas and reactive centers, initiating chemical transformations under visible light that would otherwise require ultraviolet radiation or higher energy inputs (D. Liu & Xue, 2021).

Beyond biomedical and energy sectors, plasmonic nanoparticles are finding roles in nanophotonics, metamaterials, and data encryption, where their unique spectral signatures and tunable responses are leveraged for information processing and optical switching (Butt, 2025). Emerging techniques in nano-fabrication and self-assembly continue to expand the design space for tailored plasmonic architectures, including core-shell systems, nanorods, prisms, and hybrid materials that combine metallic and dielectric components (Ganesh et al., 2024).

Despite these promising developments, challenges remain. Issues related to thermal stability, biocompatibility, and large-scale fabrication must be addressed to fully integrate plasmonic technologies into commercial platforms (Tokel, Inci, & Demirci, 2014). Furthermore, ongoing research in quantum plasmonics and machine learning–assisted design is opening new frontiers in the theoretical understanding and functional control of plasmonic phenomena (Ding, Tserkezis, Mystilidis, Vandenbosch, & Zheng, 2025).

This chapter will explore the fundamental principles of plasmonic resonance, the synthesis and characterization of metal nanoparticles, and their application landscape in modern technology. By examining both the opportunities and limitations, we aim to provide a comprehensive overview of how harnessing plasmonic effects at the nanoscale is reshaping fields as diverse as medicine, energy, and computing.

FUNDAMENTALS OF PLASMONIC RESONANCE

Localized Surface Plasmon Resonance (LSPR)

LSPR occurs when conduction electrons in a metal nanoparticle collectively oscillate in resonance with incident light. This resonance leads to strong absorption and scattering of light and results in intense localized electromagnetic fields near the nanoparticle surface (Zhao, Xue, Ji, Li, & Li, 2021).

Key parameters influencing LSPR include (Lv, Du, Wu, Cai, & Zhou, 2022; Yockell-Lelièvre, Lussier, & Masson, 2015):

- Material properties (permittivity of the metal)
- Particle size and shape

- Surrounding dielectric environment
- Wavelength of incident light

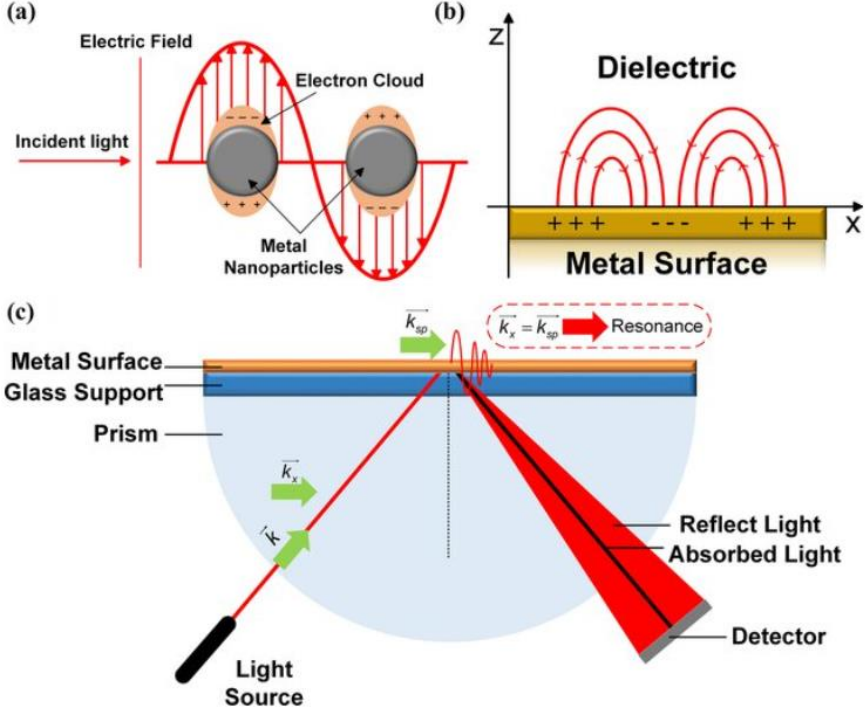


Figure 1. LSPR and SPR schematic diagrams. a) LSPR mechanism in which incident light forces the electrons on the surface of metal nanoparticles to oscillate. b) SPR process where the incident light induces the electrons on the metal and dielectric surface to collectively oscillate. c) The SPR effect on the principle of sensors (Chao et al., 2024).

The resonant condition for spherical particles in the quasistatic approximation is given by:

$$\epsilon_m(\omega) = -2 \epsilon_d \quad (1)$$

Where ϵ_m is the dielectric function of the metal, and ϵ_d is the dielectric constant of the surrounding medium.

Optical Properties of Metal Nanoparticles

Plasmonic nanoparticles exhibit:

- Strong optical absorption and scattering
- Size- and shape-dependent resonance tunability
- Near-field enhancement
- Surface-enhanced optical effects (e.g., Raman, fluorescence)

These properties underpin a variety of advanced technologies.

MATERIAL CHOICES AND NANOPARTICLE DESIGN

Common Plasmonic Metals

Gold (Au): Chemically stable, biocompatible, and exhibits strong LSPR in the visible to NIR range. Silver (Ag): Highest quality factor for LSPR but prone to oxidation. Aluminum (Al): Suitable for UV plasmonics, more earth-abundant. Copper (Cu): Cost-effective alternative, though less stable than Au or Ag (Cui et al., 2023; Shanivarasanthe Nithyananda Kumar, Martulli, Lizin, & Deferme, 2025).

Shape and Dimensional Control

LSPR can be tuned via nanoparticle shape:

- Spheres: Single resonance peak, predictable Mie theory behavior.
- Nanorods: Exhibit both transverse and longitudinal modes.
- Nanoshells and nanostars: Offer multiband resonances and enhanced field localization.

Advanced fabrication techniques such as seed-mediated growth, lithography, and template-based synthesis allow precise control over nanoparticle geometry.

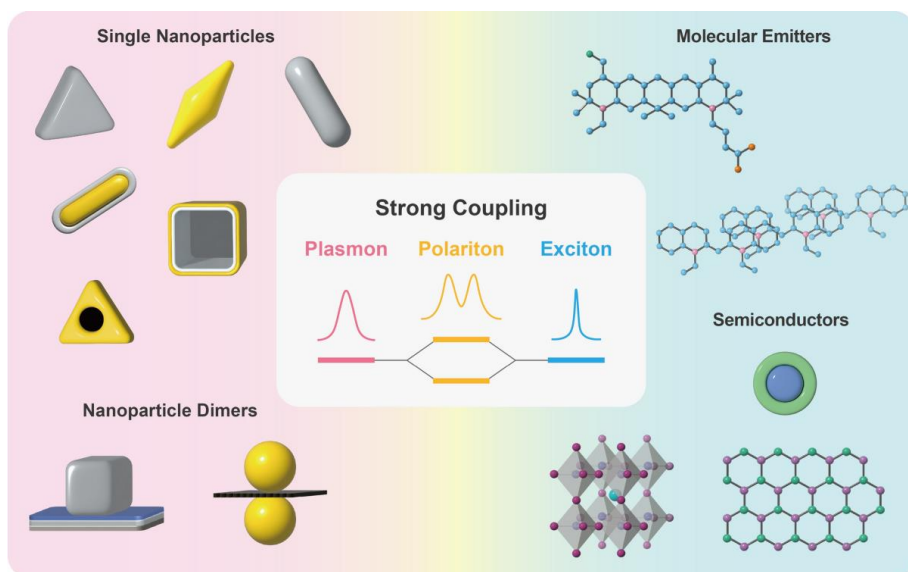


Figure 2. Polaritons formation from strong coupling between excitons and plasmons (Lee, Kim, & Park, 2023).

PLASMONIC NANOPARTICLES IN MODERN TECHNOLOGIES

Biomedical Imaging and Therapy

Bioimaging

Gold nanoparticles serve as contrast agents in various imaging modalities (Fu, Lin, Karimi-Maleh, Chen, & Zhao, 2023; Shi, Wang, Li, Feng, & Cao, 2025; Wu et al., 2025):

- Dark-field microscopy: Leveraging strong scattering from LSPR.
- Photoacoustic imaging: Nanoparticles absorb light and generate ultrasound signals.
- Multiphoton and fluorescence imaging: Enhanced by field amplification near plasmonic surfaces.

Photothermal Therapy

Plasmonic nanoparticles convert absorbed light into heat, enabling localized hyperthermia to destroy cancer cells. NIR-absorbing nanorods or

nanoshells are often used for deep tissue penetration (Debnath et al., 2024; Tabish et al., 2020).

Sensing and Detection

Surface-Enhanced Raman Scattering (SERS)

Plasmonic nanoparticles dramatically enhance Raman signals of nearby molecules due to:

- Electromagnetic field amplification
- Charge transfer between molecule and metal

SERS enables single-molecule detection, making it a powerful tool for chemical and biological sensing.

LSPR Sensing

Changes in the dielectric environment near a nanoparticle shift its resonance peak. This principle underpins label-free biosensors used to detect:

- Proteins
- DNA/RNA
- Pathogens and viruses

Plasmonic biosensors offer real-time, highly sensitive detection and are integrated into portable diagnostics and lab-on-a-chip platforms.

Plasmonic Photovoltaics

Light Trapping in Solar Cells

Embedding plasmonic nanoparticles into solar cells enhances light absorption through:

- Scattering: Increasing optical path length.
- Near-field enhancement: Boosting local absorption.
- Hot-electron injection: Contributing additional carriers.

These effects are particularly useful for thin-film photovoltaics and semiconductors with poor absorption in the visible range (e.g., TiO₂, Si).

Hot Carrier Solar Cells

In plasmonic hot carrier devices, energetic electrons generated from plasmon decay are extracted before thermalization. These systems aim to surpass the Shockley–Queisser limit, although significant challenges in carrier extraction remain.

Plasmon-Enhanced Photocatalysis

Plasmonic nanoparticles serve as visible-light photocatalysts or co-catalysts, promoting chemical reactions such as:

- Water splitting
- CO₂ reduction
- Organic synthesis

Mechanisms include:

- Photothermal heating
- Hot carrier transfer to reactants
- Field-enhanced excitation of catalytic sites

Hybrid structures (e.g., Au-TiO₂) are often used to combine plasmonic and catalytic functionalities.

EMERGING APPLICATIONS AND FRONTIERS

Plasmonic Metamaterials and Metasurfaces

By arranging plasmonic nanoparticles into periodic or quasi-periodic arrays, designers create:

- Metasurfaces with tailored reflection, refraction, or absorption.
- Optical cloaks, flat lenses, and holographic devices.
- Chiral nanostructures for polarization control and enantioselective sensing.

Quantum Plasmonics

At nanometer and sub-nanometer scales, classical descriptions of plasmonics break down. Quantum plasmonics explores:

- Nonlocal effects
- Quantum tunneling in nanogaps
- Strong coupling with excitons or quantum dots

These effects are critical for ultrasensitive detectors and quantum information processing.

Plasmonic Nanosensors for Environmental Monitoring

Plasmonic nanoparticles are used for detecting:

- Heavy metal ions
- Air and water pollutants
- Hazardous gases (e.g., H₂S, NO₂)

Portable plasmonic sensors allow in-situ and real-time monitoring, critical for environmental protection and public health.

DESIGN CONSIDERATIONS AND CHALLENGES

Despite their promise, plasmonic technologies face several design and implementation challenges:

- Material limitations: Oxidation, aggregation, and instability of metals like Ag and Cu.
- Thermal effects: Heat generated during operation can alter performance or damage substrates.
- Cost and scalability: Fabricating uniform, reproducible nanoparticles at large scale remains a hurdle.
- Integration: Incorporating plasmonic elements into commercial systems without compromising performance or compatibility.

Strategies to address these challenges include:

- Coating with protective layers (e.g., silica, polymers)
- Alloying or doping to tailor properties
- Using alternative materials (e.g., doped semiconductors, conducting oxides)

FUTURE DIRECTIONS

The field of plasmonics continues to evolve, with exciting frontiers such as:

- Active plasmonics: Dynamic tuning using phase-change materials, electric fields, or optical pumping.
- Bioplasmonics: Real-time tracking of cellular processes, gene expression, and protein dynamics.
- Plasmonic neural interfaces: Leveraging optoelectronic stimulation for brain–machine interfacing.
- Integrated plasmonic–photonic systems: Combining plasmonic nanoantennas with silicon photonics for on-chip applications.

Furthermore, advances in machine learning and computational design are enabling the inverse design of plasmonic structures for targeted functionality.

CONCLUSION

The exploitation of plasmonic resonance in metal nanoparticles—particularly gold and silver—has revolutionized modern nanotechnology by enabling unparalleled control over light–matter interactions at the nanoscale. In this chapter, we have explored the fundamental principles of localized surface plasmon resonance (LSPR), the synthesis and tunability of plasmonic nanoparticles, and their diverse applications across sensing, photonics, biomedicine, and energy technologies.

Plasmonic nanoparticles exhibit unique optical properties that are highly sensitive to size, shape, composition, and the surrounding dielectric environment. These features enable the engineering of responsive systems where light can be manipulated with extraordinary precision. Advances in fabrication techniques, such as pulsed laser deposition (PLD), colloidal synthesis, and electron beam lithography, have allowed for scalable and reproducible production of nanostructures with tailored plasmonic responses.

In practical applications, plasmonic nanoparticles have demonstrated exceptional performance in surface-enhanced spectroscopies (like SERS), biosensors with single-molecule sensitivity, photothermal cancer therapy, and light-harvesting in photovoltaic devices. Their ability to localize and amplify electromagnetic fields has opened new frontiers in nano-optics and metamaterials, making them central to next-generation photonic circuits and lab-on-chip technologies.

Despite these advances, challenges remain in achieving precise control over nanoparticle placement, stability under high-power illumination, and integration with semiconductor platforms. Future research will likely focus on hybrid plasmonic–photonic systems, dynamic tunability using stimuli-responsive materials, and exploration of non-metallic plasmonic alternatives.

In summary, the control and application of plasmonic resonance in metal nanoparticles continue to unlock innovative solutions across scientific disciplines. As fabrication, simulation, and characterization techniques advance, plasmonics will play an increasingly vital role in shaping the future of optical and nanotechnological innovation.

REFERENCES

- Babicheva, V. E. (2023). Optical processes behind plasmonic applications. *Nanomaterials*, 13(7), 1270.
- Butt, M. A. (2025). A perspective on plasmonic metasurfaces: unlocking new horizons for sensing applications. *Nanotechnology*, 36(18), 182501.
- Chao, J., Wang, G., Qiu, P., Sun, H., Wang, Y., Duan, X., . . . Fu, B. (2024). Optical properties and applications of metal nanomaterials in ultrafast photonics: a review. *Journal of Materials Science*, 59(29), 13433-13461.
- Cui, X., Ruan, Q., Zhuo, X., Xia, X., Hu, J., Fu, R., . . . Xu, H. (2023). Photothermal nanomaterials: a powerful light-to-heat converter. *Chemical Reviews*, 123(11), 6891-6952.
- Debnath, M., Debnath, S. K., Talpade, M. V., Bhatt, S., Gupta, P. P., & Srivastava, R. (2024). Surface engineered nanohybrids in plasmonic photothermal therapy for cancer: Regulatory and translational challenges. *Nanotheranostics*, 8(2), 202.

- Ding, T., Tserkezis, C., Mystilidis, C., Vandenbosch, G. A., & Zheng, X. (2025). Quantum mechanics in plasmonic nanocavities: from theory to applications. *Advanced Physics Research*, 4(4), 2400144.
- Fitzgerald, J. M., Narang, P., Craster, R. V., Maier, S. A., & Giannini, V. (2016). Quantum plasmonics. *Proceedings of the IEEE*, 104(12), 2307-2322.
- Fu, L., Lin, C.-T., Karimi-Maleh, H., Chen, F., & Zhao, S. (2023). Plasmonic nanoparticle-enhanced optical techniques for cancer biomarker sensing. *Biosensors*, 13(11), 977.
- Ganesh, K. M., Bhaskar, S., Cheerla, V. S. K., Battampara, P., Reddy, R., Neelakantan, S. C., . . . Ramamurthy, S. S. (2024). Review of gold nanoparticles in surface plasmon-coupled emission technology: Effect of shape, hollow nanostructures, nano-assembly, metal-dielectric and heterometallic nanohybrids. *Nanomaterials*, 14(1), 111.
- Ghosh, S. K., & Pal, T. (2007). Interparticle coupling effect on the surface plasmon resonance of gold nanoparticles: from theory to applications. *Chemical reviews*, 107(11), 4797-4862.
- Halas, N. J., Lal, S., Chang, W.-S., Link, S., & Nordlander, P. (2011). Plasmons in strongly coupled metallic nanostructures. *Chemical reviews*, 111(6), 3913-3961.
- Halawa, O. M., Ahmed, E., Abdelrazek, M. M., Nagy, Y. M., & Abdelraouf, O. A. (2025). Illuminating the Future: Nanophotonics for Future Green Technologies, Precision Healthcare, and Optical Computing. *arXiv preprint arXiv:2507.06587*.
- Hartland, G. V. (2011). Optical studies of dynamics in noble metal nanostructures. *Chemical reviews*, 111(6), 3858-3887.
- Huang, Y., Zhao, C., Zhao, L., & Cheng, Z. (2024). SERS for Precision Medicine: A Promising Approach. In *Surface-and Tip-Enhanced Raman Scattering Spectroscopy: Bridging Theory and Applications* (pp. 337-370): Springer.
- Khurana, K., & Jaggi, N. (2021). Localized surface plasmonic properties of Au and Ag nanoparticles for sensors: A review. *Plasmonics*, 16(4), 981-999.
- Krasavin, A. V., Ginzburg, P., & Zayats, A. V. (2018). Free-electron optical nonlinearities in plasmonic nanostructures: a review of the hydrodynamic description. *Laser & Photonics Reviews*, 12(1), 1700082.
- Lee, Y.-M., Kim, S.-E., & Park, J.-E. (2023). Strong coupling in plasmonic metal nanoparticles. *Nano Convergence*, 10(1), 34.
- Liu, D., & Xue, C. (2021). Plasmonic coupling architectures for enhanced photocatalysis. *Advanced Materials*, 33(46), 2005738.
- Liu, G. (2024a). Engineering Applications. In *Thermoplasmonics: From Principles, Materials and Characterization to Engineering Applications* (pp. 107-177): Springer.
- Liu, G. (2024b). *Thermoplasmonics*: Springer.
- Lv, S., Du, Y., Wu, F., Cai, Y., & Zhou, T. (2022). Review on LSPR assisted photocatalysis: effects of physical fields and opportunities in multifield decoupling. *Nanoscale Advances*, 4(12), 2608-2631.
- Patkar, N., & Sharan, M. (2019). Did Nanotechnology Flourish During the Roman Empire and Medieval Periods? *History of Nanotechnology: From Pre-Historic to Modern Times*, 113-140.
- Roy, A., Sashikant, M. S., Basak, A., Ayaan, M., & Kumar, A. (2024). Illuminating the Future of Medicine: Surface Plasmon Resonance-Based

- Nanotechnologies for Genetic Disorder Management. *International Journal of Scientific Research and Technology*.
- Savage, K. J. (2012). *Plasmonic interactions in the quantum tunnelling regime*.
- SHANIVARASANTHE NITHYANANDA KUMAR, R., Martulli, A., Lizin, S., & Deferme, W. (2025). The research path to commercialization: A perspective on plasmonic nanoparticles in organic and perovskite optoelectronics.
- Shi, Y., Wang, L., Li, L., Feng, C., & Cao, Y. (2025). Innovative Progress of LSPR-Based Dark-Field Scattering Spectral Imaging in the Biomedical Assay at the Single-Particle Level. *ChemistryOpen*, 14(3), e202400017.
- Tabish, T. A., Dey, P., Mosca, S., Salimi, M., Palombo, F., Matousek, P., & Stone, N. (2020). Smart gold nanostructures for light mediated cancer theranostics: combining optical diagnostics with photothermal therapy. *Advanced Science*, 7(15), 1903441.
- Tokel, O., Inci, F., & Demirci, U. (2014). Advances in plasmonic technologies for point of care applications. *Chemical reviews*, 114(11), 5728-5752.
- Wang, L., Hasanzadeh Kafshgari, M., & Meunier, M. (2020). Optical properties and applications of plasmonic-metal nanoparticles. *Advanced Functional Materials*, 30(51), 2005400.
- Wu, J., Ko, S., Lee, E., Son, E., Kang, G., Hur, S., . . . Kim, Y. (2025). Gold nanoparticles in imaging: advances, applications, and future perspectives. *Applied Spectroscopy Reviews*, 1-40.
- Yockell-Lelièvre, H., Lussier, F., & Masson, J.-F. (2015). Influence of the particle shape and density of self-assembled gold nanoparticle sensors on LSPR and SERS. *The Journal of Physical Chemistry C*, 119(51), 28577-28585.
- Zanatta, A. R. (2022). The Shockley–Queisser limit and the conversion efficiency of silicon-based solar cells. *Results in optics*, 9, 100320.
- Zhao, J., Xue, S., Ji, R., Li, B., & Li, J. (2021). Localized surface plasmon resonance for enhanced electrocatalysis. *Chemical Society Reviews*, 50(21), 12070-12097.

Stability of Impulsive Systems with Generalized Piecewise Constant Argument: A Lyapunov-Based Approach

Duygu ARUĞASLAN ÇİNÇİN

Prof. Dr.; Süleyman Demirel Üniversitesi, Mühendislik ve Doğa Bilimleri Fakültesi, Matematik Bölümü,
Türkiye duygugarugasan@sdu.edu.tr ORCID No: 0000-0003-1867-0996.

ABSTRACT

We investigate the stability properties of impulsive differential equations with piecewise constant argument of generalized type, where abrupt changes in the state of the system are accompanied by memory effects due to the presence of delayed and discretely sampled information. These systems arise naturally in various scientific and engineering applications, including control systems, population dynamics, neural networks, and other hybrid systems where the state evolves continuously but is subjected to instantaneous changes at specific discrete moments. The combination of continuous state evolution, discrete impulses, and memory effects creates significant challenges for mathematical analysis. To overcome these challenges, our approach involves associating the original system with an auxiliary impulsive system that does not involve piecewisely defined arguments. This correspondence allows us to explore the stability behavior of the original, more complex system through a simplified and more analytically tractable framework. By establishing this connection, we are able to transfer the stability properties from the auxiliary system to the original one effectively.

The main methodological tool of this study is the Lyapunov's direct method, through which we derive conditions which are sufficient for the stability of the trivial solution. This approach avoids the use of specific functionals tailored to the delay or memory structure, thereby simplifying the analysis and improving computational efficiency.

Keywords – Impulsive Differential Equations, Lyapunov Functions, Piecewise Constant Argument Of Generalized Type, Stability, Hybrid Dynamical Systems, Lyapunov's Direct Method.

INTRODUCTION

Differential equations serve as a cornerstone in representing dynamic systems within the realms of natural sciences, engineering, and social sciences (Miller and Michel, 1982). They provide very powerful tools for describing and interpreting how quantities evolve over time in response to internal mechanisms and external influences. The dynamics of many real-world systems cannot be fully described by classical ordinary differential equations, due to the presence of features such as abrupt transitions, discontinuities, memory effects, and time delays (Cengiz and Aruğaslan Çinçin, 2022; 402; Gyori and Ladas, 1991; Samoilenko and Perestyuk, 1995). The complexities of such systems have led to the development of various forms of differential equations, including differential equations with impulse effects and those with piecewise constant arguments. Impulsive differential equations are particularly useful for modeling processes subject to sudden changes, such as

shocks in mechanical systems, medical treatments in biological models, or policy changes in economic systems. On the other hand, differential equations incorporating piecewise constant arguments enable to represent systems, where state variables depend discretely on the sampled past values, as commonly encountered in control systems, and neural networks (Chiu, 2013:1; Chiu, 2022:137). The integration of these features leads to hybrid systems that reflect real-life phenomena better, but also introduce significant analytical challenges, especially in the examination of stability and long-term behaviour of those systems.

Impulsive differential equations with generalized-type piecewise constant arguments acting as delayed terms provide a robust framework for modeling systems characterized by a mixture of continuous evolution, sudden changes, and the effects of discretely sampled past states. These hybrid behaviours are prevalent in a wide range of real-world applications, including control theory, neural networks, population dynamics, epidemiology, and economics (Karakoç, 2020:957; Chiu, 2022:137). This hybrid structure considerably enriches the dynamical features of the system and raises difficulties in the stability analysis.

In recent decades, stability properties of impulsive and delay differential systems including those with piecewise constant arguments have attracted considerable attention (Bereketoğlu et al., 2010:175; Büyükkahraman, 2022:54; Chiu, 2013:1; Karakoç, 2020:957; Zhang, 2017:1). While the literature includes numerous studies on the qualitative properties of impulsive differential equations including piecewise constant arguments, relatively few have addressed generalized form of the argument function (Akhmet and Yılmaz, 2012:18; Chiu, 2022:137; Xi, 2018:1). The question of how existing techniques can be extended to impulsive systems with generalized-type piecewise constant argument remains relatively unexplored. This study contributes to the literature by proposing new Lyapunov-based stability criteria for impulsive differential systems with generalized arguments, which do not require the construction of functionals (Rouche et al., 1977; Xi, 2018:1). The findings not only enhance the theoretical understanding of such systems but are also expected to offer practical criteria for verifying their stability in applications.

We refer to \mathbb{N} , \mathbb{R} and \mathbb{R}^n as the sets containing, respectively, all non-negative integers, all real numbers and all vectors of n -dimension with real components. Besides, we use $\|\cdot\|$ to denote the Euclidean norm in \mathbb{R}^n .

The present study focuses on the following differential equation with impulse and generalized type piecewise constant argument

$$\begin{aligned} x'(t) &= f\left(t, x(t), x(\eta(t))\right), t \neq \sigma_k \\ \Delta x|_{t=\sigma_k} &= F_k(x), \quad k = 1, 2, \dots, \end{aligned} \tag{1.1}$$

where $x \in N_\gamma = \{x: x \in \mathbb{R}^n \text{ and } \|x\| < \gamma\}$, $\sigma_k: \mathbb{N} \rightarrow \mathbb{R}^n$ denotes a sequence that is strictly increasing and tends to infinity as $k \rightarrow \infty$, and $t \in I = [\sigma_0, \infty)$. The piecewise constant argument is defined by the function η as follows: $\eta(t) = \sigma_k$ for the values of t that lie in the half open interval $[\sigma_k, \sigma_{k+1})$, $k = 0, 1, 2, \dots$. We presume that the sequence σ_k satisfies the inequality $\sigma_{k+1} - \sigma_k < \sigma$ for a positive constant σ and for every $k \in \mathbb{N}$.

We can rewrite (1.1) as follows:

$$\begin{aligned} x'(t) &= f(t, x(t), x(t)) + \varphi(t, x(t), x(\eta(t))), t \neq \sigma_k \\ \Delta x|_{t=\sigma_k} &= F_k(x), \quad k = 1, 2, \dots, \end{aligned} \quad (1.2)$$

where

$$\varphi(t, x(t), x(\eta(t))) = f(t, x(t), x(\eta(t))) - f(t, x(t), x(t)).$$

To simplify the discussion, we define $g(t, x(t)) := f(t, x(t), x(t))$ in the sequel. With this representation, it can be considered that system (1.1), or equivalently (1.2), is obtained by applying a small perturbation to the right hand side of the system

$$\begin{aligned} u'(t) &= g(t, u(t)), t \neq \sigma_k \\ \Delta u|_{t=\sigma_k} &= F_k(u), \quad k = 1, 2, \dots, \end{aligned} \quad (1.3)$$

provided that σ is small enough.

The rest of the study is given rganized as follows: Section 2 presents the preliminaries including notations, assumptions, basic definitions and useful results. Section 3 is devoted to the main results concerning the stability. Section 4 provides a discussion of the findings and outlines the main conclusions drawn from the present study.

PRELIMINARIES

This study is conducted under the framework of the following assumptions:

(a.1) $f: I \times N_\gamma \times N_\gamma \rightarrow \mathbb{R}^n$, $F_k: N_\gamma \rightarrow N_\gamma$ are continuous functions.

(a.2) For every $t \in I$, $v_1, v_2, w_1, w_2 \in N_\gamma$, the function f satisfies the Lipschitz property

$$\|f(t, v_1, w_1) - f(t, v_2, w_2)\| \leq \iota \{\|v_1 - v_2\| + \|w_1 - w_2\|\},$$

where $\iota > 0$ denotes the Lipschitz constant.

(a.3) $f(t, 0, 0) = 0$ for any $t \in I$, and else, $F_k(0) = 0$ for each $k = 1, 2, \dots$.

(a.4) If $F_k(x) = F_k(\bar{x})$, for all $k = 1, 2, \dots$, then $x = \bar{x}$.

(a.5) $\beta \exp(\beta) < \frac{1}{3}$, where $\beta = \iota \sigma$.

Condition (a3) ensures that system (1.1) admits $x = 0$ as a solution. In this study, we will focus on the stability and asymptotic stability behaviour of the equilibrium solution $x = 0$ of the system (1.1). It should be noted that definitions given for stability of the differential equations with impulsive terms and piecewise constant delays are identical to those given for classical ordinary differential equations as stated below.

Definition 2.1. The trivial solution $x = 0$ of the system (1.1) is called *stable* if for every $\varepsilon > 0$ and any initial time $t_0 \in I = [\sigma_0, \infty)$, there is a $\delta = \delta(t_0, \varepsilon) > 0$ so that the inequality $\|x(t, t_0, x_0)\| < \varepsilon$ holds for each $t \geq t_0$ whenever $\|x_0\| < \delta(t_0, \varepsilon)$.

Definition 2.2. The trivial solution $x = 0$ of the system (1.1) is said to be *asymptotically stable* if it is stable, and for any initial time $t_0 \in I = [\sigma_0, \infty)$, one can find an $\eta(t_0) > 0$ so that the solution $x(t, t_0, x_0)$ goes to zero as $t \rightarrow \infty$ provided that the initial value satisfies $\|x_0\| < \eta(t_0)$.

Lemma 2.1. If (a.1)-(a.5) are assumed to hold, then the inequality given by

$$\|x(\eta(t))\| \leq \mathcal{B}\|x(t)\|$$

stands valid for all $t \in [\sigma_0, \infty)$, and for any solution $x(t)$ of (1.1), where

$$\mathcal{B} = \frac{1}{1 - \beta - \beta \exp(\beta) - \beta^2 \exp(\beta)}.$$

PROOF. If the variable $t \in I = [\sigma_0, \infty)$ is fixed, then we can determine a $k \in \{1, 2, \dots\}$ for which $t \in [\sigma_k, \sigma_{k+1})$. Note that

$$\begin{aligned} x(t) &= x(\sigma_k) + \int_{\sigma_k}^t f(\xi, x(\xi), x(\eta(\xi))) d\xi \\ &= x(\sigma_k) + \int_{\sigma_k}^t f(\xi, x(\xi), x(\sigma_k)) d\xi \\ &= x(\sigma_k) + \int_{\sigma_k}^t (f(\xi, x(\xi), x(\sigma_k)) - f(\xi, 0, 0)) d\xi, \end{aligned}$$

for $t \in [\sigma_k, \sigma_{k+1})$. Hence, we have

$$\begin{aligned}
\|x(t)\| &\leq \|x(\sigma_k)\| + \mathfrak{L} \int_{\sigma_k}^t (\|x(\xi)\| + \|x(\sigma_k)\|) \\
&\leq (1 + \beta) \|x(\sigma_k)\| + \mathfrak{L} \int_{\sigma_k}^t \|x(\xi)\| d\xi.
\end{aligned}$$

Making use of the Gronwall-Bellman inequality, it becomes evident that the following bound

$$\|x(t)\| \leq (1 + \beta) \exp(\beta) \|x(\sigma_k)\|$$

is valid on the interval $[\sigma_k, \sigma_{k+1})$.

In a similar vein, when the same reasoning is applied, we can obtain a bound for $\|x(\sigma_k)\|$ as follows. Since

$$\begin{aligned}
x(\sigma_k) &= x(t) - \int_{\sigma_k}^t f(\xi, x(\xi), x(\eta(\xi))) d\xi \\
&= x(t) - \int_{\sigma_k}^t f(\xi, x(\xi), x(\sigma_k)) d\xi,
\end{aligned}$$

on $[\sigma_k, \sigma_{k+1})$, we find that

$$\begin{aligned}
\|x(\sigma_k)\| &\leq \|x(t)\| + \mathfrak{L} \int_{\sigma_k}^t (\|x(\xi)\| + \|x(\sigma_k)\|) d\xi \\
&\leq \|x(t)\| + \mathfrak{L} \int_{\sigma_k}^t ((1 + \beta) \exp(\beta) \|x(\sigma_k)\| + \|x(\sigma_k)\|) d\xi.
\end{aligned}$$

From this, we deduce that

$$\|x(\sigma_k)\| \leq \|x(t)\| + \beta(1 + \exp(\beta) + \beta \exp(\beta)) \|x(\sigma_k)\|,$$

and subsequently, this inequality allows us to establish that

$$\|x(\sigma_k)\| \leq \frac{1}{1 - \beta - \beta \exp(\beta) - \beta^2 \exp(\beta)} \|x(t)\| = \mathbb{B} \|x(t)\|.$$

We note that $\mathbb{B} > 0$ according to the assumption (a.5). Thus, the argument is concluded on the half open interval $[\sigma_k, \sigma_{k+1})$. This outcome confirms that the inequality (2.1) continues to hold for all $t \geq \sigma_0$. \square

Let us define a set \mathcal{P}_{rc} of all functions $\psi: I \rightarrow \mathbb{R}^n$ that are right-continuous and may have first kind discontinuities at values σ_k , where $k \in \mathbb{N}$, and also introduce \mathcal{P}_{rc}^1 as the set of functions $\psi: I \rightarrow \mathbb{R}^n$ such that both ψ

and ψ' are in \mathcal{P}_{rc} , where the derivatives at the points σ_k are considered as the right-hand derivative.

Definition 2.3. The function $x(t)$ is called to be a solution of system (1.1) on the interval $[\sigma_0, \infty)$, provided that the following conditions are met:

- (i) $x(t)$ lies in the set \mathcal{P}_{rc}^1 ;
- (ii) $x(t)$ satisfies both the differential and impulsive parts of system (1.1) on the interval $[\sigma_0, \infty)$.

Theorem 2.1. (Xi, 2018:1) Under the assumptions (a.1), (a.2), (a.4) and (a.5), for each $t_0 \in I$ and $x_0 \in N_\gamma$, the initial value problem consisting of (1.1) together with the initial data $x(t_0) = x_0$ has a unique solution on I .

MAIN RESULTS

This section presents the core theoretical results concerning the stability properties for the considered class of differential equations including impulses and also generalized type piecewise constant arguments. By leveraging the association between the original system and its auxiliary counterpart, we first investigate the stability of the trivial solution and then explore its asymptotic behaviour.

Let $V(t, u)$ stand for a real-valued, continuously differentiable function defined in the region $I \times N_\gamma$, with the property that $V(t, 0) = 0$ for each $t \in I$. Moreover, except at the points $t = \sigma_k$, the rate of change of the function V evaluated with respect to time variable t along the solution paths of (1.3) is defined by

$$V'_{(1.3)}(t, u) = \frac{\partial V(t, u)}{\partial t} + \frac{\partial V(t, u)}{\partial u} g(t, u).$$

Theorem 3.1. Let the hypotheses listed as (a.1)-(a.5) be fulfilled. Provided that a positive definite, continuously differentiable function $V(t, u)$ exists satisfying $V(t, 0) = 0$ for every $t \in I$, and the following properties for a constant $\omega > 0$:

- (i) $V'_{(1.3)}(t, u) \leq -\omega \mathbf{1}(1 + \mathcal{B})\|u\|,$
- (ii) $V(\sigma_k, u + F_k(u)) \leq V(\sigma_k, u),$

$$(iii) \quad \left\| \frac{\partial V(t, u)}{\partial u} \right\| \leq \omega,$$

for all $(t, u) \in I \times N_\gamma$, the zero solution $x = 0$ of the system (1.1) is stable.

PROOF. Let $0 < \gamma_0 < \gamma$. We fix $\varepsilon > 0$ and $t_0 \in I$. We may assume without affecting the generality of the argument that $\varepsilon < \gamma_0$. Then for $t \neq \sigma_k$, we get

$$\begin{aligned} V'_{(1.1)}(t, x(t), x(\eta(t))) &= \frac{\partial V(t, x(t))}{\partial t} + \frac{\partial V(t, x(t))}{\partial x} f(t, x(t), x(\eta(t))) \\ &= \frac{\partial V(t, x(t))}{\partial t} + \frac{\partial V(t, x(t))}{\partial x} f(t, x(t), x(t)) + \\ &\quad \frac{\partial V(t, x(t))}{\partial x} \varphi(t, x(t), x(\eta(t))) \\ &= V'_{(1.3)}(t, x(t)) + \frac{\partial V(t, x(t))}{\partial x} \varphi(t, x(t), x(\eta(t))) \\ &\leq -\omega_L(1 + B)\|x(t)\| + \omega_L \|x(t) - x(\eta(t))\| \\ &\leq -\omega_L(1 + B)\|x(t)\| + \omega_L \|x(t)\| + \\ &\quad \omega_L \|x(\eta(t))\| \\ &\leq -\omega_L(1 + B)\|x(t)\| + \omega_L \|x(t)\| + \\ &\quad \omega_L B \|x(t)\| \\ &= 0. \end{aligned}$$

Hence $V'_{(1.1)}$ is negative semidefinite. We denote the infimum of the function $V(t, x)$ for $t \in I$, $\varepsilon \leq \|x\| \leq \gamma_0$ by V_* ; and pick an arbitrarily small δ so that the supremum of the function $V(t_0, x)$ for $\|x\| < \delta$ is less than V_* . Let $x(t) = x(t, t_0, x_0)$ be a solution of (1.1) with $\|x_0\| < \delta$. Assume that $\|x(t^*)\| = \varepsilon$ for some $t^* \geq t_0$. This implies that $V(t^*, x(t^*)) \geq V_*$.

Note that although the solution trajectories of systems (1.1) and (1.3) differ due to the presence of piecewise constant delay in (1.1), condition (ii) concerning the impulse map remains valid for (1.1) as well since the inequality in (ii) is evaluated pointwise, and does not depend on the trajectory. Hence, negative semidefiniteness of $V'_{(1.1)}$ and condition (ii) lead to the conclusion that $V(t, x)$ is nonincreasing along every trajectory of system (1.1). This means that

$$V_* \leq V(t^*, x(t^*)) \leq V(t_0, x(t_0)) < V_*,$$

which is a contradiction. Hence, $\|x(t)\| < \varepsilon$ for all $t \geq t_0$. In view of Definition 2.1, this proves the stability of the zero solution of (1.1). \square

Theorem 3.2. Let (a.1)-(a.5) hold true. If there exists a positive definite, continuously differentiable function $V(t, u)$ satisfying $V(t, 0) = 0$ for each $t \in I$, and the following properties for a constant $\omega > 0$:

- (i) $V'_{(1.3)}(t, u) \leq -\omega \mathbf{L}(1 + \mathbf{B})\|u\|,$
- (ii) $V(\sigma_k, u + F_k(u)) - V(\sigma_k, u) \leq -\psi(V(\sigma_k, u)),$ where $\psi(a)$ is continuous for $a \geq 0$, with $\psi(0) = 0$, and positive for all $a > 0$,
- (iii) $\left\| \frac{\partial V(t, u)}{\partial u} \right\| \leq \omega,$

for all $(t, u) \in I \times N_\gamma$, the zero solution $x = 0$ of the system (1.1) is asymptotically stable.

PROOF. It is clear that the zero solution $x = 0$ of the system (1.1) is stable. According to Definition 2.2, it is enough to verify that $\lim_{t \rightarrow \infty} x(t, t_0, x_0) = 0$. To achieve this result, we first consider the behavior of the Lyapunov function $V(t, x(t))$ for sufficiently large values of t , i.e., $\lim_{t \rightarrow \infty} V(t, x(t))$ if it exists. The inequalities given by (i) and (ii) imply that the function $V(t, x(t))$ is nonincreasing. Besides, positive definiteness of V leads to the conclusion that it is bounded from below. Hence, the limit $\lim_{t \rightarrow \infty} V(t, x(t))$ exists. Set

$$\lim_{t \rightarrow \infty} V(t, x(t)) = L.$$

It is clear that $L > 0$ or $L = 0$. Assume that $L > 0$. Since ψ is a continuous function, it has a minimum value on the closed interval $[L, V(t_0, x(t_0))]$. We denote this value by m . Note that $V(\sigma_k, x(\sigma_k)) \in [L, V(t_0, x(t_0))]$ for all $k \in \{1, 2, 3, \dots\}$. According to the condition (ii), we have

$$V(\sigma_k, x + F_k(x)) - V(\sigma_k, x) \leq -\psi(V(\sigma_k, x)).$$

This leads to the inequality

$$V(\sigma_k, x(\sigma_k +)) - V(\sigma_k, x(\sigma_k)) \leq -\psi(V(\sigma_k, x(\sigma_k))) \leq -m.$$

Owing to the nature of its defining properties, it is true for the function V that

$$V(\sigma_k, x(\sigma_k +)) \geq V(\sigma_{k+1}, x(\sigma_{k+1}))$$

for each $k \in \{1, 2, 3, \dots\}$. This property allows to write the following inequality

$$\begin{aligned}
V(\sigma_n, x(\sigma_n +)) &\leq V(\sigma_n, x(\sigma_n +)) + \sum_{k=1}^n [V(\sigma_{k-1}, x(\sigma_{k-1} +)) \\
&\quad - V(\sigma_k, x(\sigma_k))] \\
&\leq V(\sigma_0, x(\sigma_0 +)) - mn,
\end{aligned}$$

for any $n \in \mathbb{N}$. It can be seen that V becomes negative for the values of $n > \frac{V(\sigma_0, x(\sigma_0 +))}{m}$. However, this contradicts with the assumption that V is positive definite. In this case, it is not possible for L to be positive and hence $L = 0$. That is to say,

$$\lim_{t \rightarrow \infty} V(t, x(t)) = 0.$$

Since V is positive definite, there exists a continuous, strictly increasing function $\alpha: [0, \gamma] \rightarrow [0, \infty]$ with $\alpha(0) = 0$, bounding V from below as $V(t, x) \geq \alpha(\|x\|)$ for all $(t, x) \in I \times N_\gamma$. Then, we get

$$0 = \lim_{t \rightarrow \infty} V(t, x(t)) \geq \lim_{t \rightarrow \infty} \alpha(\|x(t)\|) = \alpha(\lim_{t \rightarrow \infty} \|x(t)\|),$$

from which it follows that $\lim_{t \rightarrow \infty} x(t) = 0$. This ultimately shows that the trivial solution $x = 0$ of the impulsive system (1.1) with generalized type piecewise constant argument is asymptotically stable. \square

OUTCOMES AND DISCUSSION

The study and simulation of dynamic systems across various scientific and engineering disciplines rely extensively on differential equations. In recent decades, there has been a growing interest in the stability analysis of impulsive and delay differential systems. Numerous studies have employed Lyapunov functionals (Xi, 2018:1; Yu and Cao, 2018:153) and other generalized methods to derive sufficient conditions for the stability of such systems. However, many of these approaches rely on intricate functional constructions or impose restrictive assumptions, potentially limiting their practical applicability.

In particular, impulsive systems with arguments that depend discontinuously on time pose significant analytical challenges. These hybrid systems, characterized by the interplay of continuous evolution, abrupt state changes, and memory effects, demand novel analytical techniques that go beyond the conventional framework.

This study contributes to the existing literature by establishing new sufficient conditions for the stability of impulsive differential equations with generalized piecewise constant arguments. Unlike traditional methods, the approach adopted here utilizes Lyapunov's second method without the need for constructing functionals tailored to the delay or memory structure. This direct method simplifies the stability analysis while maintaining mathematical rigor and generality.

A key innovation of the study is the introduction of a comparison framework between the original delayed system and an auxiliary non-delayed system. This framework allows for the transfer of stability properties between the two systems and offers a deeper understanding of the qualitative behavior of impulsive systems with nonstandard argument structures. The results obtained enhance the theoretical foundation for analyzing the stability of such hybrid dynamical systems.

Looking forward, several promising research directions emerge from this work. Future studies could aim to generalize the proposed framework to encompass more complex settings, such as systems with multiple or distributed delays, and state-dependent impulses, each of which poses additional layers of analytical complexity. Furthermore, the development of computational algorithms to verify the derived stability conditions and their application to real-world models in fields such as engineering, biology, and economics would further demonstrate the utility and adaptability of the theoretical contributions presented in this study.

REFERENCES

- Akhmet, M.U., and Yılmaz, E. (2012). Global exponential stability of neural networks with non-smooth and impact activations, *Neural Networks*, 34, 18-27.
- Bereketoğlu, H., Seyhan, G., and Ogun, A. (2010). Advanced impulsive differential equations with piecewise constant arguments. *Mathematical Modelling and Analysis*, 15(2), 175-187.
- Büyükkahraman, M. L. (2022). Existence of periodic solutions to a certain impulsive differential equation with piecewise constant arguments. *Eurasian Mathematical Journal*, 13(4), 54-60.
- Castillo, S., Pinto, M., and Torres, R. (2019). Asymptotic formulae for solutions to impulsive differential equations with piecewise constant argument of generalized type. *Electronic Journal of Differential Equations*, 2019(40), 1-22.
- Cengiz, N. and Aruğaslan Çiçin, D. (2022). Asymptotic stability of an impulsive Huang-Li financial model. 7. *Uluslararası Uygulamalı Bilimler Kongresine Sunulmuş Tam Metin Bildiri*, 402-419.
- Chiu, K-S., (2013). Existence and global exponential stability of equilibrium for impulsive cellular neural network models with piecewise alternately advanced and retarded argument. *Abstract and Applied Analysis*, Article ID: 196139, 13 pages.
- Chiu, K-S., (2022). Stability analysis of periodic solutions in alternately advanced and retarded neural network models with impulses. *Taiwanese Journal of Mathematics*, 26(1), 137-176.
- Gyori, I., and Ladas, G. (1991). *Oscillation Theory of Delay Differential Equations with Applications*. Oxford University Press, New York.
- Karakoç, F. (2020). Impulse effect on the food-limited population model with piecewise constant argument. *Applications and Applied Mathematics: An International Journal*, 15(2), 957-969.
- Miller, R. K., and Michel, A. (1982). *Ordinary Differential Equations*. New York: Academic Press.
- Samoilenko, A. M., and Perestyuk, N. A. (1995). *Impulsive Differential Equations*. World Scientific Publishing.
- Rouche, N., Habets, P., and Laloy, M. (1977). *Stability Theory by Lyapunov's Direct Method*, New York, Springer-Verlag.
- Xi, Q. (2018). Razumikhin-type theorems for impulsive differential equations with piecewise constant argument of generalized type. *Advances in Difference Equations*, 2018:267, 16 pages.
- Yu, T., and Cao, D. (2018). Stability analysis of impulsive neural networks with piecewise constant arguments. *Neural Process Letters*, 47, 153-165.
- Zhang, G-L. (2017). Oscillation of Runge-Kutta methods for advanced impulsive differential equations with piecewise constant arguments. *Advances in Difference Equations*, 2017:32, 13 pages.

Electronic Structure, Reactivity, and Intermolecular Interaction Studies on a Coumarin Derivative via DFT and Hirshfeld Surface Analysis

Sevgi KANSIZ¹

Okan ŞİMŞEK²

- 1- Asst. Prof.; Samsun University, Faculty of Engineering and Natural Sciences, Department of Fundamental Sciences. sevgi.kansiz@samsun.edu.tr ORCID No: 0000-0002-8433-7975.
- 2- Res. Asst.; Ondokuz Mayıs University, Faculty of Science, Department of Physics. okan.simsek@omu.edu.tr ORCID No: 0000-0003-1157-4088.

ABSTRACT

A comprehensive theoretical investigation was carried out on the coumarin derivate compound, $C_{14}H_{14}O_4$, using density functional theory (DFT) and a suite of wavefunction-based analyses. The optimized geometry and frontier molecular orbital analysis reveal that the HOMO and LUMO are predominantly localized over the coumarin core, with a HOMO–LUMO gap of 3.35 eV, suggesting moderate chemical reactivity. Global descriptors derived from orbital energies confirm the ability of the molecule to function as both an electron donor and acceptor, consistent with its relatively high electronegativity ($\chi = 7.14$ eV) and moderate hardness ($\eta = 1.68$ eV). Molecular electrostatic potential (MEP) mapping highlights the carbonyl oxygen atoms as the most favorable sites for electrophilic attack, whereas the aromatic hydrogen regions serve as potential nucleophilic targets. Electron localization analyses (ELF and LOL) demonstrate strong localization around π -bonds and oxygen lone pairs, while regions of reduced localization correspond to intermolecular interaction sites. Noncovalent interaction features were further confirmed by reduced density gradient (RDG) and Hirshfeld surface analyses, which emphasize the role of weak C–H \cdots O hydrogen bonds, dispersion forces, and steric contacts in stabilizing the crystal structure. Collectively, the findings provide a detailed understanding of the electronic structure, reactivity profile, and intermolecular interactions of the coumarin compound, offering insights into its potential applications in materials and bioactive molecular design.

Keywords – Coumarin, DFT, MEP, HOMO-LUMO, ELF/LOL.

INTRODUCTION

The coumarin scaffold, chemically defined as 2H-1-benzopyran-2-one and classified within the subgroup of lactones, constitutes a privileged structural motif extensively explored in both natural products and synthetic chemistry (Lončarić et al., 2020). Coumarin derivatives occur naturally in numerous plants, such as tonka bean, *Angelica dahurica*, and species of *Ferulago*, and in these plants they are frequently concentrated in the roots (Venugopala et al., 2013; Matos et al., 2015). Because of their conjugated π system and electron-rich nature, coumarin derivatives exhibit luminescent properties that make them applicable as fluorescent probes and as photocleavable protecting groups in chemical and biological systems (Annunziata et al., 2020). In medicinal chemistry, coumarins have demonstrated a wide spectrum of bioactivities, encompassing anticoagulant, antioxidant, and anti-inflammatory effects as well as antimicrobial, anti-HIV, and anticancer properties (Pisani et al., 2022; Balewski et al., 2021). For example, coumarin-based hybrids have been reported to inhibit key enzymes implicated in neurodegenerative diseases, including monoamine oxidase B

(MAO-B), acetylcholinesterase (AChE), and butyrylcholinesterase (BuChE). This inhibitory activity provides promising avenues for the design of multitarget drugs aimed at managing complex neurological disorders (Hussain et al., 2019). In addition to their biological potential, the synthetic versatility of the coumarin core—achievable through classical reactions such as the Pechmann condensation, the Perkin reaction, and the Knoevenagel condensation—facilitates the preparation of structurally diverse derivatives with tailored functional properties (Gulati et al., 2021; Vekariya et al., 2014). Recent studies have emphasized the pharmacological significance of C-3 substituted coumarin derivatives, which display enhanced activity against pathogens such as *Staphylococcus aureus* and thus hold considerable promise in the fight against antimicrobial resistance (Tandel et al., 2025). Overall, the combination of structural modifiability, multifunctionality, and potent bioactivity renders coumarin derivatives highly valuable scaffolds in the continuing search for novel therapeutic agents.

In this study, a comprehensive theoretical investigation was carried out on a coumarin-derived compound in order to explore its structural, electronic, and supramolecular features. Density Functional Theory (DFT) calculations were employed to optimize the molecular geometry and to examine the electronic distribution in detail. The frontier molecular orbital (HOMO–LUMO) analysis was conducted to evaluate the energy gap and to predict the chemical reactivity and stability of the system. Molecular electrostatic potential (MEP) mapping was utilized to identify electrophilic and nucleophilic regions, thus indicating potential reactive sites. To further elucidate the electronic topology, electron localization function (ELF) and localized orbital locator (LOL) analyses were performed, providing insights into electron-pair distribution and bonding characteristics. Noncovalent Interaction–Reduced Density Gradient (NCI-RDG) analysis enabled the visualization of weak interactions such as van der Waals forces, hydrogen bonds, and π – π stacking, highlighting the supramolecular features of the compound. Moreover, Hirshfeld surface analysis, generated using the CrystalExplorer21 program, was applied to quantify the intermolecular contacts in the solid state through *d*_{norm}, *d*_i, *d*_e, and shape index surfaces, together with two-dimensional fingerprint plots (Simsek et al., 2023; Ozsanlı et al., 2024). Collectively, these computational results contribute to a deeper understanding of the electronic and interactional properties of coumarin derivatives.

Materials and Method

In this study, Density Functional Theory (DFT) calculations were carried out using the Gaussian 09W software package (Frisch et al., 2016), and molecular visualizations were generated with GaussView 6.0 (Dennington et al., 2016). The geometry optimization and subsequent electronic structure analyses were performed at the B3LYP level of theory

(Becke, 1993; Lee et al., 1988) with the 6-31G(d,p) basis set, ensuring a reliable balance between computational accuracy and efficiency. These procedures enabled the evaluation of the frontier molecular orbital (HOMO-LUMO) distributions, the energy gap, and the Molecular Electrostatic Potential (MEP) surface. In particular, the MEP surface was employed to identify nucleophilic and electrophilic regions within the molecule, thereby providing a comprehensive framework for mapping electron density distribution and visualizing electrostatic interaction patterns.

The intermolecular interactions within the crystal lattice of the coumarin derivative compound were examined using Hirshfeld surface analysis (Spackman and Jayatilaka, 2009), and the corresponding two-dimensional fingerprint plots were generated with the CrystalExplorer21 software package (Spackman et al., 2021; Turner et al., 2017). This method allows the visualization of intermolecular contact distances and the identification of regions of significant noncovalent interactions. Additionally, fingerprint plots derived from the Hirshfeld surface were employed to quantify the relative contributions of distinct atom–atom contacts, thus providing a comprehensive understanding of the molecular packing features (Simsek et al., 2022). The ELF, LOL, and RDG analyses were modeled using the Multiwfn 3.7 (Lu and Chen, 2012) package and VMD (Humphrey et al., 1996).

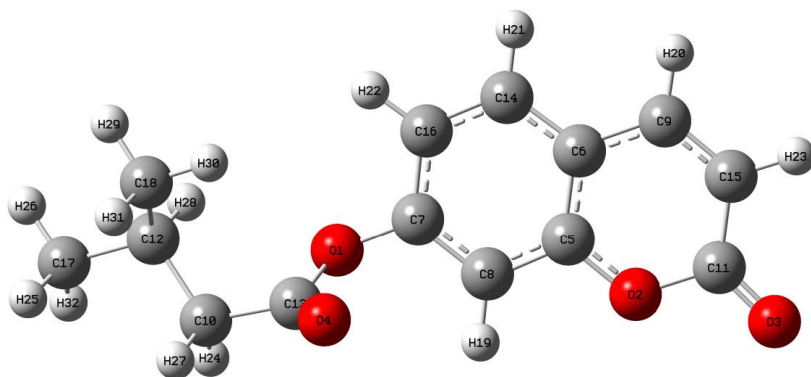


Figure 1: The optimized structure of $C_{14}H_{14}O_4$.

RESULTS AND DISCUSSION

MEP surface analysis of C₁₄H₁₄O₄

The molecular electrostatic potential (MEP) surface of the optimized C₁₄H₁₄O₄ compound (Fig. 1), computed at the B3LYP/6-31G(d,p) level maps electron-rich (negative, red) and electron-poor (positive, blue) regions, providing a physically meaningful descriptor of reactive sites (El Kalai et al., 2023; Arumugam et al., 2021). In the coumarin framework (Fig. 2), the most negative potential concentrates around the carbonyl oxygen atoms of the lactone/ester portion, consistent with their high electron density and well-established role as strong hydrogen-bond acceptors (Adhikari et al., 2024; El Bakri et al., 2024). Complementarily, the carbonyl bears a positive potential, identifying it as a plausible locus for nucleophilic attack in polar reactions. Positive potential is also observed about aromatic and benzylic C–H groups, especially those adjacent to electronegative atoms, in line with the ability of polarized C–H bonds to participate in C–H···O hydrogen bonding (Peter et al., 2013; Adhikari et al., 2023). This polarity pattern—electron-rich oxygen sites and electron-poor C=O carbon/C–H regions—indicates multiple noncovalent interaction modes available to the molecule (H-bond accepting at O, H···O contacts at polarized hydrogens), a behavior widely noted for coumarin scaffolds in chemical and biological contexts. Taken together with frontier-orbital descriptors, the MEP map provides a coherent picture of electrophilic and nucleophilic preferences that underpins the observed reactivity profile of this coumarin derivative (Al-thamili et al., 2020).

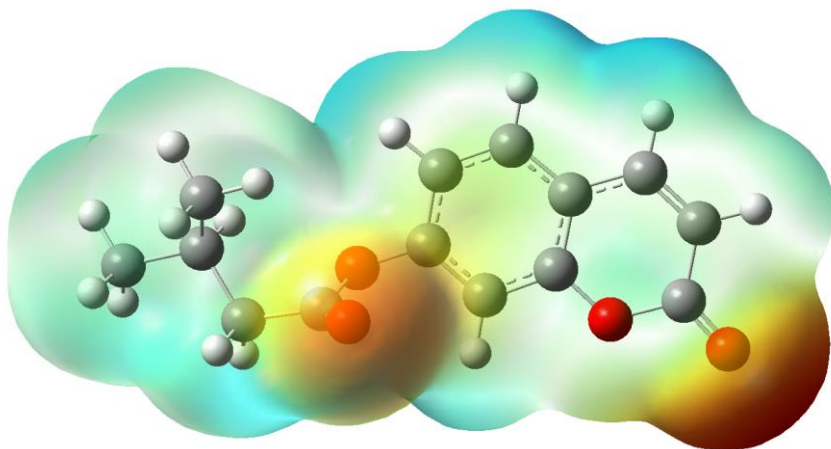


Figure 2: MEP surface of C₁₄H₁₄O₄.

Frontier molecular orbital analysis of $C_{14}H_{14}O_4$

Analysis of the frontier molecular orbitals shows that both the HOMO and LUMO are mainly concentrated on the $C_{14}H_{14}O_4$ framework. As illustrated in Fig. 3, the orbital distribution suggests that nucleophilic and electrophilic interactions are most likely directed toward the carbonyl group and the conjugated aromatic ring, where the frontier orbitals significantly overlap. Further insight into the electronic nature of the compound can be obtained from global reactivity descriptors derived from the frontier orbital energies (Table 1). The HOMO energy (-9.08 eV) and LUMO energy (-5.73 eV) give a HOMO–LUMO gap of 3.35 eV, pointing to a moderate barrier for electron transfer and implying a balanced reactivity profile. The corresponding ionization potential (IP = 9.08 eV) and electron affinity (EA = 5.73 eV) indicate that the molecule can act as both an electron donor and acceptor depending on the environment. The calculated chemical hardness ($\eta = 1.68$ eV) and electronegativity ($\chi = 7.14$ eV) further suggest that the coumarin system possesses a relatively electron-withdrawing character, favoring interactions in polar media and in the presence of hydrogen-bond donors.

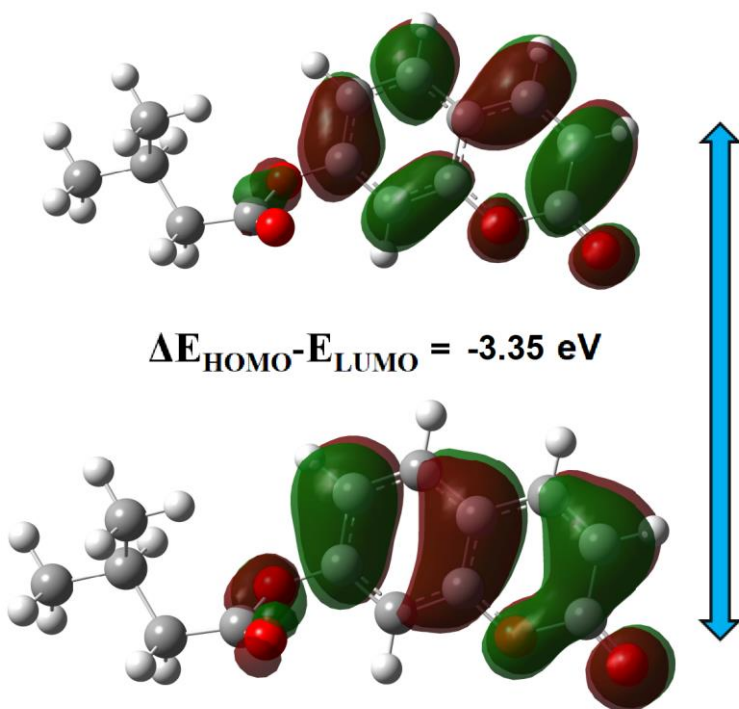


Figure 3: HOMO-LUMO surface of $C_{14}H_{14}O_4$.

Table 1: The energy values of the global reactivity parameters of $C_{14}H_{14}O_4$.

Parameters	
E_{HOMO} (eV)	-9.08
E_{LUMO} (eV)	-5.73
Energy gap (eV)	3.35
Ionization potential ($I=-E_{HOMO}$)	9.08
Electron affinity ($A=-E_{LUMO}$)	5.73
Electronegativity ($\chi=(I+A)/2$)	7.14
Hardness ($\eta=(I-A)/2$)	1.68
Softness ($S=1/2\eta$)	0.30

ELF and LOL analysis of $C_{14}H_{14}O_4$

In terms of electron localization, the ELF maps (Fig. 4, left) reveal strong electron density around the aromatic π -system and the lone pairs of oxygen atoms, appearing as intense red and yellow regions in both 2D contour and 3D surface representations. These features indicate well-defined electron pairs associated with π - and σ -bonds as well as nonbonding domains on electronegative centers. The complementary LOL maps (Fig. 4, right) highlight compact orbital clusters around the ring carbons and oxygen sites, displaying narrower distributions that support the orbital segregation depicted by ELF. Regions of reduced localization are observed in the intermolecular space and at the periphery of the molecule, reflecting diffuse electron density that facilitates weak noncovalent interactions in the crystal packing.

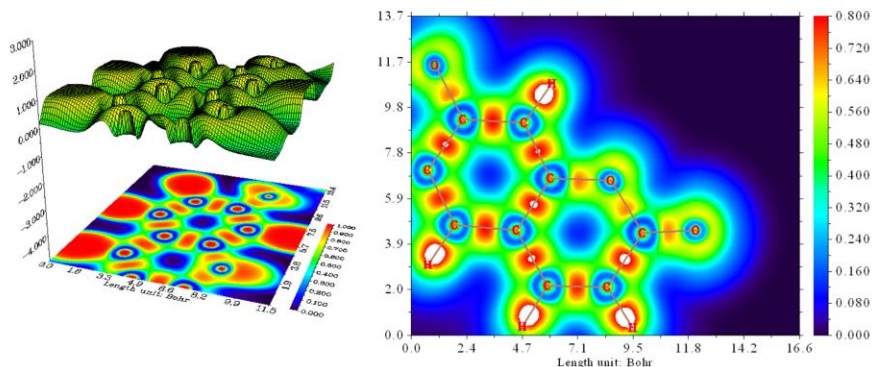


Figure 4: The electron localization function (ELF) (left), and localized orbital locator (LOL) (right) maps of $C_{14}H_{14}O_4$.

NCI-RDG analysis of $C_{14}H_{14}O_4$

A detailed picture of the noncovalent interactions and electron distribution in the coumarin derivative is provided by the wavefunction-based analyses in Fig. 5. The RDG scatter plot (Fig. 5, up) classifies the interactions according to $\text{sign}(\lambda_2)\rho$ values. Negative regions (blue, -0.04 to

−0.01 a.u.) correspond to attractive forces, reflecting possible hidden hydrogen-bond acceptor contributions at electronegative centers. The zone near zero (green, ± 0.01 a.u.) represents weak dispersion-type van der Waals contacts, while positive values (red, +0.01 to +0.04 a.u.) indicate steric repulsions typically arising from closely positioned substituents or terminal groups. The RDG isosurface (Fig. 5, down) further illustrates the spatial distribution of these effects. Small greenish patches observed between oxygen and adjacent hydrogen atoms suggest weak C–H \cdots O interactions, whereas the red regions concentrated within the core of the coumarin ring reflect steric congestion inside the aromatic framework.

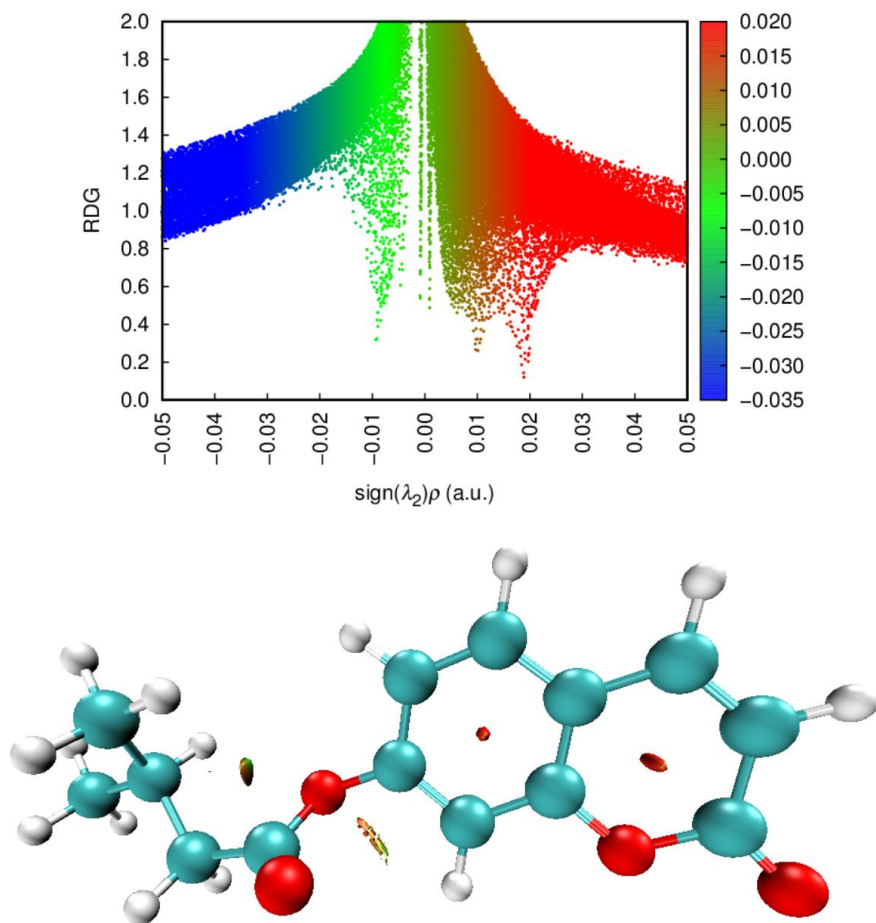


Figure 5: RDG scatter plot and RDG isosurface of $C_{14}H_{14}O_4$.

Hirshfeld surface analysis of $C_{14}H_{14}O_4$

The Hirshfeld surface analysis of $C_{14}H_{14}O_4$ (d_{norm} range −0.1669 to 1.2306) indicates that the crystal packing is dominated by van-der-Waals

H \cdots H contacts (44%), with significant contributions from O \cdots H interactions (28%) and C \cdots H contacts (18%). The negative d_{norm} minima (≈ -0.167) coincide with localized close contacts near the carbonyl and ester oxygen atoms, consistent with directional C–H \cdots O interactions rather than classical strong hydrogen bonds. The shape-index map shows no pronounced complementary red/blue triangles over the aromatic rings, and the curvedness surface exhibits mainly curved regions with only minor low-curvedness patches, indicating an absence of extensive face-to-face π – π stacking.

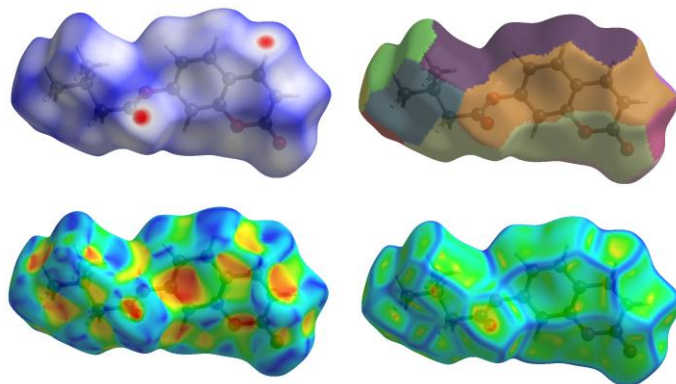


Figure 6: The Hirshfeld surfaces of C₁₄H₁₄O₄.

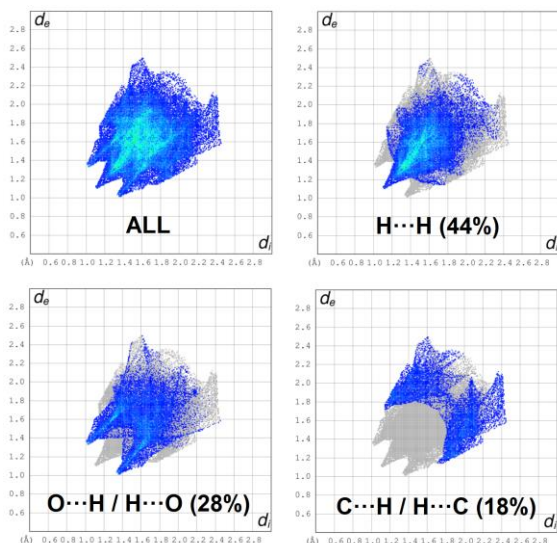


Figure 7: The 2D fingerprint plots of C₁₄H₁₄O₄.

CONCLUSION

The combined computational analyses highlight that the electronic and structural properties of $C_{14}H_{14}O_4$ are strongly governed by the coumarin backbone. The HOMO–LUMO distribution and global reactivity descriptors reveal a system with balanced electron-donating and -accepting capabilities, supported by a moderate energy gap that reflects both chemical stability and reactivity. MEP surfaces and ELF/LOL maps consistently point to oxygen centers and aromatic π -systems as the primary reactive sites. RDG and Hirshfeld surface analyses further demonstrate that the crystal packing is stabilized mainly by van der Waals $H\cdots H$ contacts, supplemented by directional $C-H\cdots O$ interactions and minor $C-H\cdots \pi$ contributions, while steric effects arise within the aromatic core. Altogether, these computational findings provide a coherent picture of the molecule's reactivity and intermolecular behavior, reinforcing its potential as a versatile coumarin derivative for future functional and applied studies.

REFERENCE

- Al-thamili, D. M., Almansour, A. I., Arumugam, N., Kansız, S., Dege, N., Soliman, S. M., Azam, M., and Kumar, R. S. (2020). Highly functionalized N-1-(2-pyridinylmethyl)-3,5-bis[(E)-arylmethylidene]tetrahydro-4(1H)-pyridinones: Synthesis, characterization, crystal structure and DFT studies. *Journal of Molecular Structure*, 1222, 128940.
- Adhikari, S., Nath, S., Kansız, S., Balidya, N., Paul, A. K., Dege, N., Sahin, O., Mahmoudi, G., Verma, A. K., and Safin, D. A. (2024). Zinc(II) coordination compound with N'-(pyridin-2-ylmethylene)nicotinohydrazide: Synthesis, crystal structure, computational and cytotoxicity studies. *Journal of Inorganic Biochemistry*, 257, 112598.
- Adhikari, S., Sheikh, A. H., Kansız, S., Dege, N., Baildya, N., Mahmoudi, G., Choudhury, N. A., Butcher, R. J., Kaminsky, W., Talledo, S., Lopato, E. M., Bernhard, S., and Kłak, J. (2023). Supramolecular Co(II) complexes based on dithiolate and dicarboxylate ligands: Crystal structures, theoretical studies, magnetic properties, and catalytic activity studies in photocatalytic hydrogen evolution. *Journal of Molecular Structure*, 1285, 135481.
- Annunziata, F., Pinna, C., Dallavalle, S., Tamborini, L., and Pinto, A. (2020). An overview of coumarin as a versatile and readily accessible scaffold with broad-ranging biological activities. *International Journal of Molecular Sciences*, 21(13), 4618.
- Arumugam, N., Almansour, A. I., Kumar, R. S., Yeswanthkumar, S., Padmanaban, R., Arun, Y., Kansız, S., Dege, N., Manohar, T. S., and Venketesh, S. (2021). Design, stereoselective synthesis, computational studies and cholinesterase inhibitory activity of novel spiropyrolidinoquinoxaline tethered indole hybrid heterocycle. *Journal of Molecular Structure*, 1225, 129165.

- Balewski, Ł., Szulta, S., Jalińska, A., and Kornicka, A. (2021). A mini-review: Recent advances in coumarin-metal complexes with biological properties. *Frontiers in Chemistry*, 9, 704531.
- Becke, A. D. (1993). Density-functional thermochemistry. III. The role of exact exchange. *The Journal of Chemical Physics*, 98(7), 5648–5652.
- Dennington, R., Keith, T. A., and Millam, J. M. (2016). GaussView 6.0.16. *Semichem Inc., Shawnee Mission*.
- El Bakri, Y., Kurbanova, M., Ahsin, A., Karthikeyan, S., Maharramov, A., Al-Salahi, R., Kansız, S., Mali, S. N., and Ashfaq, M. (2024). Synthesis, crystal structure investigation, and theoretical approaches to discover potential 6-bromo-3-cyanocoumarin as a potent inhibitor of MetAP2 (methionine aminopeptidase). *Chemical Physics Impact*, 8, 100477.
- El Kalai, F., Abraham, C. S., Kansiz, S., Oulmidi, A., Muthu, S., Prasana, J. C., Dege, N., Abuelizz, H. A., Al-Salahi, R., Benchat, N., and Karrouchi, K. (2023). Synthesis, crystal structure, and computational investigations of 2-(2-(4-fluorophenyl)-2-oxoethyl)-6-methyl-5-(4-methylbenzyl)pyridazin-3(2H)-one as antiviral agent. *Crystals*, 13(7), 1098.
- Frisch, M. J., Trucks, G. W., Schlegel, H. B., Scuseria, G. E., Robb, M. A., Cheeseman, J. R., Montgomery Jr., J. A., Vreven, T., Kudin, K. N., Burant, J. C., Millam, J. M., Iyengar, S. S., Tomasi, J., Barone, V., Mennucci, B., Cossi, M., Scalmani, G., Rega, N., Petersson, G. A., Nakatsuji, H., Hada, M., Ehara, M., Toyota, K., Fukuda, R., Hasegawa, J., Ishida, M., Nakajima, T., Honda, Y., Kitao, O., Nakai, H., Klene, M., Li, X., Knox, J. E., Hratchian, H. P., Cross, J. B., Bakken, V., Adamo, C., Jaramillo, J., Gomperts, R., Stratmann, R. E., Yazyev, O., Austin, A. J., Cammi, R., Pomelli, C., Ochterski, J. W., Ayala, P. Y., Morokuma, K., Voth, G. A., Salvador, P., Dannenberg, J. J., Zakrzewski, V. G., Dapprich, S., Daniels, A. D., Strain, M. C., Farkas, O., Malick, D. K., Rabuck, A. D., Raghavachari, K., Foresman, J. B., Ortiz, J. V., Cui, Q., Baboul, A. G., Clifford, S., Cioslowski, J., Stefanov, B. B., Liu, G., Liashenko, A., Piskorz, P., Komaromi, I., Martin, R. L., Fox, D. J., Keith, T., Al-Laham, M. A., Peng, C. Y., Nanayakkara, A., Challacombe, M., Gill, P. M. W., Johnson, B., Chen, W., Wong, M. W., Gonzalez, C., and Pople, J. A. (2016). Gaussian 09, Revision A.02. *Gaussian, Inc., Wallingford CT*.
- Gulati, S., Singh, R., and Sangwan, S. (2021). A review on convenient synthesis of substituted coumarins using reusable solid acid catalysts. *RSC Advances*, 11, 29130–29155.
- Humphrey, W., Dalke, A., and Schulten, K. (1996). VMD: visual molecular dynamics. *Journal of Molecular Graphics*, 14(1), 33–38.
- Hussain, M. I., Syed, Q. A., Khattak, M. N. K., et al. (2019). Natural product coumarins: Biological and pharmacological perspectives. *Biologia*, 74(9), 863–888.
- Lee, C., Yang, W., and Parr, R. G. (1988). Development of the Colle–Salvetti correlation-energy formula into a functional of the electron density. *Physical Review B*, 37(2), 785–789.
- Lončarić, M., Gašo-Sokač, D., Jokić, S., and Molnar, M. (2020). Recent advances in the synthesis of coumarin derivatives from different starting materials. *Biomolecules*, 10(1), 151.
- Lu, T., and Chen, F. (2012). Multiwfn: A multifunctional wavefunction analyzer. *Journal of Computational Chemistry*, 33(5), 580–592.

- Matos, M. J., Santana, L., Uriarte, E., Abreu, O. A., Molina, E., and Yáñez, M. (2015). Coumarins—An important class of phytochemicals. In *Phytochemicals: Isolation, Characterisation and Role in Human Health*, 25, 533–536).
- Ozsanlı, H., Simsek, O., Yılmaz, O. R., Cicek, C., Agar, E., Coruh, U., and Vazquez-Lopez, E. M. (2024). Synthesis, crystal structure, Hirshfeld surface analysis, supramolecular and computational investigation of the (E)-4-methoxy-2-(((2-methoxy-5-(trifluoromethyl)phenyl)imino)methyl) phenol compound. *Journal of Structural Chemistry*, 65(5) 946–957.
- Peter, P., Murray, J. S., and Clark, T. (2013). Halogen bonding and other σ -hole interactions: A perspective. *Physical Chemistry Chemical Physics*, 15(27), 11178–11189.
- Pisani, L., Catto, M., Muncipinto, G., Nicolotti, O., Carrieri, A., Rullo, M., Stefanachi, A., Leonetti, F., and Altomare, C. (2022). A twenty-year journey exploring coumarin-based derivatives as bioactive molecules. *Frontiers in Chemistry*, 10, 1002547.
- Simsek, O., Ashfaq, M., Tahir, M. N., Ozturk, S., and Agar, E. (2023). Synthesis and characterizations of the Schiff base derived from 2-hydroxy-5-nitrobenzaldehyde along with Hirshfeld surface analysis and computational study. *Journal of Structural Chemistry*, 64(5), 942–953.
- Simsek, O., Dincer, M., Dege, N., Saif, E., Yilmaz, I., and Cukurovali, A. (2022). Crystal structure and Hirshfeld surface analysis of (Z)-4-{[4-(3-methyl-3-phenylcyclobutyl) thiazol-2-yl] amino}-4-oxobut-2-enoic acid. *Acta Crystallographica Section E: Crystallographic Communications*, 78(2), 120–124.
- Spackman, M. A., and Jayatilaka, D. (2009). Hirshfeld surface analysis. *CrystEngComm*, 11(1), 19–32.
- Spackman, P. R., Turner, M. J., McKinnon, J. J., Wolff, S. K., Grimwood, D. J., Jayatilaka, D., and Spackman, M. A. (2021). CrystalExplorer: a program for Hirshfeld surface analysis, visualization and quantitative analysis of molecular crystals. *Journal of Applied Crystallography*, 54(3), 1006–1011.
- Tandel, P., Khalifa, Z., Upadhyay, R., et al. (2025). Investigation of recent advancement in the pharmacological potential of C-3 substituted coumarin derivatives against *S. aureus*. *Discover Chemistry*, 2, 58.
- Turner, M. J., MacKinnon, J. J., Wolff, S. K., Grimwood, D. J., Spackman, P. R., Jayatilaka, D., and Spackman, M. A. (2017). CrystalExplorer Ver. 17.5. University of Western Australia. <http://hirshfeldsurface.net>
- Venugopala, K. N., Rashmi, V., and Odhav, B. (2013). Review on natural coumarin lead compounds for their pharmacological activity. *BioMed Research International*, 2013, 963248.
- Vekariya, R. H., and Patel, H. D. (2014). Recent advances in the synthesis of coumarin derivatives via Knoevenagel condensation: A review. *Synthetic Communications*, 44(19), 2756–2788.

A Photocatalytic Investigation of Benzyl Alcohol Oxidation

Osman Tayyar ARLI¹

Halil Zeki GÖK¹

1-Doktorand; Burdur Mehmet Akif Ersoy University, Faculty of Science and Letters, Department of Chemistry, Burdur-Türkiye, osmantayyararli@hotmail.com, ORCID: 0000-0001-7619-2668

1-Prof. Dr.; Burdur Mehmet Akif Ersoy University, Faculty of Science and Letters, Department of Chemistry, Burdur-Türkiye, zekigok@mehmetakif.edu.tr, ORCID: 0000-0001-7641-2683

ABSTRACT

The oxidation of benzyl alcohol to benzaldehyde is essential for producing fine chemicals and aromatic aldehydes. It is also important as a model reaction for understanding more complex oxidative processes. Frequently referenced in photocatalytic systems, this reaction is considered a critical test reaction for elucidating the fundamental mechanism and informing new catalyst designs. This study systematically investigated the photooxidative conversion of benzyl alcohol without a catalyst. Reactions were carried out in specially designed photoreactors using red (640 nm) and blue (420 nm) LED light sources and different types of oxidants and solvents. The highest conversion was observed with a yield of 34.7% benzaldehyde using TBHP (1/32). H_2O_2 exhibited moderate activity, and m-CPBA was notable for its low selectivity and byproduct formation. Solvent studies showed that toluene provided the highest conversion, while water and IPA offered lower yields. Wavelength tests revealed that blue light at 420 nm was significantly more effective than red light. These results demonstrate that light wavelength, oxidant type, and solvent selection are critical factors in photooxidation processes. This study is an important reference for understanding photooxidative mechanisms in uncatalyzed systems and will guide future studies in catalyzed systems.

Keywords – Benzyl Alcohol Oxidation, Catalyst, Photocatalyst.

INTRODUCTION

Selective oxidation of benzyl alcohol is a common transformation in organic synthesis. The main product of this reaction, benzaldehyde, is of great interest due to its use as an intermediate chemical in the perfume, flavor, dye, and pharmaceutical industries (Mallat & Baiker, 2004). However, conventional oxidation methods often rely on stoichiometric and environmentally hazardous oxidants, resulting in disadvantages such as waste generation, toxicity, and energy consumption (Sheldon, 2016). In this context, methods that comply with green chemistry principles and offer high energy and atomic efficiencies have made photocatalytic approaches attractive for similar reactions. Photocatalysis is based on the generation of excited charge carriers (electrons (e^-)/holes (h^+)) when the catalyst absorbs light. These carriers then interact with acceptors, such as oxygen, on the surface to produce reactive oxygen species (ROS) (Fujishima & Honda, 1972). Thus, the oxidation of benzyl alcohol to benzaldehyde can often be achieved at room temperature and atmospheric pressure using molecular oxygen, which provides significant advantages in terms of process safety and

sustainability (Mamba & Mishra, 2016). Due to the practicality and scalability of light irradiation, visible light-activated systems are increasingly sought after in the literature.

Semiconductor oxides, especially TiO_2 and ZnO , are the backbone of traditional photocatalytic oxidation studies. However, their wide band gaps and fast recombination can reduce quantum efficiency (Chen et al., 2010). To address these limitations, strategies such as surface/interface engineering (e.g., defect creation and oxygen vacancies), metal/metal oxide loadings, and carbon-based dopants (e.g., graphene and carbon nanotubes) have been reported. For instance, heterojunctions and Z-scheme architectures increase conductivity and charge carrier lifetime, which supports oxidation by improving light harvesting and charge separation (Chen et al., 2010).

$\text{g-C}_3\text{N}_4$ is an attractive photocatalyst for oxidation due to its activity under visible light, metal-free structure, and ease of synthesis (Mamba & Mishra, 2016). Loading transition metal complexes or phthalocyanines onto $\text{g-C}_3\text{N}_4$ can facilitate oxygen activation and promote the formation of species such as $^1\text{O}_2$ and $\text{O}_2^{\bullet-}$ (Parrino et al., 2018; Gök et al., 2026). Similarly, metal-organic frameworks (MOFs) are a promising platform for visible-light photocatalysis thanks to their large surface area, adjustable pore size, and light-absorbing organic linkers (Xianjiang et al., 2020). From a mechanistic perspective, the dominant reactive oxygen species (ROS) in oxidation is a key factor in determining selectivity. Singlet oxygen ($^1\text{O}_2$) can convert alcohols to aldehydes under mild conditions. However, more reactive species, such as superoxide ($\text{O}_2^{\bullet-}$) and the hydroxyl radical ($\bullet\text{OH}$), can lead to overoxidation and the formation of benzoic acid (Parrino et al., 2018; Gök et al., 2026). Therefore, parameters such as catalyst band positions, surface functions, solvent polarity, base/additives, and O_2 pressure must be optimized together. Light wavelength and intensity also influence charge carriers and consequently, pathway selection.

Supported and heterogeneous systems offer advantages in terms of catalyst recovery and long-term stability. Mesoporous silica supports, such as MCM-41 and SBA-15, have regular pore channels and a high surface area. These properties allow for good distribution of active centers and improved mass transfer. Immobilizing phthalocyanines, transition metal complexes, or MOF fragments on these supports reduces photocatalyst leaching and improves reusability (Gök et al., 2026; Gök et al., 2024). Additionally, charge transfer at the carrier-catalyst interface can positively impact visible light activity.

Controlling selectivity is critical for industrial applicability. Using mild bases (e.g., carbonates) to facilitate proton transfer, controlling water content, and optimizing oxygen partial pressure in the reaction medium have been reported to achieve high selectivity (Mallat & Baiker, 2004; Gök et al., 2025). Additionally, selecting the appropriate solvent (aprotic or polar

aprotic) and managing the intermediate species formed under light exposure can protect the target product by limiting excessive oxidation. Tuning the surface acid/base properties of the catalyst can also enable chemoselectivity between similar substrates. The performance of a reactor is also determined by its operating parameters. Batch reactors have mass transfer limitations. However, fluidized-bed or micro/flow reactor architectures can improve light-matter interactions and oxygen transfer, providing extended stability and higher spatial efficiency. The spectral power of the light source and the reactor's reflective surfaces and shortened light path directly impact quantum efficiency. Improvements in these areas suggest that differences in efficiency reported in the literature may be due not only to catalyst composition, but also to differences in hardware and operation (Chen et al., 2010).

Reusability and structural stability are key issues when scaling up photocatalysts. Loss of activity during repeated cycling can be attributed to mechanisms such as active site blockage, particle agglomeration, adsorption of organic intermediates, and metal leaching. Although these effects are mitigated in supported systems, maintaining performance requires appropriate regeneration protocols, such as mild thermal or UV cleaning (Gök et al., 2026; Gök et al., 2025; Gök et al., 2024). Long-term testing is critical for realistic application evaluations.

In general, the existing literature indicates that three axes are decisive in the photocatalytic oxidation of benzyl alcohol: (i) effective management of light absorption and charge separation, (ii) selective control of oxygen activation pathways, and (iii) ensuring stability and recovery of active centers through support/interface engineering. These research directions should be addressed together for sustainable and industrially applicable processes (Mallat & Baiker, 2004; Chen et al., 2010; Parrino et al., 2018; Xiao et al., 2020).

In light of this expanded framework, research on benzyl alcohol oxidation is expected to deepen around the design of visible-light photocatalysts, the selective production of reactive oxygen species, and stable immobilization strategies on mesoporous carriers. This will enable the scalability of processes with low energy consumption, minimal waste generation, and high chemoselectivity. A reliable technology base will be created for production lines compatible with green chemistry targets (Sheldon, 2016; Gök et al., 2026). To determine the effect of light alone on benzyl alcohol oxidation, free from the aforementioned factors that determine photocatalytic activity, a series of test reactions were carried out within the scope of this study.

RESULTS AND DISCUSSION

Photocatalytic conversion experiments of benzyl alcohol without a catalyst were conducted to investigate the effects of different oxidant types, solvent media, and light conditions. All reactions were carried out in Schlenk-type glass tubes and operated at 25 °C with a stirring speed of 200 rpm. The photoreactors were fabricated using a 3D printer (Gök et al; 2025; Gök et al., 2026). The first reactor was equipped with 10-watt red (640-nm) and blue (420-nm) LED lamps. The second reactor had arrays of six 32 W red LEDs to evaluate the effect of light intensity. The distance between the light source and the sample was fixed at 1.25 cm. Benzyl alcohol (0.03 mmol) was used as the substrate, and the preferred oxidants were tert-butyl hydroperoxide (TBHP, 70% in water), hydrogen peroxide (H₂O₂, 30%), and meta-chloroperbenzoic acid (m-CPBA, ≥77%). Substrate/oxidant ratios were tested from 1:1 to 1:32. Water, toluene, dichloromethane (DCM), isopropanol (IPA), dimethylformamide (DMF), and oxygen-saturated acetonitrile were used to investigate the effects of solvents. All reactions, except those investigating the effect of light intensity (15 min.), were run under light for two hours. Reaction products were analyzed by gas chromatography-flame ionization detection (GC-FID).

The experimental results demonstrate that the oxidation of benzyl alcohol varies significantly depending on the oxidant, solvent, light wavelength, and light intensity used. Experiments using TBHP demonstrate that conversion rates increase as the substrate-to-oxidant ratio decreases. Specifically, a benzaldehyde yield of 34.7% was achieved at a ratio of 1:32. The results obtained are given in Table 1. These results demonstrate that TBHP is a strong oxidant and that excess oxidant increases reaction efficiency.

Table 1. Results obtained with TBHP at different substrate/oxidant ratios^[a]

Entry	Substrat/Oxidant	Wavelength of Light (nm)	Benzaldehyde (%) ^[b]	Selectivity (%)
1	1/1	420	3.18	100
		660	0.33	
2	1/2	420	5.47	100
		660	0.39	
3	1/4	420	8.84	100
		660	0.26	
4	1/8	420	13.75	100
		660	0.47	
5	1/16	420	23.35	100
		660	0.59	
6	1/32	420	34.67	100
		660	0.65	

^aReaction conditions as solvent: acetonitrile (1 mL), substrate: benzyl alcohol (0.03 mmol), oxidant: TBHP, ^bConversions were determined by GC-FID. Reactions were conducted for 2 hours when carried out 25°C. Light source: LED lamps (10 W)

Subsequent studies revealed lower conversion rates with H₂O₂ than with TBHP. The highest yield was 17.4% at a 1/32 ratio. The results obtained are given in Table 2. These results suggest that, although H₂O₂ is effective in photooxidation, it is not as potent an oxidant as TBHP.

Table 2. Results obtained with H₂O₂ at different substrate/oxidant ratios^[a]

Entry	Substrat/Oxidant	Wavelength of Light (nm)	Benzaldehyde (%)	Selectivity (%)
1	1/2	420	5.42	100
		660	0.50	
2	1/8	420	9.65	100
		660	0.73	
3	1/32	420	17.42	100
		660	1.03	

^aReaction conditions as solvent: acetonitrile (1 mL), substrate: benzyl alcohol (0.03 mmol), oxidant: H₂O₂, ^bConversions were determined by GC-FID. Reactions were conducted for 2 hours when carried out 25°C. Light source: LED lamps (10 W)

Studies comparing oxidants revealed that TBHP provided the highest selectivity and efficiency. The results obtained are given in Table 3. H₂O₂ yielded moderate results, while m-CPBA produced low conversion and numerous byproducts, including benzoic acid, 1,4-benzoquinone, and benzyl benzoate. Therefore, TBHP can be concluded to be a more selective oxidant.

Table 3. Comparison of different oxidants at a ratio of 1/32^[a]

Entry	Oxidant	Wavelength of Light (nm)	Benzaldehyde (%)	Benzoic acid (%)	Benzyl Benzoate (%)	Aldehyde Selectivity (%)
1	TBHP	420	34.67	-	-	100
		660	0.65			
2	H ₂ O ₂	420	17.42	-	-	100
		660	1.03			
3	m-CPBA	420	1.61	3.17	89.44	1.7
		660	0.81	1.15	92.23	0.86

^aReaction conditions as solvent: acetonitrile (1 mL), substrate: benzyl alcohol (0.03 mmol), ^bConversions were determined by GC-FID. Reactions were conducted for 2 hours when carried out 25°C. Light source: LED lamps (10 W)

In studies investigating the effect of solvents on photocatalytic activity, high benzaldehyde yields were obtained in toluene; however, byproduct formation increased. Relatively low conversions were achieved in water and IPA media, while DMF media nearly suppressed the reaction. The

results obtained are given in Table 4. These results demonstrate that solvent polarity and oxygen solubility play critical roles in the reaction mechanism.

Table 4. Results obtained at 1/32 ratio in different solvents^[a]

Entry	Solvent	Wavelength of Light (nm)	Benzaldehyde (%)	Benzoic acid (%)	Benzyl Benzoate (%)	Aldehyde Selectivity (%)
1	ACN	420 660	34.67 0.65	-	-	100
2	H ₂ O	420 660	5.9 1.8	-	-	100
3	Toluene	420 660	23.9 4.0	23.3 -	-	50.6 100
4	DCM	420 660	12.4 1.3	-	19.3 -	39.1 100
5	IPA	420 660	5.7 0.67	-	-	100
6	DMF	420 660	3.7 0.35	-	-	100

^aReaction conditions as solvent: acetonitrile (1 mL), substrate: benzyl alcohol (0.03 mmol), oxidant: TBHP, ^bConversions were determined by GC-FID. Reactions were conducted for 2 hours when carried out 25°C. Light source: LED lamps (10 W)

In terms of wavelength, blue light (420 nm) was found to be much more efficient than red light (640 nm). Conversion was negligible under red light alone. The results obtained are given in Table 5. These results suggest that the system primarily propagates the reaction by absorbing high-energy photons.

Table 5. Effect of illumination at different wavelengths.

Entry	Substrat/Oxidant	Wavelength of Light (nm)	Benzaldehyde (%)	Aldehyde Selectivity (%)
1	1/32	420	34.67	100
2	1/32	420&660	7.85	100
3	1/32	660	0.65	100

^aReaction conditions as solvent: acetonitrile (1 mL), substrate: benzyl alcohol (0.03 mmol), oxidant: TBHP, ^bConversions were determined by GC-FID. Reactions were conducted for 2 hours when carried out 25°C. Light source: LED lamps (10 W)

Finally, studies investigating the effect of light intensity on photocatalytic activity revealed that the yield of benzaldehyde increased with increasing light intensity. However, the conversion rate plateaued at 96 W, suggesting that the system had reached the saturation point for photon absorption.

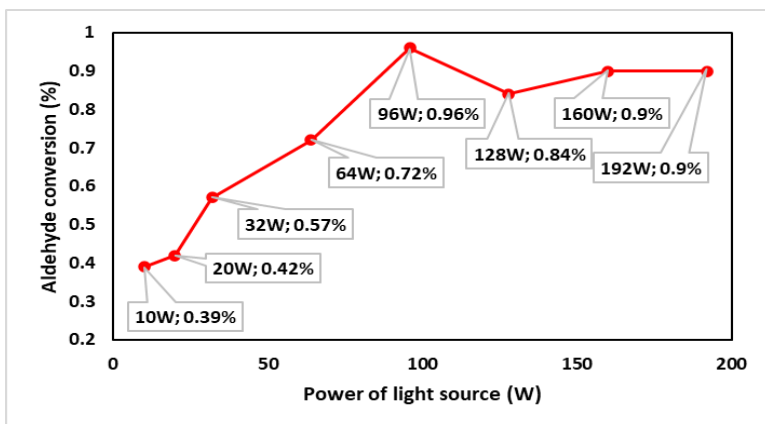


Figure 1. Effect of light intensity on benzaldehyde yield under red LED lamp (640 nm) with 15 min. light irradiation

The findings from the evaluation of photooxidative transformations provide reaction yields and an understanding of fundamental photochemical processes. The conversion of benzyl alcohol to benzaldehyde is a widely used model reaction in selective oxidation processes. This reaction is highly sensitive to the type of oxidant, light wavelength, and solvent environment used. Thus, the presented data reveal experimental observations and the fundamental dynamics of the photooxidation mechanism. Previous studies have generally been conducted in the presence of heterogeneous or homogeneous photocatalysts, emphasizing the catalyst's accelerating effect. However, this study preferred catalyst-free conditions. This permits the pure photochemical behavior of the system to be examined without masking the catalyst's effect. Catalyst-free experiments reveal the interaction between oxidant activation and photon energy, determining whether the reaction is photoinduced. Thus, the results obtained contribute to a more accurate interpretation of light-oxidant-environment interactions when designing future catalyzed systems. Another important aspect of the catalyst-free study is measuring the system's spontaneous photooxidative conversion capacity. This approach establishes reference values for photocatalytic mechanisms and provides a "blank test" standard for evaluating whether increases in catalyst-based systems represent real performance improvements. This comparative perspective, particularly in frequently used model reactions such as the oxidation of benzyl alcohol, enables a more reliable evaluation of the effectiveness of reported catalysts.

Overall, the experimental findings showed that benzyl alcohol photooxidation can occur efficiently without a catalyst, particularly under high-energy blue light and with the TBHP oxidant. A comparison of oxidant types revealed that TBHP was the most selective and efficient, while H_2O_2 exhibited limited activity and m-CPBA resulted in byproduct formation with

low conversion. Studies on the effect of solvents revealed that the polarity and oxygen solubility of the medium directly affect the course of the reaction. Toluene provided the highest efficiency, but showed low selectivity. Media such as DMF virtually suppressed the reaction.

Light intensity and wavelength tests demonstrated that the system is sensitive to high-energy photons and that efficient photooxidation occurs under blue light. Red light alone was insufficient to initiate conversion but contributed partially in combination. These observations demonstrate that light intensity and photon energy are both determining factors in photooxidation processes. In conclusion, this study reveals the fundamental mechanism of uncatalyzed photooxidation and provides a basis for the future development of catalyzed systems. The obtained data demonstrate that highly efficient and selective oxidation processes can be designed through the selection of appropriate oxidants, the optimization of solvents, and the adjustment of light conditions. This advances our understanding of the fundamental mechanism and sheds light on new strategies for photocatalytic transformations.

REFERENCE

- Chen, X., Li, C., Grätzel, M., Kostecki, R., ve Mao, S. S. (2012). Nanomaterials for renewable energy production and storage. *Chemical Society Reviews*, 41(23), 7909–7937. <https://doi.org/10.1039/C2CS35230C>
- Fujishima, A., Honda, K. (1972). Electrochemical photolysis of water at a semiconductor electrode. *Nature*, 238, 37–38. <https://doi.org/10.1038/238037a0>
- Gök, Y., Donmez, S., Erdem, R., ve Gök, H. Z. (2025). Green photooxidation of 1-naphthol using a zinc phthalocyanine-loaded MCM-41 heterogeneous catalyst. *ChemPlusChem*, 90(8), e202500207 <https://doi.org/10.1002/cplu.202500207>
- Gök, Y., Erdem, R., ve Gök, H. Z. (2026). Photocatalytic selective oxidation of 1-naphthol under red light using SBA-15-supported zinc phthalocyanine. *Journal of Photochemistry and Photobiology A: Chemistry*, 470, 116640. <https://doi.org/10.1016/j.jphotochem.2025.116640>
- Gök, Y., Arlı, O., Gök, H., & Erdem, R. (2024). Preparation of Mesoporous silica Nanostructure Functionalized with Hydrobenzoin substituted phthalocyanine and its catalytic performance in benzyl alcohol oxidation. *Applied Organometallic Chemistry*, 39(3), e7925. <https://doi.org/10.1002/aoc.7925>
- Gök, H. Z., Erdem, R., Gök, Y. (2025). Selective oxidation of benzylic alcohols to aldehydes by C-symmetric diol substituted Cobalt phthalocyanine-mesoporous silica nanostructure. *Inorganic Chemistry Communications*, 174(1), 113961. <https://doi.org/10.1016/j.inoche.2025.113961>

Mallat, T., Baiker, A. (2004). Oxidation of alcohols with molecular oxygen on solid catalysts. *Chemical Reviews*, 104(6), 3037–3058. <https://doi.org/10.1021/cr0200116>

Mamba, G., Mishra, A. K. (2016). Graphitic carbon nitride (g-C₃N₄) nanocomposites: A new and exciting generation of visible light driven photocatalysts for environmental pollution remediation. *Applied Catalysis B: Environmental*, 198, 347–377. <https://doi.org/10.1016/j.apcatb.2016.05.052>

Parrino, F., Bellardita, M., García-López, E. I., Marci, G., Loddo, V., Palmisano L. (2018). Heterogeneous photocatalysis for selective formation of high-value-added molecules: Some chemical and engineering aspects. *ACS Catalysis*, 8(12), 11191–11225. <https://doi.org/10.1021/acscatal.8b03093>

Sheldon, R. A. (2016). Green chemistry and resource efficiency: Towards a green economy. *Green Chemistry*, 18(11), 3180–3183. <https://doi.org/10.1039/C6GC90040B>

Xianjiang, L., Ma, W., Li, H., Zhang, Q., Liu, H. (2020). Sulfur-functionalized metal-organic frameworks: Synthesis and applications as advanced adsorbents. *Coordination Chemistry Reviews*, 408, 213191. <https://doi.org/10.1016/j.ccr.2020.213191>

On Non-Newtonian Closed Metric Intervals

Ahmadou DIALLO¹

Birsen SAĞIR²

- 1- Master's Student, Graduate Education Institute, Department of Mathematics, Ondokuz Mayıs University, ahmaddjalloh@gmail.com ORCID No: 0009-0004-7403-7903
- 2- Prof. Dr, Department of Mathematics, Onndokuz Mayıs University 55139, bduyar@omu.edu.tr ORCID iD: 0000-0001-5954-2005.

ABSTRACT

Fréchet (1906) and Hausdorff (1914) developed the idea of a metric space, which has been essential to developing geometric and analytical concepts. Menger expanded this framework in 1928 by proposing the idea of a point that is "between" two other points, which is technically defined by the equivalence $d(a, c) = d(a, b) + d(b, c)$. Later advancements, such as Mud's (2019) formalization of monotonicity in metric spaces, made additional expansions possible.

The idea of monotone sequences is expanded in this work to the context of non-Newtonian calculus produced by a bijective generator function \mathfrak{x} . Beginning with Grossman and Katz (1972–1983), non-Newtonian analysis substitutes \mathfrak{x} -arithmetic and \mathfrak{x} -metrics for classical arithmetic and metric notions, enabling the adaptation of basic ideas like distance, convergence, and completeness. In this framework, we define \mathfrak{x} -monotonicity using Menger's "between" relation's \mathfrak{x} -metric analogue.

We demonstrate various important theorems provided in \mathfrak{x} -metric spaces such as \mathfrak{x} -real, \mathfrak{x} -taxicab, and \mathfrak{x} -Euclidean spaces, showing how the \mathfrak{x}^{-1} transformation preserves classical behaviors while revealing truly new structural features.

By bridging the gap between non-Newtonian analysis and classical metric space theory, this work demonstrates how the generalized concept of monotonicity enhances the analytical toolkit available for examining sequences in wider mathematical contexts while also retaining much of the intuitive geometric interpretation.

Keywords – Non-Newtonian calculus, \mathfrak{x} -metric, \mathfrak{x} -monotonicity.

INTRODUCTION

The notion of *écart* (or semi-metric) was first proposed by Maurice Fréchet in 1906, and Felix Hausdorff officially used the phrase "metric space" in 1914. Metric spaces were introduced to geometry by Karl Menger shortly after. He discussed points that lie between two given points in his 1928 work *Untersuchungen über allgemeine Metrik*, among other things. Based on their original sources (R.N. Mud 2019; Cristinel 2025), these ideas are synthesized in the section that follows.

Definition 1.1: Assume E is a non-empty set. A real-valued function f defined on $E \rightarrow (0, \infty)$ is called a metric on E if it satisfies the following criteria:

$$(M1) \quad d(t, s) = 0 \Leftrightarrow s = t$$

$$(M2) \quad d(t, s) = d(s, t)$$

$$(M3) \quad d(t, s) \leq d(t, z) + d(z, s)$$

for any $t, s, z \in E$. E is commonly represented by (E, d) and is referred to as the metric space.

The triangle inequality is the name given to the third property.

In general, spaces with an ordering relation " \leq " are used to define monotonicity.

For all $n \in \mathbb{N}$, we say that a sequence of real numbers is increasing if $a_n \leq a_{n+1}$ and decreasing if $a_n \geq a_{n+1}$. If a sequence is either increasing or decreasing, it is considered monotone.

Menger (1928:100) developed the concept of points that are between two points, introducing an ordering relation even though there isn't one in a general metric space. More specifically, if

$$d(a, b) = d(a, t) + d(t, b),$$

then t is between a and b if points $a, b, t \in (E, d)$.

Mud (2019) defined a type of monotonicity with regard to a fixed element selected in the corresponding metric space. In this work, we will present the idea of monotone sequences in metric spaces, which do not contain elements that are not part of the specified sequence.

We shall begin with the example of the metric space of the real numbers, as is customary. In this regard, note that for any positive integer $m \leq n \leq p$, we have $t_m \leq t_n \leq t_p$, and thus

$$|t_m - t_n| + |t_n - t_p| = |t_m - t_p| \quad (1)$$

Additionally, this equivalence applies to any decreasing sequence (t_n) .

(1) can be rewritten in terms of distance d if we take into consideration the (usual) metric space (\mathbb{R}, d) with $d(t, s) = |t - s|$.

We are entitled to introduce the following because of this fact:

Definition 1.2 Let $E \neq \emptyset$ and (E, d) be a metric space. A sequence (t_n) is considered monotone if, for any positive integer $m \leq n \leq p$, we obtain:

$$d(t_m, t_n) + d(t_n, t_p) = d(t_m, t_p) \quad (2)$$

In the sequel, we will describe monotone sequences in a few classical metric spaces.

With $d(t, s) = |t - s|$ in the (normal) metric space (\mathbb{R}, d) , relation (2) takes the following form:

$$|t_m - t_n| + |t_n - t_p| = |t_m - t_p|,$$

where $1 \leq m \leq n \leq p$.

In summary, the monotonicity provided by Definition 1.1 is equivalent to the monotonicity with regard to the natural ordering on \mathbb{R} in the (usual) metric space (\mathbb{R}, d) .

The k -dimensional real space $\mathbb{R}^k = \{t | t = (t_1, \dots, t_k), t_1 \in \mathbb{R}, \dots, t_k \in \mathbb{R}\}$ equipped with the so-called Taxicab metric is examined here:

$$d(t, s) = \sum_{i=1}^k |t_i - s_i|$$

for each $t, s \in \mathbb{R}^k, t = (t_1, \dots, t_k), s = (s_1, \dots, s_k)$

Theorem 1.3 According to Definition 1.1, a sequence $(t_n)_{n \geq 1}, t_n = (t_n^1, \dots, t_n^k)$, of elements from the k -dimensional Taxicab metric space is monotone if and only if every real sequence $(t_n^1)_{n \geq 1}, (t_n^2)_{n \geq 1}, \dots, (t_n^k)_{n \geq 1}$ is monotone in the conventional sense (possibly of different monotonicity).

Let us consider the k -dimensional real space $\mathbb{R}^k = \{t | t = (t_1, \dots, t_k), t_1 \in \mathbb{R}, \dots, t_k \in \mathbb{R}\}$ endowed with the Euclidian metric:

$$d(t, s) = \sqrt{\sum_{i=1}^k (t_i - s_i)^2} \quad (3)$$

for each $t, s \in \mathbb{R}^k, t = (t_1, \dots, t_k), s = (s_1, \dots, s_k)$.

Theorem 1.4 A sequence $(t_n)_{n \geq 1}, t_n = (t_n^1, \dots, t_n^k)$, of elements from the k -dimensional Euclidian metric space is monotone in the sense of Definition 1.1 if and only if there exists a monotone sequence $(\lambda_n)_{n \geq 1}$, such that, for every integer $n \geq 1$, it holds:

$$t_n = \lambda_n(x_2, \dots, x_1).$$

Maurice Fréchet first proposed the idea of ecart (semi-metric) in 1906, while Felix Hausdorff first used the word metric space in 1914. The introduction of metric spaces in geometry by Karl Menger followed shortly after. The formula $d(a, b) = d(a, t) + d(t, b)$ indicates that a point t is between a and b . The collection of all these points is now referred to as a Closed Metric Interval (Deza, M. M. and Deza E. 2009).

Next, the notion of closed metric intervals, denoted $[a, b]_d$, is introduced in a metric space (X, d) as:

$$[a, b]_E^d := \{t \in X \mid d(a, t) + d(t, b) = d(a, b)\} \quad (4)$$

The sub- and superscripts clarify the metric space, defining the set as $[a, b]_{\mathbb{R}}^d$. This is the closed interval of real numbers between a and b . Closed metric intervals prove the Monotone Convergence Theorem in metric spaces, resembling line segments but with less well-behaved behavior.

Lemma 1.5 $t \in [a, b]$ if and only if $[a, t] \subseteq [a, b]$

This lemma confirms that the set $[a, b]$ is built in a nested fashion from subintervals $[a, t]$. Furthermore, it is established that $[a, b] = [b, a]$ meaning the metric interval is symmetric.

However, the stronger claim that $t, s \in [a, b]$ implies $[t, s] \subseteq [a, b]$ does not always hold. A counterexample using nodes and shortest-path distances demonstrates this.

Lemma 1.7 For $t, s \in [a, b]$,

$$t \in [a, y] \text{ if and only if } s \in [t, b].$$

This lemma reinforces the symmetric structure of closed metric intervals and provides a key identity for defining generalized monotonicity.

Theorem 1.8 The set $[a, b]$ is closed in any metric space. This foundational result ensures that convergence and continuity arguments using these intervals are well-supported within general metric space theory.

Newton and Leibniz established differential and integral calculus, leading to the development of Newtonian calculus. Grossman and Katz's 1972-1983 studies introduced non-Newtonian analysis, introducing fundamental definitions and concepts in classical analysis. Numerous analyses, such as geometric, harmonic, and quadratic analysis, have been developed by various researchers. Grossman J. studied the properties of derivatives and integrals. Duyar, Sağır, and Oğur discovered fundamental topological characteristics of the non-Newtonian real line, and Sağır and Duyar obtained results on Lebesgue measure in non-Newtonian calculus.

Building on these studies, especially (Çakmak and Başar, 2012:228; Grossman and Katz, 1972; Grossman, 1979; Değirmen and Duyar, 2023:9561–9574; Duyar and Erdoğan, 2016:34–48; Duyar and Oğur, 2017:11–14; Güngör, 2022:373–387; Güngör and Dinç, 2024:130–145; İ. Eryılmaz, 2024:1–23; Sager and Sağır, 2021:2231–2243; Rohman, M., and Eryılmaz, I, 2023-1:8), we present the relevant definitions and theorems and provide a brief overview of non-Newtonian calculus.

The relations of a field with a compatible total order on a certain subset of the set of real numbers are indicated by arithmetic. The addition and multiplication operations, as well as the order relation of this ordered field, can be defined using definitions other than the conventional ones. These definitions are the outcome of a particular transformation that yields a fundamental subset of real numbers required for mathematical operations. A generator function is the name given to such a transformation. \varkappa -arithmetic is a specific non-Newtonian technique that uses generator functions.

The set $\{\varkappa(o): o \in \mathbb{R}\}$ is referred to as the set of real numbers in a non-Newtonian context, denoting it by \mathbb{R}_\varkappa . The basic operations on \mathbb{R}_\varkappa are introduced as follows:

$$\begin{array}{ll} \varkappa\text{-addition} & \dot{o} \dot{+} \dot{j} = \varkappa\{\varkappa^{-1}(\dot{o}) + \varkappa^{-1}(\dot{j})\} \\ \varkappa\text{-subtraction} & \dot{o} \dot{-} \dot{j} = \varkappa\{\varkappa^{-1}(\dot{o}) - \varkappa^{-1}(\dot{j})\} \\ \varkappa\text{-multiplication} & \dot{o} \dot{\times} \dot{j} = \varkappa\{\varkappa^{-1}(\dot{o}) \times \varkappa^{-1}(\dot{j})\} \\ \varkappa\text{-division} & \dot{o} \dot{/} \dot{j} = \varkappa\{\varkappa^{-1}(\dot{o}) / \varkappa^{-1}(\dot{j})\}, \dot{j} \neq \dot{0} \\ \varkappa\text{-order} & \dot{o} \dot{<} \dot{j} \Leftrightarrow \varkappa^{-1}(\dot{o}) < \varkappa^{-1}(\dot{j}) \end{array}$$

for $\dot{o}, \dot{j} \in \mathbb{R}_\varkappa$.

The number \varkappa -zero is represented by $\dot{0} = \varkappa(0)$ and the \varkappa -unit is represented as $\dot{1} = \varkappa(1)$. The usual notation for \varkappa -integers is as follows:

$$\dots \varkappa(-2), \varkappa(-1), \varkappa(0), \varkappa(1), \varkappa(2), \dots$$

\varkappa -positive numbers are those that meet the criterion $\dot{0} \dot{<} \dot{o}$, and \varkappa -negative numbers are those that meet the condition $\dot{o} \dot{<} \dot{0}$. Therefore, each number n is represented by $\dot{n} = \varkappa(n)$ in accordance with \varkappa -arithmetic.

If \dot{n} is a positive \varkappa -integer, it can be expressed as the \varkappa -sum of $\dot{1}$ repeated n times:

$$\dot{n} = \underbrace{\dot{1} \dot{+} \dots \dot{+} \dot{1}}_{n\text{-times}}.$$

\mathbb{R}_\varkappa^+ and \mathbb{R}_\varkappa^- stand for the sets of non-Newtonian positive and negative real numbers, respectively.

The system $(\mathbb{R}_\varkappa, \dot{+}, \dot{\times}, \dot{<})$ forms a totally ordered field.

The \varkappa -square of $o \in \mathbb{R}_\varkappa$ is the square of a number represented by o^{2_\varkappa} , which is defined as follows:

$$o^{2_\varkappa} = o \dot{\times} o$$

The \mathfrak{x} -nonnegative number whose \mathfrak{x} -square equals:

$$\mathfrak{d}^{2\mathfrak{x}} = \Leftrightarrow \mathfrak{d} = \sqrt{\mathfrak{d}}^{\mathfrak{x}} = \mathfrak{x}\left\{\sqrt{\mathfrak{x}^{-1}(\mathfrak{d})}\right\}$$

is the \mathfrak{x} -square root of a number $\mathfrak{d} \in \mathbb{R}_{\mathfrak{x}}^+$ represented by $\sqrt{\mathfrak{d}}^{\mathfrak{x}}$.

$\mathfrak{d}^{p_{\mathfrak{x}}}$ and $\sqrt[p]{\mathfrak{d}}^{\mathfrak{x}}$, respectively, are the representations of the p th non-Newtonian exponent and the q th non-Newtonian root of a number $\mathfrak{d} \in \mathbb{R}_{\mathfrak{x}}$. They are defined as follows:

$$\begin{aligned}\mathfrak{d}^{2\mathfrak{x}} &= \mathfrak{d} \times \mathfrak{d} = \mathfrak{x}\{\mathfrak{x}^{-1}(\mathfrak{d}) \times \mathfrak{x}^{-1}(\mathfrak{d})\} = \mathfrak{x}\{[\mathfrak{x}^{-1}(\mathfrak{d})]^2\} \\ \mathfrak{d}^{3\mathfrak{x}} &= \mathfrak{d}^{2\mathfrak{x}} \times \mathfrak{d} = \mathfrak{x}\{\mathfrak{x}\{\mathfrak{x}[\mathfrak{x}^{-1}(\mathfrak{d}) \times \mathfrak{x}^{-1}(\mathfrak{d})]\} \times \mathfrak{x}^{-1}(\mathfrak{d})\} = \mathfrak{x}\{[\mathfrak{x}^{-1}(\mathfrak{d})]^3\} \\ &\vdots \\ \mathfrak{d}^{p_{\mathfrak{x}}} &= \mathfrak{d}^{(p-1)\mathfrak{x}} \times \mathfrak{d} = \mathfrak{x}\{[\mathfrak{x}^{-1}(\mathfrak{d})]^p\} \\ &\vdots\end{aligned}$$

The \mathfrak{x} -absolute value function $|\cdot|_{\mathfrak{x}}: \mathbb{R}_{\mathfrak{x}} \rightarrow \mathbb{R}_{\mathfrak{x}}^{+,0}$ is defined by:

$$|\mathfrak{d}|_{\mathfrak{x}} = \begin{cases} \mathfrak{d}, & \mathfrak{d} \succ \dot{0} \text{ or } \mathfrak{d} = \dot{0} \\ \dot{0} \dot{-} \mathfrak{d}, & \mathfrak{d} \prec \dot{0} \end{cases}$$

where $\mathbb{R}_{\mathfrak{x}}^{+,0} = \mathbb{R}_{\mathfrak{x}}^+ \cup \{\dot{0}\}$

Hence, for $\mathfrak{d} \in \mathbb{R}_{\mathfrak{x}}$ we get:

$$\sqrt{\mathfrak{d}^{2\mathfrak{x}}}^{\mathfrak{x}} = |\mathfrak{d}|_{\mathfrak{x}} = \mathfrak{x}(|\mathfrak{x}^{-1}(\mathfrak{d})|)$$

The non-Newtonian distance between the points $\mathfrak{d}_1, \mathfrak{d}_2 \in \mathbb{R}_{\mathfrak{x}}$ is given by

$$|\mathfrak{d}_1 \dot{-} \mathfrak{d}_2|_{\mathfrak{x}}.$$

The characteristics of the \mathfrak{x} -absolute value with $\mathfrak{d}, \mathfrak{z} \in \mathbb{R}_{\mathfrak{x}}$ are as follows:

- (I) $|\mathfrak{d} \times \mathfrak{z}|_{\mathfrak{x}} = |\mathfrak{d}|_{\mathfrak{x}} \times |\mathfrak{z}|_{\mathfrak{x}}$
- (II) $|\mathfrak{d} \dot{+} \mathfrak{z}|_{\mathfrak{x}} \leq |\mathfrak{d}|_{\mathfrak{x}} \dot{+} |\mathfrak{z}|_{\mathfrak{x}}$
- (III) $||\mathfrak{d}|_{\mathfrak{x}} \dot{-} |\mathfrak{z}|_{\mathfrak{x}}|_{\mathfrak{x}} \leq |\mathfrak{d} \dot{-} \mathfrak{z}|_{\mathfrak{x}}$

Let $\mathfrak{d}, \mathfrak{z} \in \mathbb{R}_{\mathfrak{x}}$. Then

$$\frac{|\mathfrak{d} \dot{+} \mathfrak{z}|_{\mathfrak{x}}}{\mathfrak{x}(1) \dot{+} |\mathfrak{d} \dot{+} \mathfrak{z}|_{\mathfrak{x}}} \mathfrak{x} \leq \frac{|\mathfrak{d}|_{\mathfrak{x}}}{\mathfrak{x}(1) \dot{+} |\mathfrak{d}|_{\mathfrak{x}}} \mathfrak{x} \dot{+} \frac{|\mathfrak{z}|_{\mathfrak{x}}}{\mathfrak{x}(1) \dot{+} |\mathfrak{z}|_{\mathfrak{x}}} \mathfrak{x}$$

Theorem 1.9 (\mathfrak{x} -Minkowski inequality) Let $p > 1$ and $\mathfrak{d}_k, \mathfrak{z}_k \in \mathbb{R}_{\mathfrak{x}}^+$ for $k \in \{1, 2, \dots, n\}$. Then

$$\sqrt[p]{\sum_{k=1}^n (\mathfrak{d}_k \dot{+} \mathfrak{z}_k)^{p_{\mathfrak{x}}}}^{\mathfrak{x}} \leq \sqrt[p]{\sum_{k=1}^n \mathfrak{d}_k^{p_{\mathfrak{x}}}}^{\mathfrak{x}} \dot{+} \sqrt[p]{\sum_{k=1}^n \mathfrak{z}_k^{p_{\mathfrak{x}}}}^{\mathfrak{x}} \quad (5)$$

Definition 1.10 Let E be a set that isn't empty. If a non-Newtonian real-valued function $d_{\mathfrak{x}}$ defined on $X \times X$ meet the following criteria, it is referred to as a \mathfrak{x} -metric on E :

$$(\mathfrak{x}\text{-M1}) \quad d_{\mathfrak{x}}(\dot{\mathfrak{o}}, \dot{\mathfrak{j}}) = \dot{0} \Leftrightarrow \dot{\mathfrak{o}} = \dot{\mathfrak{j}}$$

$$(\mathfrak{x}\text{-M2}) \quad d_{\mathfrak{x}}(\dot{\mathfrak{o}}, \dot{\mathfrak{j}}) = d_{\mathfrak{x}}(\dot{\mathfrak{j}}, \dot{\mathfrak{o}})$$

$$(\mathfrak{x}\text{-M3}) \quad d_{\mathfrak{x}}(\dot{\mathfrak{o}}, \dot{\mathfrak{j}}) \leq d_{\mathfrak{x}}(\dot{\mathfrak{o}}, \dot{\mathfrak{w}}) \dot{+} d_{\mathfrak{x}}(\dot{\mathfrak{w}}, \dot{\mathfrak{j}})$$

for any $\dot{\mathfrak{o}}, \dot{\mathfrak{j}}, \dot{\mathfrak{w}} \in E$. E is commonly represented by $(E, d_{\mathfrak{x}})$ and is referred to as the non-Newtonian metric (\mathfrak{x} -metric) space.

Corollary 1.11 All ordered n -tuples of \mathfrak{x} -real numbers consist of an n -dimensional \mathfrak{x} -Euclidian space $\mathbb{R}_{\mathfrak{x}}^n$, is a \mathfrak{x} -metric space with the metric $d_{\mathfrak{x}}$ defined in $\mathbb{R}_{\mathfrak{x}} \times \mathbb{R}_{\mathfrak{x}} \rightarrow \mathbb{R}_{\mathfrak{x}}$ by

$$d_{\mathfrak{x}}(\dot{\mathfrak{o}}, \dot{\mathfrak{j}}) = \sqrt{\sum_{k=1}^n (\dot{\mathfrak{o}}_k \dot{-} \dot{\mathfrak{j}}_k)^{2_{\mathfrak{x}}}} = \mathfrak{x} \left\{ \sqrt{\sum_{k=1}^n [\mathfrak{x}^{-1}(\dot{\mathfrak{o}}_k) - \mathfrak{x}^{-1}(\dot{\mathfrak{j}}_k)]^2} \right\} \quad (6)$$

where $\dot{\mathfrak{o}} = (\dot{\mathfrak{o}}_1, \dot{\mathfrak{o}}_2, \dots, \dot{\mathfrak{o}}_n)$, $\dot{\mathfrak{j}} = (\dot{\mathfrak{j}}_1, \dot{\mathfrak{j}}_2, \dots, \dot{\mathfrak{j}}_n) \in \mathbb{R}_{\mathfrak{x}}^n$

Definition 1.12 Let $\mathbb{R}_{\mathfrak{x}}$ be the set of non-Newtonian real numbers. The function $\mathfrak{w}: \mathbb{N} \rightarrow \mathbb{R}_{\mathfrak{x}}$ is called the non-Newtonian sequence (\mathfrak{x} -sequence) of real numbers. For $n \in \mathbb{N}$, a \mathfrak{x} -sequence is denoted by one of its symbols $\{\mathfrak{w}_n\}_{n=1}^{\infty}$, $\{\mathfrak{w}_n\}_{n \geq 1}$, (\mathfrak{w}_n) .

Definition 1.13 (\mathfrak{x} -convergent sequence and \mathfrak{x} -Cauchy sequence): Let a sequence (\mathfrak{w}_n) and $\dot{\mathfrak{o}} \in E$ be given in the non-Newtonian metric space $(E, d_{\mathfrak{x}})$.

If for any given $\dot{\varepsilon} > \dot{0}$ there exists an $n_0 = n_0(\dot{\varepsilon}) \in \mathbb{N}$ such that $d_{\mathfrak{x}}(\mathfrak{w}_n, \dot{\mathfrak{o}}) < \dot{\varepsilon}$ for all $n \geq n_0$, then the \mathfrak{x} -sequence (\mathfrak{w}_n) is said to be \mathfrak{x} -convergent in E and is denoted by

$$\mathfrak{x} \lim_{n \rightarrow \infty} \mathfrak{w}_n = \dot{\mathfrak{o}} \text{ or } \mathfrak{w}_n \xrightarrow{d_{\mathfrak{x}}} \dot{\mathfrak{o}} \text{ as } n \rightarrow \infty$$

If for every given $\dot{\varepsilon} > \dot{0}$, one $n_0 = n_0(\dot{\varepsilon}) \in \mathbb{N}$ can be found such that $d_{\mathfrak{x}}(\mathfrak{w}_n, \mathfrak{w}_m) < \dot{\varepsilon}$ for all $m, n \geq n_0$, then the sequence (\mathfrak{w}_n) is called a non-Newtonian Cauchy sequence (\mathfrak{x} -Cauchy sequence) in \mathfrak{x} -metric space $(X, d_{\mathfrak{x}})$.

A metric space $(X, d_{\mathfrak{x}})$ is \mathfrak{x} -complete if every \mathfrak{x} -Cauchy sequence (\mathfrak{w}_n) in X converges.

RESULTS AND DISCUSSION

The definition of closed metric intervals in the context of non-Newtonian analysis is presented in this work, along with some findings.

Definition 2.1 For all $n \in \mathbb{N}$, we say that a sequence of \mathfrak{r} real numbers $(a_n)_{n \in \mathbb{N}}$ is increasing if $a_n \leq a_{n+1}$ and decreasing if $a_n \geq a_{n+1}$. If a \mathfrak{r} -sequence is either increasing or decreasing, it is considered \mathfrak{r} -monotone.

Next, the notion of closed metric intervals, denoted $[a, b]_{d_{\mathfrak{r}}}$, is introduced in a metric space $(E, d_{\mathfrak{r}})$ as:

$$[a, b]_E^{d_{\mathfrak{r}}} := \{t \in X \mid d_{\mathfrak{r}}(a, t) \dot{+} d_{\mathfrak{r}}(t, b) = d_{\mathfrak{r}}(a, b)\}$$

Subscripts and superscripts are used to avoid any ambiguity regarding the metric space in which the set is defined. When the context makes the metric space clear, we will simply write $[a, b]$. It can be verified that $[a, b]_{\mathbb{R}_{\mathfrak{r}}}^{d_{\mathfrak{r}}}$, as defined above, corresponds exactly to the closed interval of \mathfrak{r} -real numbers between a and b , which explains the choice of this notation. In the following, however, the metric space considered will be non-Newtonian, and all intervals and constructions are understood in that context.

Lemma 2.2

$$t \in [a, b]_E^{d_{\mathfrak{r}}} \text{ if and only if } [a, t]_E^{d_{\mathfrak{r}}} \subseteq [a, b]_E^{d_{\mathfrak{r}}}$$

Proof: If $[a; t] \subseteq [a, b]$, then $t \in [a, t]$ trivially, so $t \in [a, b]$.

Conversely, suppose $t \in [a, b]$. Then for all $s \in [a; t]$,

$$\begin{aligned} d_{\mathfrak{r}}(a, b) &= d_{\mathfrak{r}}(a, t) \dot{+} d_{\mathfrak{r}}(t, b) \\ &= d_{\mathfrak{r}}(a, s) \dot{+} d_{\mathfrak{r}}(s, t) \dot{+} d_{\mathfrak{r}}(t, b) \\ &\geq d_{\mathfrak{r}}(a, s) \dot{+} d_{\mathfrak{r}}(s, b) \\ &\geq d_{\mathfrak{r}}(a, b). \end{aligned}$$

So equality must hold, meaning $s \in [a; b]$. Thus, $[a; t] \subseteq [a, b]$

This lemma confirms that the set $[a, b]$ is built in a nested fashion from subintervals $[a, t]$. Furthermore, it is established that $[a, b] = [b, a]$ meaning the metric interval is symmetric.

However, the stronger claim that $t, s \in [a, b]$ implies $[t, s] \subseteq [a, b]$ does not always hold. A counterexample using nodes and shortest-path distances demonstrates this.

Lemma 2.3

For $t, s \in [a, b]$,

$$t \in [a, s] \text{ if and only if } s \in [t, b].$$

Proof: $t, s \in [a, s] \Leftrightarrow d_{\mathfrak{r}}(a, t) \dot{+} d_{\mathfrak{r}}(t, s) = d_{\mathfrak{r}}(a, s)$

$$\Leftrightarrow d_{\mathfrak{r}}(a, t) \dot{+} d_{\mathfrak{r}}(t, s) \dot{+} d_{\mathfrak{r}}(s, b) = d_{\mathfrak{r}}(a, s) \dot{+} d_{\mathfrak{r}}(s, b)$$

$$\Leftrightarrow d_{\mathfrak{r}}(a, t) \dot{+} d_{\mathfrak{r}}(t, s) \dot{+} d_{\mathfrak{r}}(s, b) = d_{\mathfrak{r}}(a, s)$$

$$\Leftrightarrow d_{\mathfrak{r}}(t, s) \dot{+} d_{\mathfrak{r}}(s, b) = d_{\mathfrak{r}}(t, b)$$

$$\Leftrightarrow s \in [t, b].$$

This lemma reinforces the symmetric structure of closed metric intervals and provides a key identity for defining generalized monotonicity.

Definition 2.4 Let $E \neq \emptyset$ and $(E, d_{\mathfrak{r}})$ be a metric space. A sequence (t_n) is considered monotone if, for any positive integer $m \leq n \leq p$, we obtain:

$$d_{\mathfrak{r}}(t_m, t_n) \dot{+} d_{\mathfrak{r}}(t_n, t_p) = d_{\mathfrak{r}}(t_m, t_p) \quad (7)$$

In the sequel, we will describe monotone sequences in a few classical metric spaces.

With $d_{\mathfrak{r}}(t, s) = |t - s|_{\mathfrak{r}}$ in the (normal) metric space $(\mathbb{R}_{\mathfrak{r}}, d_{\mathfrak{r}})$, relation (7) takes the following form:

$$|t_m \dot{-} t_n|_{\mathfrak{r}} \dot{+} |t_n \dot{-} t_p|_{\mathfrak{r}} = |t_m \dot{-} t_p|_{\mathfrak{r}},$$

where $1 \leq m \leq n \leq p$.

In summary, the monotonicity provided by Definition 1.1 is equivalent to the monotonicity with regard to the natural ordering on $\mathbb{R}_{\mathfrak{r}}$ in the (usual) \mathfrak{r} -metric space $(\mathbb{R}_{\mathfrak{r}}, d_{\mathfrak{r}})$.

The k -dimensional real space $\mathbb{R}_{\mathfrak{r}}^k = \{t | t = (t_1, \dots, t_k), t_1 \in \mathbb{R}_{\mathfrak{r}}, \dots, t_k \in \mathbb{R}_{\mathfrak{r}}\}$ equipped with the so-called \mathfrak{r} -Taxicab metric is examined here:

$$d_{\mathfrak{r}}(t, s) = \sum_{\mathfrak{r} k=1}^k |t_i \dot{-} s_i|_{\mathfrak{r}}$$

for each $t, s \in \mathbb{R}_{\mathfrak{r}}^k, t = (t_1, \dots, t_k), s = (s_1, \dots, s_k)$

This work provided the foundation for obtaining the results of Theorems 1.3 and 1.4 in the non-Newtonian sense.

Theorem 2.5 According to Definition 1.1, a \mathfrak{x} -sequence $(t_n)_{n \geq 1}$, $t_n = (t_n^1, \dots, t_n^k)$, of elements from the k -dimensional \mathfrak{x} -Taxicab metric space is \mathfrak{x} -monotone if and only if every \mathfrak{x} -real sequence $(t_n^1)_{n \geq 1}$, $(t_n^2)_{n \geq 1}$, ..., $(t_n^k)_{n \geq 1}$ is monotone in the conventional sense (possibly of different monotonicity).

Let us consider the k -dimensional \mathfrak{x} -real space $\mathbb{R}_\mathfrak{x}^k = \{t | t = (t_1, \dots, t_k), t_1 \in \mathbb{R}_\mathfrak{x}, \dots, t_k \in \mathbb{R}_\mathfrak{x}\}$ endowed with the Euclidian metric:

$$d_\mathfrak{x}(t, s) = \sqrt[\mathfrak{x}]{\sum_{i=1}^k (t_i \dot{-} s_i)^{2\mathfrak{x}}}$$

for each $x, y \in \mathbb{R}_\mathfrak{x}^k$, $x = (x_1, \dots, x_k)$, $y = (y_1, \dots, y_k)$.

Theorem 2.6 A sequence $(t_n)_{n \geq 1}$, $t_n = (t_n^1, \dots, t_n^k)$, of elements from the k -dimensional \mathfrak{x} -Euclidian metric space is \mathfrak{x} -monotone in the sense of Definition 1.1 if and only if there exists a \mathfrak{x} -monotone sequence $(\lambda_n)_{n \geq 1}$, such that, for every integer $n \geq 1$, it holds:

$$t_n = \lambda_n(t_2 \dot{-} t_1) \dot{+} t_2$$

Theorem 2.7 Every \mathfrak{x} -monotone and \mathfrak{x} -bounded sequence

$$(t_n)_{n \geq 1} \subset (E, d)$$

is a \mathfrak{x} -Cauchy sequence.

Proof: Suppose that

$$M = \sup_{n \geq 1} d_\mathfrak{x}(t_1, t_n).$$

For all $\varepsilon > 0$, there exists $k \geq 1$ such that $d_\mathfrak{x}(t_1, t_k) \dot{>} M \dot{-} \varepsilon$. Then for all $m, n \geq k$, we have:

$$d_\mathfrak{x}(t_m, t_n) \dot{<} \varepsilon,$$

indicating that $(t_n)_{n \geq 1}$ is a Cauchy sequence. Here's how this may be demonstrated.

Assume that $m \leq n$ without losing generality.

$$d_\mathfrak{x}(t_1, t_m) = d_\mathfrak{x}(t_1, t_k) \dot{+} d_\mathfrak{x}(t_k, t_m) \dot{\geq} d_\mathfrak{x}(t_1, t_k) \dot{>} M \dot{-} \varepsilon$$

so $d_\mathfrak{x}(t_1, t_k) \dot{>} M \dot{-} \varepsilon$. If we use $d_\mathfrak{x}(t_n, t_1) \dot{\leq} M$, we can deduce

$$d_\mathfrak{x}(t_m, t_1) = d_\mathfrak{x}(t_1, t_n) \dot{+} d_\mathfrak{x}(t_1, t_m) \dot{<} M \dot{+} (M \dot{-} \varepsilon) \dot{>} \varepsilon.$$

which completes the proof.

The intuition behind this result is that a sequence progressing in one direction and bounded by a fixed limit has no 'space' to diverge.

This theorem plays a central role in the infinite series theory and other areas such as Lebesgue integration.

REFERENCE

- Grossman, M., and Katz, R. (1972). Non-Newtonian calculus. Pigeon Cove, MA: Lee Press
- Grossman, M. (1979). An introduction to non-Newtonian calculus. *International Journal of Mathematical Education in Science and Technology*, 10(4), 525–528
- Mud, R. N. (2019). Monotone convergence in complete metric spaces (Bachelor's Project Mathematics)
- Mortici, C. (2025). Monotone sequences in metric spaces. *Journal of Science and Arts*, 25(1), 5–10
- Çakmak, A. F., and Başar, F. (2012). Some new results on sequence spaces with respect to non-Newtonian calculus. *J. Inequal. Appl.*, 228
- Duyar, C., Sağır, B., and Oğur, O. (2015). Some basic topological properties on non-Newtonian real line. *BJMCS*, 300–307
- Duyar, C., and Oğur, O. (2017). A note on topology of non-Newtonian real numbers. *IOSR J Math*, 13(6), 11–14
- Menger, K. (1928). Untersuchungen über allgemeine Metrik. *Mathematische Annalen*, 100(1), 75–163.
- Güngör, N., and Dinç, N. (2024). Non-Newtonian Sumudu Transform. *Maejo Int. J. Sci. Technol.*, 18(02), 130–145
- Sager, N., and Sağır, B. (2021). Some inequalities in the quasi-Banach algebra of non-Newtonian bicomplex numbers. *Filomat*, 35, 2231–2243
- Duyar, C., and Sağır, B. (2017). Non-Newtonian comment of Lebesgue measure in real numbers. *J. Math*, Article ID 6507013
- Değirmen, N., and Duyar, C. (2023). A new perspective on Fibonacci and Lucas numbers. *Filomat*, 37(28), 9561–9574
- Duyar, C., and Erdoğan, M. (2016). On non-Newtonian real number series. *IOSR J Math*, 12(6), 34–48
- Güngör, N. (2022). A note on linear non-Newtonian Volterra integral equations. *Math Sci*, 16, 373–387
- İ. Eryılmaz. (2024). Non-Newtonian Lebesgue spaces with their basic features. *J. Math. Ext.*, 18(7), 1–23
- Deza, M. M., and Deza, E. (2009). *Encyclopedia of distances*. Springer
- Rohman, M., and Eryılmaz, İ. (2023). Some basic results in v-normed spaces. *Indonesian Journal of Mathematics and Applications*, 1(1), 1-8.

A Complete Quadrangle-Based Approach to Complete $(k,4)$ -Arcs in $PG(2,4)$

**Elif ALTINTAŞ KAHRİMAN^{1,*}
Ayşe BAYAR ²**

- 1- Dr.; Bartın University, Department of Management Information System, Faculty of Economics and Administrative Sciences, akormaz@ogu.edu.tr ORCID No: 0000-0002-3454-0326
- 2- Prof. Dr.; Eskişehir Osmangazi University, Department of Mathematics and Computer Science, Faculty of Science,, akormaz@ogu.edu.tr ORCID No: 0000-0002-2210-5423

ABSTRACT

This chapter presents a systematic methodology for constructing complete $(k,4)$ -arcs in the finite projective plane $PG(2,4)$, grounded in the geometric structure of a complete quadrangle. An explicit algorithm is introduced to formalize the process of arc extension and completion, implemented computationally in C# to ensure reproducibility and methodological rigor.

The framework begins with the representation of $PG(2,4)$ using an irreducible polynomial over $GF(4)$, yielding 21 points and 21 lines. A complete quadrangle is then selected as the foundational configuration, and methodological variations arise from different treatments of its diagonal points. Four distinct approaches are considered: (i) including all diagonal points yields a complete $(13,4)$ -arc, (ii) including two diagonal points produces a complete $(16,4)$ -arc, (iii) including only one diagonal point results in a complete $(13,4)$ -arc, and (iv) excluding all diagonal points still allows the construction of a complete $(16,4)$ -arc. These results highlight the structural dependency between point selection and arc completion, underscoring the versatility of the quadrangle-based framework.

Beyond these specific constructions, the broader contribution of this work lies in offering a constructive and replicable methodology for generating arcs in $PG(2,4)$. By deepening the understanding of geometric configurations, the proposed framework provides a foundation for further applications in combinatorial design, coding theory, and the study of discrete mathematical structures.

Keywords – projective plane; $(k,3)$ -arc; complete quadrangle; finite geometry; $PG(2,4)$

INTRODUCTION

A projective plane P is characterized by a collection N of points and a collection D of subsets of N , which denote lines. Four points can define six separate lines in this arrangement, and every pair of points lies on exactly one line. Additionally, every pair of distinct lines connects at exactly one point. A subset B of points and lines that also constitutes a projective plane is regarded as a subplane of the projective plane P when we analyze the incidence relation within P .

In projective geometry, a complete quadrangle is a fundamental geometric construction made up of six lines connecting four points, none of which are collinear. This arrangement reveals intricate relationships between points and lines, establishing the foundation for understanding more complex geometric properties within projective planes.

Arcs are extensively utilized in combinatorics and related disciplines and are essential to projective geometry. In a finite projective plane π , a k -arc is a set K of k ($k \geq 3$) points such that no three points in K are collinear. If the plane π has order p , then $k \geq p+2$, but the maximum value of k can only be reached if p is even. A $(p+2)$ -arc is referred to as a hyperoval. Ovals are commonly discussed in the literature, and Hirschfeld is one source that does so (Hirschfeld and Thas, 2016). The literature on arcs in projective planes is extensive, particularly on complete $(k,2)$ -arcs with complete quadrangles that produce the Fano plane in the projective planes. They are thoroughly examined in (Bayar et al., 2016; Ekmekçi et al., 2016). The study of $(k,3)$ -arcs connected with a complete quadrangle in the projective plane $PG(2,5)$ has been presented in (Altıntaş Kahrıman and Bayar, 2024^a). Utilizing an arc-finding algorithm created in C# (Altıntaş Kahrıman and Bayar, 2024^b), the $(k,2)$ -arcs connected to a triangle and a quadrangle were examined in the projective plane $PG(2,4)$ over the finite field $GF(4)$.

ARCS IN PROJECTIVE PLANES

Key concepts in projective geometry are covered in this part, such as projective planes, finite fields, arc properties, and a complete quadrangle configuration. The basis for our investigation is provided by these definitions.

Definition 1. In a projective plane (N, D, ϕ) , the set N represents points and D denotes lines (subsets of N), with the following axioms holding: every pair of points lies on one and only one line, each pair of distinct lines meets at exactly one point, and there are four non-collinear points, no three of which lie on a common line.

Definition 2. The vector space $V(n+1, q)$ is $(n+1)$ -dimensional and consists of vectors with coordinates from the finite field $GF(q)$. The projective space $PG(n, q)$ is defined as the collection of points, each corresponding to a line that passes through the origin in $V(n+1, q)$. Specifically, this means that each point in $PG(n, q)$ can be represented as $P(x)$, where x is any non-zero vector in $V(n+1, q)$. If K is the finite field $GF(q)$, also denoted as F_q , then the n -dimensional projective plane is referred to as $PG(n, K)$ or $PG(n, q)$. In this context, q represents the order of $PG(n, q)$. The number of points in this projective plane can be determined using the formula

$$\theta(n) = \frac{q^{n+1}-1}{q-1}.$$

(x_1, x_2, \dots, x_n) represents a point in N , where x_1, x_2, \dots, x_n are not all zero, and $(\lambda x_1, \lambda x_2, \dots, \lambda x_n) \equiv (x_1, x_2, \dots, x_n)$, $\lambda \in K \setminus \{0\}$. Similarly, the notation $[a_1, a_2, \dots, a_n]$ denotes any line in D , where a_1, a_2, \dots, a_n are not

all zero. The relationship $[\mu a_1, \dots, \mu a_n] \equiv [a_1, \dots, a_n]$ holds for $\mu \in K \setminus \{0\}$. The projective plane P_2K is characterized as a point-line geometry (N, D, \circ) defined by K . The incidence relation is given by \circ :

$$(x_1, \dots, x_n) \circ [a_1, \dots, a_n] \Leftrightarrow a_1x_1 + a_2x_2 + a_3x_3 + \dots + a_nx_n = 0$$

Let p denote a prime number and r a positive integer. The projective plane of order $q = p^r$ over the finite field $K = GF(p^r)$, where p^r represents the number of elements, is expressed as $P_2K = PG(2, p^r)$ (Hirschfeld and Thas, 1991).

Definition 3. If four points in a plane are joined in pairs by six distinct lines, they are called the vertices of a complete quadrangle, and the lines are its 6 sides. Two sides are said to be opposite if their common point is not a vertex. The common point of two opposite sides is called a diagonal point. There are 3 diagonal points. The quadrangle is $ABCD$, its sides are AD, BD, CD, BC, CA, AB and its diagonal points are E, F, G (Coxeter, 1987).

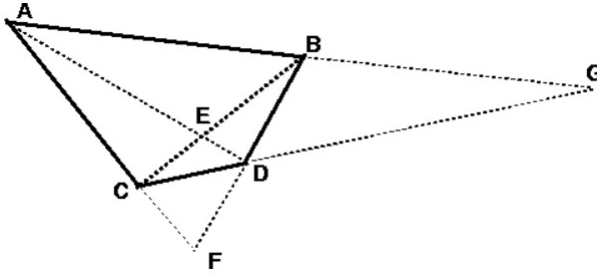


Figure 1. Complete Quadrangle

Definition 4. In a projective plane, a (k, n) -arc \mathcal{K} is a set of k points such that some line intersects \mathcal{K} in n points, and no line intersects \mathcal{K} in more than n points, where $n \geq 2$ (Hirschfeld and Voloch, 2015)

If there isn't a $(k + 1, n)$ -arc that contains a (k, n) -arc, then it is complete.

CONSTRUCTION OF THE PROJECTIVE PLANE OF ORDER 4

The irreducible polynomial $f(x) = x^2 + x + 1$, where the elements $0, 1, t, t^2$ of $GF(4)$, is used to construct $PG(2, 4)$, which has 21 points and 21 lines over $GF(4)$. In $PG(2, 4)$, each line has five points, and each point has five lines that pass through it (Ekmekçi et al., 2022).

The projective plane $PG(2, 4)$ has a point set N that is $N = \{N_i \mid i = 1, 2, \dots, 21\}$, where

$$N_1 = (0, 1, 0), N_2 = (0, 0, 1), N_3 = (0, 1, 1), N_4 = (0, 1, t^2), N_5 = (0, 1, t),$$

$$\begin{aligned}
N_6 &= (1,1,1), N_7 = (1,0,1), N_8 = (1,t,1), N_9 = (1,t^2,1), \\
N_{10} &= (1,1,0), N_{11} = (1,1,t^2), N_{12} = (1,1,t), N_{13} = (1,t,t^2) \\
N_{14} &= (1,t^2,t), N_{15} = (1,0,0), N_{16} = (1,t,0), N_{17} = (1,t^2,0), \\
N_{18} &= (1,0,t^2), N_{19} = (1,0,t), N_{20} = (1,t^2,t^2), N_{21} = (1,t,t).
\end{aligned}$$

Table 1 provides the $PG(2,4)$ incident relation table. Each row represents points located on the line $D_i, i = 1, 2, \dots, 21$.

Table 1. The lines of $PG(2,4)$

D_1	N_1	N_2	N_3	N_4	N_5
D_2	N_1	N_6	N_7	N_8	N_9
D_3	N_1	N_{10}	N_{15}	N_{16}	N_{17}
D_4	N_1	N_{11}	N_{13}	N_{18}	N_{20}
D_5	N_1	N_{12}	N_{14}	N_{19}	N_{21}
D_6	N_2	N_6	N_{10}	N_{11}	N_{12}
D_7	N_2	N_7	N_{15}	N_{18}	N_{19}
D_8	N_2	N_9	N_{14}	N_{17}	N_{20}
D_9	N_2	N_8	N_{13}	N_{16}	N_{21}
D_{10}	N_3	N_6	N_{15}	N_{20}	N_{21}
D_{11}	N_5	N_6	N_{14}	N_{16}	N_{18}
D_{12}	N_4	N_6	N_{13}	N_{17}	N_{19}
D_{13}	N_3	N_7	N_{10}	N_{13}	N_{14}
D_{14}	N_3	N_8	N_{12}	N_{17}	N_{18}
D_{15}	N_3	N_9	N_{11}	N_{16}	N_{19}
D_{16}	N_4	N_7	N_{12}	N_{16}	N_{20}
D_{17}	N_5	N_7	N_{11}	N_{17}	N_{21}
D_{18}	N_5	N_8	N_{10}	N_{19}	N_{20}
D_{19}	N_4	N_9	N_{10}	N_{18}	N_{21}
D_{20}	N_5	N_9	N_{12}	N_{13}	N_{15}
D_{21}	N_4	N_8	N_{11}	N_{14}	N_{15}

METHODS FOR CONSTRUCTING COMPLETE $(k,4)$ -ARCS FROM COMPLETE QUADRANGLES IN $PG(2,4)$

This section presents an algorithm used to construct complete $(k,4)$ -arcs by including the vertices and diagonal points of a complete quadrangle configuration in $PG(2,4)$.

- Method 1. \rightarrow constructs a complete $(k,4)$ -arcs containing the vertices and all diagonal points of the complete quadrangle.
- Method 2. \rightarrow constructs a complete $(k,4)$ -arcs containing the vertices and two of the diagonal points of the complete quadrangle.
- Method 3. \rightarrow constructs a complete $(k,4)$ -arcs containing the vertices and only one of the diagonal points of the complete quadrangle.
- Method 4. \rightarrow constructs a complete $(k,4)$ -arcs containing the vertices and none of the diagonal points of the complete quadrangle.

Each method follows a structured approach, ensuring systematic identification and completion of arcs.

Methodology: Constructing $(k,4)$ -Arcs in $PG(2,4)$

This section presents an algorithm designed to construct $(k,4)$ -arcs, incorporating the complete quadrangle and participating diagonal points of the complete quadrangle in $PG(2,4)$. The algorithm follows a structured approach, ensuring systematic identification and extension of arcs.

Before starting the methodological approaches, the construction of the projective plane and the choice of the complete quadrangle, which are necessary for all methodologies, must be performed as follows:

With the help of an irreducible polynomial $f(x) = x^2 + x + 1$ over $GF(4)$, 21 points and 21 lines of $PG(2,4)$ are determined and a complete quadrangle Q is selected as consisting of seven points A, B, C, D, E, F, G where A, B, C, D are the vertices, and E, F, G are the diagonal points of Q in this plane.

Method 1. Constructing complete $(k,4)$ -Arcs containing the vertices and all diagonal points of a complete quadrangle

When the algorithm is applied to the vertices and all diagonal points of a complete quadrangle Q selected in the $PG(2,4)$ to construct $(k,4)$ -arcs, there remain 14 points on the 7 lines of the complete quadrangle that can still be added. The 12 points not on the diagonal line, lie in pairs on the side lines of the quadrangle. By adding one of these two remaining points on each side lines of the complete quadrangle to the points of Q , a complete $(13,4)$ -arc is obtained.

Method 2. Constructing complete $(k,4)$ -Arcs containing the vertices and two of the diagonal points of a complete quadrangle

When the algorithm is applied to the vertices and two of the three diagonal points of a complete quadrangle Q selected in $PG(2,4)$, 14 points remain to be added excluding the remaining diagonal point. If both of the remaining points on the three lines of the complete quadrangle that pass through the remaining diagonal point are added to the $(6,3)$ -arc determined by the vertices and two diagonal points of Q , an incomplete $(12,4)$ -arc is obtained. Subsequently, if one of the two remaining points on each of the four side lines not passing through the remaining diagonal point of the quadrangle is selected and added to this incomplete $(12,4)$ -arc, then a complete $(16,4)$ -arc is obtained.

Method 3. Constructing complete $(k,4)$ -Arcs containing the vertices and only one of the diagonal points of a complete quadrangle

When the vertices and only one of the diagonal points of a complete quadrangle Q selected in $PG(2,4)$ are taken and the algorithm is applied, 14 points remain, excluding the diagonal points, to be added to the $(5,3)$ -arc determined by the vertices and the chosen diagonal point of Q . By adding all of the remaining points on any three of the four side lines of the quadrangle that do not pass through the chosen diagonal point, together with one suitable point of the remaining points on each of the side lines passing through the chosen diagonal point, a complete $(13,4)$ -arc is obtained.

Method 4. Constructing complete $(k,4)$ -Arcs containing the vertices of a complete quadrangle

Beginning with the vertices of a complete quadrangle Q selected in the $PG(2,4)$ and excluding all of its diagonal points, the algorithm identifies 14 remaining points, two of which lie on the diagonal line of Q . By systematically adding two of the remaining points on each of the side lines not on the diagonal line of Q , and applying the algorithm to these points together with the vertices of Q , the construction yields a complete $(16,4)$ -arc.

Algorithm Implementation

We present the following algorithm, implemented in $C\#$, designed to identify complete $(k,4)$ -arcs within $PG(2,4)$:

```
A ← Read(Excel File)
B ← Read(Text File)
C ← A
while s(C)>0
```

```

 $B_i \leftarrow \text{input}(b), \{b|b \in C, b \notin B, i = s(B) + 1\}$ 
 $j=1$ 
while  $j \leq s(B)$ 
  for  $k=(j+1)$  to  $s(B)$ 
     $m \leftarrow$  the index of row on  $B_j, B_k$ 
     $D \leftarrow A_{mn}; \{A_{mn}|A_{mn} \neq B_j, A_{mn} \neq B_k, n = 1, \dots, 10\}$ 
    Remove  $a$  from  $A; \{a|a \in A, a \in D\}$ 
     $C \leftarrow c; \{c|c \in A, c \notin C\}$ 
  end for
   $j=j+1$ 
end while
end while

```

EXAMPLES OF COMPLETE (k,4)-ARCS

In this chapter, four distinct examples are presented, each corresponding to Methodologies 1–4 introduced in the previous chapter. Let Q denote the complete quadrangle $N_2 N_6 N_{15} N_{17}$. By applying the incidence relations provided in Table 1, it follows that N_{10}, N_{19} , and N_{20} are the diagonal points of the complete quadrangle Q . If the vertices of the complete quadrangle N_2, N_6, N_{15}, N_{17} are taken in $PG(2,4)$, and the algorithm is applied to the vertices of Q , then $N_1, N_3, N_4, N_5, N_7, N_8, N_9, N_{10}, N_{11}, N_{12}, N_{13}, N_{14}, N_{16}, N_{18}, N_{19}, N_{20}, N_{21}$ points are remained. According to our methodologies and adding diagonal points to the vertices of Q , we have four different examples as follows:

Example 1. (According to Method 1) When this algorithm is applied to the vertices and all diagonal points of Q , there remain 14 points on the lines of the complete quadrangle that potentially be included, namely: $N_1, N_3, N_4, N_5, N_7, N_8, N_9, N_{11}, N_{12}, N_{13}, N_{14}, N_{16}, N_{18}, N_{21}$. In addition, $\{N_2, N_6, N_{10}, N_{15}, N_{17}, N_{19}, N_{20}\}$ constitutes a complete (7,3)-arc in $PG(2,4)$. These remaining points appear in pairs on the side lines of the quadrangle. By selecting and adding one of the two remaining points on each side line of the quadrangle excluding the diagonal line to this complete (7,3)-arc, for instance, N_1 or N_{16} , N_3 or N_{21} , N_4 or N_{13} , N_7 or N_{18} , N_9 or N_{14} , N_{11} or N_{12} , and then applying the algorithm to these thirteen points, complete (13,4)-arcs are obtained. For example, if the remaining points are chosen as $N_1, N_3, N_4, N_7, N_9, N_{11}$ and added to the complete (7,3)-arc determined by Q , the resulting complete (13,4)-arc is $\{N_1, N_2, N_3, N_4, N_6, N_7, N_9, N_{10}, N_{11}, N_{15}, N_{17}, N_{19}, N_{20}\}$. In a similar manner, by considering different selections of the remaining points, further complete (13,4)-arcs can be obtained. Using this method, and by applying the algorithm, a total of 64 distinct complete (13,4)-arcs can be constructed, each arising from a different possible choice of the remaining points.

Example 2. (According to Method 2) If two diagonal points N_{10}, N_{20} and vertices N_2, N_6, N_{15}, N_{17} of the complete quadrangle are selected to construct $(k, 4)$ -arc, and the algorithm is applied to these six points, an incomplete $(6, 3)$ -arc is obtained as $\{N_2, N_6, N_{10}, N_{15}, N_{17}, N_{20}\}$. Accordingly, 14 different points $N_1, N_3, N_4, N_5, N_7, N_8, N_9, N_{11}, N_{12}, N_{13}, N_{14}, N_{16}, N_{18}, N_{21}$ remain to be added to this incomplete $(6, 3)$ -arc except for one diagonal point. If all of the remaining points on the three lines of the complete quadrangle that pass through the remaining diagonal point N_{19} are added to this incomplete $(6, 3)$ -arc determined by the vertices and two diagonal point of Q , an incomplete $(12, 4)$ -arc is obtained as $\{N_2, N_4, N_5, N_6, N_7, N_8, N_{10}, N_{13}, N_{15}, N_{17}, N_{18}, N_{20}\}$. Subsequently, by selecting and adding one of the two remaining points on each of the other four side lines of the quadrangle is selected and added to this incomplete $(12, 4)$ -arc, for instance, N_{11} or N_{12} , N_1 or N_{16} , N_9 or N_{14} , N_3 or N_{21} , and then applying the algorithm to these twelve points, complete $(16, 4)$ -arcs are obtained. For example, if the remaining points are chosen as N_3, N_9, N_{11}, N_{16} , and added to $\{N_2, N_4, N_5, N_6, N_7, N_8, N_{10}, N_{13}, N_{15}, N_{17}, N_{18}, N_{20}\}$, the resulting complete $(16, 4)$ -arc is $\{N_2, N_3, N_4, N_5, N_6, N_7, N_8, N_9, N_{10}, N_{11}, N_{13}, N_{15}, N_{16}, N_{17}, N_{18}, N_{20}\}$. Further complete $(16, 4)$ -arcs can be obtained by considering alternative selections of the remaining points. Applying this procedure with the algorithm yields exactly 16 distinct complete $(16, 4)$ -arcs, each determined by a different choice of points.

Example 3. (According to Method 3) Starting with the vertices N_2, N_6, N_{15}, N_{17} and the diagonal point N_{20} of the complete quadrangle Q , an initial incomplete $(5, 3)$ -arc is formed as $\{N_2, N_6, N_{15}, N_{17}, N_{20}\}$, leaving 14 remaining points except for two diagonal points that can be added to the arc determined by the vertices and the chosen diagonal point of Q . By adding all of the remaining points on any three of the four side lines of the quadrangle that do not pass through the chosen diagonal point, N_{20} , together with one suitable point of the remaining points on each of the side lines passing through the chosen diagonal point, N_{20} , a complete $(13, 4)$ -arc is obtained. For example, if the remaining points are chosen as $N_4, N_{13}, N_7, N_{18}, N_{11}, N_{12}$ on any three of the four side lines of the quadrangle that do not pass through the chosen diagonal point, N_{20} , and N_3, N_9 on each of the side lines passing through N_{20} , and added to $\{N_2, N_6, N_{15}, N_{17}, N_{20}\}$, the resulting complete $(13, 4)$ -arc is $\{N_2, N_3, N_4, N_6, N_7, N_9, N_{11}, N_{12}, N_{13}, N_{15}, N_{17}, N_{18}, N_{20}\}$. Further complete $(13, 4)$ -arcs can be obtained by considering alternative selections of the remaining points.

Example 4. (According to Method 4) Starting with the vertices N_2, N_6, N_{15}, N_{17} of the complete quadrangle Q to construct $(k, 4)$ -arc not containing any diagonal points of Q , and the algorithm is applied, leaving 14 remaining

points except for the all diagonal points. Two of these fourteen remaining points are on the diagonal line of Q . By successively adding two remaining points on each side of complete quadrangle that are not on the diagonal line, namely, $N_{11}, N_{12}, N_3, N_{21}, N_4, N_{13}, N_{18}, N_7, N_1, N_{16}, N_9, N_{14}$, and applying the algorithm to these points together with the vertices of Q , this results in the $(16,4)$ -arc $\{N_1, N_2, N_3, N_4, N_6, N_7, N_9, N_{11}, N_{12}, N_{13}, N_{14}, N_{15}, N_{16}, N_{17}, N_{18}, N_{21}\}$. When the algorithm is applied to this $(16,4)$ -arc, no remaining points can be added to it, and thus the resulting $(16,4)$ -arc is complete.

CONCLUSION

This book chapter has detailed a systematic approach for constructing $(k,4)$ -arcs within the projective plane $PG(2,4)$, utilizing the fundamental structure of a complete quadrangle. The methodologies presented demonstrate that the properties and composition of the initial point set—specifically, the inclusion or exclusion of the complete quadrangle’s vertices and diagonal points—significantly influence the size and structure of the constructed arc. Four distinct methodological approaches were introduced, each leading to different configurations of complete arcs.

- Method 1 demonstrated the construction of a complete $(13,4)$ -arc by utilizing the vertices together with all diagonal points and supplementing them with one additional point from each side line.
- Method 2 illustrated how, by including two diagonal points and then systematically adding appropriate points from side lines, a complete $(16,4)$ -arc can be obtained.
- Method 3 showed that, when only one diagonal point is considered, the process results in a complete $(13,4)$ -arc through a selective addition of points from side lines.
- Method 4 highlighted that even when no diagonal points are included, the algorithm still produces a complete $(16,4)$ -arc by successively incorporating pairs of points from the side lines of the quadrangle.

These results not only provide specific examples of complete arcs but also offer a robust, replicable procedure for their generation. This work contributes to the study of finite geometry by providing an explicit algorithm for arc construction, thereby enriching the understanding of geometric configurations in $PG(2,4)$.

REFERENCES

Altıntaş Kahrıman E, Bayar A. (2024^a). Investigating Incomplete $(7,3)$ -Arcs and Their Extensions in $PG(2,5)$: A Study On Secants And Complete Quadrangles.

In: 5. Bilisel International World Scientific And Research Congress; 05-06 October, İstanbul, Türkiye. pp.536-545.

Altıntaş Kahriman E, Bayar A. (2024^b). An Algorithm For Constructing $(k,2)$ -Arcs Containing Triangle And Quadrangle in $PG(2,4)$. In: 5. Bilisel International Gordion Scientific Researches Congress; 08-09 December, Ankara/ Türkiye. pp.987-997.

Bayar A, Akca Z, Altintas E, Ekmekci S. (2016). On the complete arcs containing the quadrangles constructing the Fano planes of the left near field plane of order 9. New Trend Math. Sci. 4(4), 266-266. <http://dx.doi.org/10.20852/ntmsci.2016.113>

Coxeter H.S.M. (1987). Projective geometry. Springer, pp. 7; 95.

Ekmekci S, Bayar A, Altintas E, Akca Z. (2016). On the Complete $(k,2)$ - Arcs of the Hall Plane of Order 9. IJARCSSE, 6 (10), 282-288. ISSN: 2277 128X.

Ekmekci S, Bayar A, Akca Z. (2022). On The Projective Planes In Projective Space $PG(4,4)$. Erciyes Üniversitesi Fen Bilimleri Enstitüsü Fen Bilimleri Dergisi, 38(3), 519-524.

Hirschfeld J.W.P, Thas J.A. (1991). General Galois Geometries. The Charendon Press, Oxford.

Hirschfeld J.W.P, Voloch J.F. (2015). Group-arcs of prime order on cubic curves, Finite Geometry and Combinatorics, 191, 177-185.

Hirschfeld J.W.P, Thas J.A. (2016). General Galois Geometries. Springer Monographs in Mathematics. Springer- Verlag London.

Preparation of Electrodes through Pseudocapacitors, Electric double layer capacitance and Hybrid Supercapacitor Systems

Murat ATES¹

1- Prof. Dr. Murat ATES; Tekirdağ Namık Kemal Üniversitesi, Fen-Edebiyat Fakültesi, Kimya Bölümü.
mates@nku.edu.tr, ORCID No: 0000-0002-1806-0330.

ABSTRACT

Supercapacitors (SCs) have many advantageous than other systems such as long-term stability, fast charge-discharge capabilities, and high power density (Ishaq et al., 2019). SC performances are mostly depends on using different types of electrode components. These are affected by charge-storage mechanisms. Supercapacitors are divided into three sections. These are electric double layer capacitors (EDLC), which mostly consititutes from carbanous materials, such as C60, reduced graphene oxide (rGO), carbon nanotube (CNT), etc. Capacitance can be obtained from charge seperation of electrode and Helmholtz plane (Dhibar, et al., 2015). The second one is called as pseudocapacitance (PCs), which have including metal oxides, metal sulfides or conducting polymers. They have fast and reversible redox recations on the electrode surface. In literature, there are many different kinds of conducting polymers, such as polypyrrole, polycarbazole, polythiophene, etc. They can be used as an electrode component in supercapacitors due to their low-cost and high electrical conductivity (Hu, et al., 2011). The third one is the hybrid capacitors (HCs), which consists of both EDLC and PCs mechanisms. Supercapacitors have 3 main components, which are electrode materials, electrolyte type and used current collectors (stainless steel, copper or aluminum, etc.). The most critical importance is type of electrode materials. There are many different types of electrode materials. Electrochemical performance of SC devives can be decided by type of electrode materials.

Keywords – Supercapacitors, EDLC, pseudocapacitance, hybrid supercapacitor, electrodes

INTRODUCTION

Nowdays, supercapacitors are used in different energy storage systems such as mobile phones, memory back-up systems, aerospace, laptops, etc (Cui, et al., 2016; Jobeen, et al., 2016). It is mostly used due to its high electrochemical performances (high capacitance, high power density and good stability performance during charging-discharging processes). All scientists concentrate on to develop highly efficient supercapacitors such as high electrochemical performance, easy preparation, eco-frindly (Ates, et al., 2018).

Supercapacitors have 3 main storage mechanisms for their usage (Moyseowicz, et al., 2017). These are EDLC, PCs, and HCs. In general, carbanous materials, such as, graphene, fullerene, hard carbon, and carbon fibers work with EDLC systems. In literature, graphene oxide (GO)-based composites were synthesized both chemically and electrochemically ways

(Phan, et al., 2016). Metal oxides and sulfides such as Fe_2O_3 , TiO_2 , RuO_2 , MoS_2 , etc. and conducting polymers such as polyvinylcarbazole, polypyrrole (PPy) work in PCs mechanism. In addition, there is another mechanism that includes both EDLC and PC systems on the electrode surface.

Vapor phase polymerization (VPP) technique has been developed recently to synthesize conducting polymers. It has some advantages such as highly ordered film formation, improving electrical conductivity, etc. In literature, graphene (G)-PEDOT films were formed to use in SC applications (Chen et al., 2013).

Ionic liquid is also used to increase the potential window in supercapacitor devices. For example, *N*-butyl-*N*-methyl pyrrolidiniumbis(trifluoromethane sulfonyl)-imide (PYR-TFSI) was used together with poly(3,4-dimethylthiophene) and its copolymers (Lagoutte et al., 2013). This electrolyte enhances the ionic conductivity of SC device (Galinski et al., 2006).

Pseudocapacitors (PCs)

In literature, there are many PC materials including metal oxides, metal sulfides and conducting polymers (Owusu, et al., 2017). A new type of PC materials, Mxenes are used in supercapacitors to increase the Faradaic reactions (Kim et al., 2021).

Bao et al. have been presented cobalt-iron PBA nanotubes with a redox polymer nanoskin (CFP@PTMT), which is used in supercapacitor applications (Bao et al., 2025). It has a good electrochemical performances such as $C_{sp}=984 \text{ F/g}$ at 1 A/g , and long-term stability performance (87.19%) over 5000 cycles (Fig.1).

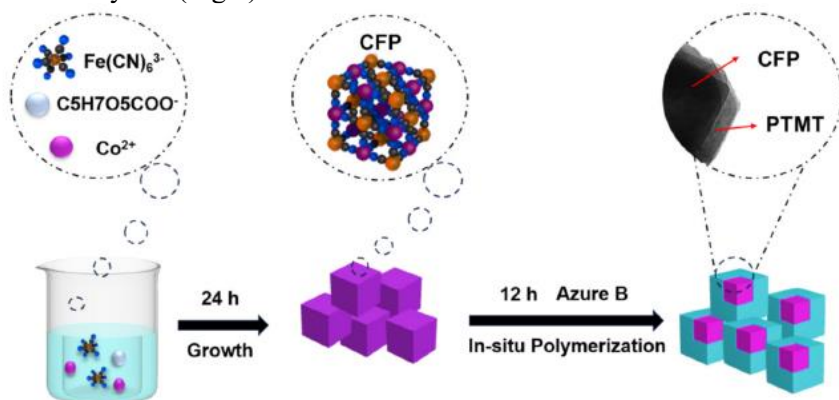


Fig. 1. Experimental synthesis way of CFP@PTMT. Permission was taken from Ref (Bao, et al., 2025).

Polythiophene (PTh) and polypyrrole (PPy) were chemically polymerized to form PPy/PTh/TiO₂ composite, which shows the highest capacitance of $C_{sp}=271.8$ F/g. It is compared to other composites such as PT/TiO₂ ($C_{sp}=109.6$ F/g) and PPy/TiO₂ ($C_{sp}= 80.4$ F/g) (Sowmiya and Velraj, 2020). Conducting polymer based PCs have low and limited cyclic stability performance due to the pulverization during repetitive charge-discharge performances (Song, et al., 2019). Long term stability performance of SC depends on the mechanical properties of electrode components (Wang et al., 2016).

Electric double layer capacitors (EDLC)

Charge-storage in the supercapacitors is also supplied by the Helmholtz plane between electrode and electrolyte due to the charge separation (Thakur, et al., 2018). Carbanous materials are mostly wide surface area and are commonly used for EDLCs mechanism (Muniraj, et al., 2016).

Porous carbanous materials have EDLC supercapacitor mechanism, where pore size, electrical conductivity, surface area of the electrode are critical important to obtain a higher electrochemical performance of SC. It supplied from Faradaic reactions (Lai et al., 2012). Graphene based composites have been preferred in SCs because of their mechanical strength, high thermal stability, high capacitance and good electron mobility (Solonaru and Grigoras, 2017). Reduced graphene oxide was used in electrode component with high surface area (2670 m²/g) (Guan, et al., 2016; Chen, et al., 2017), high mechanical properties (Han, et al., 2019) and high electrical and thermal conductivity (Li, et al., 2015). Theoretically, a specific capacitance of graphene was given as $C_{sp}=550$ F/g (Liu et al., 2010). However, the specific capacitance changes with different electrolyte solutions from 100 F/g to 300 F/g (Wang, et al., 2009; Kuok, et al., 2017). There is a small gap between the valance and conduction bands of rGO (Yea et al., 2012).

In literature, power law dependence can be evaluated by CV method to understand the capacitive process or diffusion-limited Faradaic intercalation process (Li et al., 2019). It depends on the current (I) on the scan rate, ν .

$$i_p = a \times \nu^b \quad (1)$$

a and b are used as variables.

3D graphene have some disordered pores due to the agglomeration of graphene sheets. Thus, flexible and preventing self-stacking of graphene

is important scientific challenges. Hybrid systems of both EDLC and PCs materials have a good solution of this problem (Meng et al., 2013).

Hybrid capacitors

In literature, there are many studies includes both EDLC and PCs mechanisms. For example, rGO/CuO/PANI nanocomposites were presented in different weight ratio of $w_{\text{ANI}} / w_{\text{CuO}}$. It shows a good electrochemical performances such as $E=18.95$ Wh/kg and $P=545.79$ W/kg (Viswanathan and Shetty, 2017).

Liu et al. have presented N doped $\text{Fe}_2\text{O}_3/\text{rGO}$ for anode side and $\text{NiCo LDH}/\text{Co}(\text{OH})_2$ for cathode for side. In this study, two PCs materials were used to improve electrical conductivity of electrode. Anode electrode presents a specific capacitance of $C_{\text{sp}}=912.9$ F/g at 1 A/g and stability performance of 84% at 30 A/g. Cathode electrode delivers a high capacitance of $C_{\text{sp}}= 2220$ F/g at 1 A/g (Liu et al., 2021) (Fig.2).

Wang et al. have presented graphene/polyaniline/ Co_3O_4 ternary composite for supercapacitor applications. It exhibits an outstanding performance with high capacitance of $C_{\text{sp}}=789.7$ F/g at 1 A/g. In addition, it shows an initial capacitance retention of ~82% at 10 A/g for 1000 cycles (Wang et al., 2017).

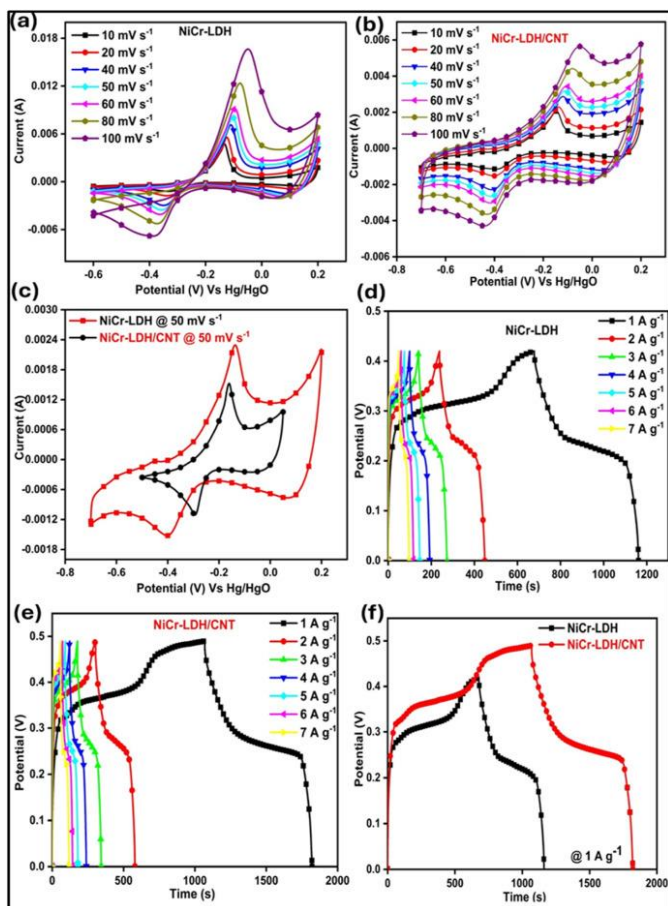


Fig. 2. CV plots of a) NiCr-LDH, b) NiCr-LDH/CNT, c) CV comparison at different scan rates, d) GCD plots of NiCr-LDH, e) GCD plots of NiCr-LDH/CNT, f) GCD comparison at different current densities. Permission was taken from Ref (Ashwini Chavan, et al., 2025).

Carbanous materials such as fullerene are important electrode components for composite formation. However, they have insufficient Coulombic efficiency (ICE) and expensive for use in supercapacitors. To decrease the total price of SC device, some preferable combination of carbon based materials with convenient cheaper materials such as silicone. It supplies a higher capacitive performance with silicone / carbon composite materials for long-term stability performance of SC devices (Hu et al., 2020).

Carbanous materials have weak interface interactions. Moreover, metal oxides, and their coatings have low conductivity (Ren et al., 2022; Liu, et al., 2025). Conjugated polymers have improve the capacitance and energy

and power density of electrode materials due to their electrical conductivity and good adhesion properties of other materials (Mohamed, et al., 2024).

Sharma et al. have presented TiO₂/NiO/rGO nanocomposite for a photocatalyst for efficient degradation of o-chlorophenol (Sharma and Lee, 2016). In addition, Xu et al. have reported poly(aniline-co-methoxyaniline) / MWCNT composite, which has a capacitance of $C_{sp}=484$ F/g (Xu, et al., 2013).

RESULTS AND DISCUSSION

In this study, three different mechanisms including PCs, EDLC and hybrid supercapacitor systems were investigated in more detail. The critical question is that which type of electrode components will be used to obtain a higher electrochemical performance of SCs.

Therefore, the selection of suitable electrode materials with a convenient charge storage mechanisms designed into SCs can better utilize their strengths and boost the energy and power densities and long cycle life.

REFERENCE

- Ates, M., Caliskan, S., Ozten, E. (2018). Synthesis of ternary polypyrrole / Ag nanoparticle/graphene nanocomposites for asymmetric supercapacitor devices. *J Solid State Electrochem.*, 22(3), 773-784.
- Ashwini Chavan, V.M., Shireesha, G., Rastogi, C.K., Manjunatha, C. (2025). Nickel chromium-LDH/CNT composite for supercapacitors: Synergistic conductive for superior energy storage. *J. Power Sources*, 654, Article number: 237807.
- Bao, Y., Chen, G., Zhu, X., Zou, P., Yang, Q., Yuan, S., Chen, C. (2025). Encapsulation of cobalt-iron Prussian-blue analog nanotubes using a redox polymer for advanced supercapacitor cathode materials. *J. Colloid Interface Sci.*, 697, Article number: 137975.
- Cui, L., Huang, L., Ji, M., Wang, Y., Shi, H., Zuo, Y., Kang, S. (2016). High-performance MgCo₂O₄ nano-cone arrays grown on three-dimensional nickel foams: Preparation and application as binder-free electrode for pseudo-supercapacitor. *Power Sources*, 333, 118-124.
- Chen, Y., Xu, J., Mao, Y., Yang, Y., Yang, W., Li, S. (2013). Electrochemical performance of graphene-polyethylenedioxythiophene nanocomposites. *Mater. Sci. Eng. B.*, 178, 1152-1157.
- Chen, J., Wang, Y., Cao, J., Liu, Y., Zhou, Y., Quyang, J.H., Jia, D. (2017). Facile co-electrodeposition method for high performance supercapacitor based on reduced graphene oxide / polypyrrole composite film. *ACS Appl. Mater. Interfaces*, 9, 19831-19842.

- Chang, B.Y.S., Huang, N.M., An'amt, M.N., Marlinda, A.R., Norazriera, Y., Muhamad, M.R., Harrison, I., Lim, H.N., Chia, C.H. (2012). Facile hydrothermal preparation of titanium dioxide decorated reduced graphene oxide nanocomposite. *Int. J. Nanomedicine*, 7, 3379-3387.
- Dhibar, S., Bhattacharya, P., Hatui, G., Das, C.K. (2015). Transition metal doped poly(aniline-co-pyrrole) / multi-walled carbon nanotubes nanocomposite for high performance supercapacitor electrode materials. *J. Alloys Compds.*, 625, 64-75.
- Galinski, M., Lewandowski, A., Stepniak, I. (2006). Ionic liquids as electrolytes. *Electrochim. Acta*, 51, 5567-5580.
- Guan, L., Yu, L.P., Chen, G.Z. (2016). Capacitive and non-capacitive faradaic charge-storage. *Electrochim. Acta*, 206, 464-478.
- Han, H., Lee, S.W., Moon, K.H., Cho, S. (2019). Fabrication of solid state asymmetric supercapacitors based on aniline oligomers and graphene electrodes with enhanced electrochemical performances. *ACS Omega*, 4, 1244-1253.
- Hu, W.L., Chen, S.Y., Yang, Z.H., Liu, L.T., Wang, H.P. (2011). Flexible electrically conductive nanocomposite membrane based on bacterial cellulose and polyaniline. *J. Phys. Chem. B.*, 115(26), 8453-8457.
- Hu, Y., Yu, B., Qi, Y., Shi, B., Fang, S., Yu, Z., Yang, J (2020). The preparation of graphite / silicone @ carbon composites for lithium-ion batteries through molten salts electrolysis. *J. Mater. Sci.*, 55, 10155-10167.
- Ishaq, S., Moussa, M., Kanwal, F., Ehsan, M., Saleem, M., Ngo Van, T., Losic, D. (2015). Facile synthesis of ternary graphene nanocomposites with doped metal oxide and conductive polymers as electrode materials for high-performance supercapacitors. *Scientific Reports*, 9, Article number: 5974.
- Jabeen, N., Xia, Q., Yang, M., Xia, H. (2016). Unique core-shell nanorod arrays with polyaniline deposited into mesoporous NiCo₂O₄ support for high-performance supercapacitor electrodes. *ACS Appl. Mater. Interfaces*, 8, 6093-6100.
- Kim, E., Lee, B.J., Maleski, K., Chae, Y., Lee, Y., Gogotsi, Y., Ahn, C.W. (2021). Micro-supercapacitor with a 500 nm gap between MXene / CNT electrodes. *Nano Energy*, 81, Article number: 105616.
- Kuok, F.H., Liao, C.Y., Wan, T.H., Yeh, P.W., Cheng, I.C., Chen, J.Z. (2017). Atmospheric pressure plasma jet processed reduced graphene oxides for supercapacitor application, *J. Alloys Compds.*, 692, 558-562.

- Lagoutte, S., Aubert, P.H., Tran-Van, F., Sallenave, X., Laffaiteur, C., Sarrazin, C., Chevrot, C (2013). Electrochemical and optical properties of poly(3,4-dimethyl thiophene) and its copolymers with 3-methylthiophene in ionic liquids media. *Electrochim. Acta*, 106, 13-22.
- Lai, L., Yang, H., Wang, L., Teh, B.K., Zhang, J., Chou, H., Chen, L., Chen, W., Shen, Z., Ruoff, R.S., Lin, J. (2012). Preparation of supercapacitor electrodes through selection of graphene surface functionalities, *ACS Nano*, 6 (7), 5941-5951.
- Li, H., Li, X., Liang, J., Chen, Y. (2019). Microsupercapacitors: Hydrous RuO₂-decorated MXene coordinating with silver nanowire inks enabling fully printed micro-supercapacitors with extraordinary volumetric performance. *Adv. Energy Mater.* 9, Article number: 1970050.
- Li, J., Zheng, S., Wang, X., Yang, H., Loos, K., Xu, Q. (2015). Effect of supercritical CO₂ on the morphology and fluorescent behaviour of fluorinated poly(ylidene) fluorenes derivative / graphene oxide nanohybrids. *Mater. Lett.*, 158, 147-150.
- Liu, C., Zhenning, Y., Neff, D., Zhamu, A., Jang, B.Z. (2010). Graphene-based supercapacitor with an ultra-high energy density, *Nano Lett.*, 10(12), Article number: 4863.
- Liu H, Zhu J, Li Z, Shi Z, Zhu J, Mei H (2021). Fe₂O₃/N doped rGO anode hybridized with NiCo LDH/Co(OH)₂ cathode for battery-like supercapacitor. *Chem. Eng. J.*, 403, Article number: 126325.
- Liu, Q., Zhang, D., Yang, Y., Gu, Y., Liang, W., Chen, W., Wu, Y., Hu, L. (2025). Encapsulation of Prussian blue analogues with conductive polymers for high-performance ammonium-ion storage. *Adv. Energy Mater.*, 15, Article number: 2402863.
- Mohamed, H.M., Abo-Aly, M.M., Wahab, S.M.A, Ali, A.A.I., Mousa, M.A. (2024). Single, binary, and ternary nanocomposite electrodes of reduced graphene oxide @ polyaniline @ Co-Prussian analog for supercapacitors. *Electrochim. Acta*, 506, Article number: 145017.
- Meng, Y., Wang, K., Zhang, Y., Wei, Z. (2013). Hierarchical porous graphene / polyaniline composite film with superior rate performance for flexible supercapacitors. *Adv. Mater.*, 25, 6985-6990.
- Muniraj, V.K.A., Komaja, C.K., Shelke, M.V. (2016). RuO₂.n H₂O nanoparticles anchored on carbon nano-onions: an efficient electrode for solid state flexible electrochemical supercapacitor. *ACS Sustain Chem. Eng.*, 5, 2528-2534.
- Moyseowicz, A., Sliwak, A., Miniach, E., Gryglewicz, C.Z. (2017). Polypyrrole / iron oxide / reduced graphene oxide ternary composite as a binderless

- electrode material with high cyclic stability for supercapacitors. *Composites Part B*, 109, 23-29.
- Owusu, K.A., Qu, L., Li, J., Wang, Z., Zhao, K., Yang, C., Hercule, K.M., Lin, C., Shi, C., Wei, Q., Zhou, L. (2017). Low crystalline iron oxide hydroxide nanoparticle anode for high-performance supercapacitors. *Nat. Commun.*, 8, Article number: 14264.
- Phan, T.B., Luong, T.T., Mai, T.X., Mai, T.T.T., Pham, T.T. (2016). Effect of nanostructures graphene oxide on electrochemical activity of its composite with polyaniline titanium dioxide. *Adv. Nat. Sci. Nanosci. Nanotechnol*, 7, Article number: 015016.
- Ren, Q., Yuan, Y., Wang, S. (2022). Interfacial strategies for suppression of Mn dissolution in rechargeable battery cathode materials. *ACS Appl. Mater. Interfaces*, 14, Article number: 23022.
- Sharma, A., Lee, B.K. (2016). Integrated ternary nanocomposite of TiO₂/NiO/reduced graphene oxide as a visible light photocatalyst for efficient degradation of o-chlorophenol. *J. Environ. Manag.* 181, 563-573.
- Solonaru, A.M., Grigoras, M. (2017). Water-soluble polyaniline/graphene composites as materials for energy storage applications. *Express Polymer Letters*, 11(2), 127-139.
- Sowmiya, G., Velraj, G. (2020). Designing a ternary composite of PPy-PT/TiO₂ using TiO₂, and multipart-conducting polymers for supercapacitor applications. *J. Mater. Sci. Mater. Electronics*, 31, 14287-14294.
- Song, C., Yun, J., Keum, K., Ra, Y., Park, H., Lee, H., Lee, G., Yun, S., Seok, J. (2019). High performance wire-type supercapacitor with PPy/CNT-ionic liquid/AuNP/carbon nanofiber electrode and ionic liquid based electrolyte. *Carbon N.Y.*, 144, 639-648.
- Thakur, A.K., Choudhary, R.B., Majumder, M., Majhi, M. (2018). Fairly improved pseudocapacitive of PTP/PANI/TiO₂ nanohybrid composite electrode material for supercapacitor applications. *Ionics*, 24, 257-268.
- Wang, Y., Tang, S., Vongehr, S., Ali Syed, J., Wang, X., Meng, X. (2016). High-performance flexible solid-state carbon cloth supercapacitors based on highly processable N-Graphene doped polyacrylic acid / polyaniline composites, *Scientific Reports*, 6, Article number: 12883.
- Wang, H., Guo, Z., Yao, S., Li, Z., Zhang, W. (2017). Design and synthesis of ternary graphene / polyaniline / Co₃O₄ hierarchical nanocomposites for supercapacitors. *Int. J. Electrochem. Sci.*, 12, 3721-3731.

- Wang, Y., Shi, Z.Q., Huang, Y., Ma, Y.F., Wang, C.Y., Chen, M.M., Chen, Y.S. (2009). Supercapacitor devices based on graphene materials, *J. Phys. Chem. C.*, 113(30), 13103-13107.
- Xu, F., Jamal, R., Ubul, A., Shao, W., Andiryim, T. (2013). Characterization and electrochemical properties of poly(aniline-co-o-methoxy aniline)/multi-walled carbon nanotubes composites synthesized by solid-state method. *Fiber Polym.*, 14, 8-15.
- Viswanathan, A., Sheety, A.N. (2017). Facile in-situ single step chemical synthesis of reduced graphene oxide-copper oxide-polyaniline nanocomposite and its electrochemical performance for supercapacitor application. *Electrochim. Acta*, 257, 483-493.

On the Study of Parabolas in the Maximum Plane

Süheyla EKMEKÇİ¹

1- Prof. Dr.; Eskişehir Osmangazi University, Department of Mathematics and Computer Science, Faculty of Science, sekmekci@ogu.edu.tr ORCID No: 0000-0003-2820-2096

ABSTRACT

This study provides a detailed study of parabolas, called M-parabolas, in the maximum plane \mathbb{R}_M^2 (or Chebyshev plane) defined by the maximum metric. The properties and geometric structures of M-parabolas are systematically studied, characterized, and presented according to the types of their directrices. It is observed that M-parabolas are piecewise-linear structures consisting of line segments and rays determined by the properties of the metric. A fundamental property is presented that in M-parabolas, the d_M -length of the latus rectum is always four times the focal d_M -length, for all directrix types. Based on these studies, an algorithm is introduced that provides a practical visualization tool for constructing any M-parabola. Furthermore, degenerate cases where the focus lies on the directrix are examined, and the resulting degenerate M-parabolas are classified.

Keywords – Maximum metric; Chebyshev plane; parabola; latus rectum.

INTRODUCTION

Distance in the real plane and space can be quantified using various metrics, the most common being the Euclidean, taxicab, and maximum, Chinese Checker metrics. These metrics define non-Euclidean analytical planes and spaces, a subject explored in numerous studies. Some notable contributions include: (Akça and Kaya, 1997:151), (Özcan et al, 2002: 381), (Akça and Kaya, 2004:521), (Akça and Kaya, 2004:491), (Bayar and Kaya, 2005:41), (Bayar et. al., 2009:17), (Bayar and Ekmekçi, 2014: 33), (Bayar and Ekmekçi, 2015: 58), (Akça and Çalış, 2021:175), (Bayar, 2008:45), (Can et. al., 2021:95), (Gelişgen and Kaya, 2008:187), (Gelişgen and Kaya, 2015:82). The Minkowski distance (or Minkowski metric), introduced by the German mathematician Hermann Minkowski and named after him, is a family of distances that is used in many fields. This distance is also known as the L_p -norm. The Minkowski distance between the points $X = (x_1, \dots, x_n)$ and $Y = (y_1, \dots, y_n)$ is defined as:

$$d_p(X, Y) = \left(\sum_{i=1}^n |y_i - x_i|^p \right)^{\frac{1}{p}}.$$

In the case where p approaches infinity ($p \rightarrow \infty$), this distance corresponds to the maximum distance (also called Chebyshev distance, L_∞ -distance). The maximum distance is defined for points $A_1 = (x_1, y_1)$ and $A_2 = (x_2, y_2)$ as $d_M(A_1, A_2) = \max \{|x_2 - x_1|, |y_2 - y_1|\}$. This metric is particularly

useful in computer science and engineering due to its computational simplicity and intuitive application to grid-based movement and problems.

Conics represent one of the most fundamental and well-studied objects in Euclidean geometry. Conics, studied since ancient Greek times, have not only become a fundamental topic in geometry but also have significant applications in many branches of science, including astronomy, physics, engineering, and optimization. Conics, which are defined as the locus of points satisfying certain distance-based definitions in Euclidean geometry, possess rich geometric and algebraic properties. Investigating how these definitions behave under alternative metrics such as taxicab, Chinese checker, maximum, and generalized taxicab metrics has therefore become a fruitful research area. In particular, analyses of conics through two-foci and focus-directrix definitions have been extended to non-Euclidean planes induced by these metrics, leading to a variety of novel shapes and special cases (Kaya et al, 2000:135), (Laatsch, 1982:205), (Salihova, 2006:64), (Turan and Özcan, 2006:393), (Turan and Özcan, 2004:119) and (Turan and Özcan, 2004), (Altıntaş and Ekmekçi, 2025). Salihova studied the basic geometric concepts, the isometries, and the conics in the maximum plane in 2006. She introduced the general equation of M-parabolas and provided a basic framework, (Salihova, 2006:64). The primary objective of this study is to conduct a systematic classification and in-depth geometric analysis of parabolas in the maximum plane, commonly referred to as the Chebyshev Plane. Within this framework, the structure of M-parabolas is classified based on directrix type (vertical, horizontal, steep, gradual, or separator), and their geometric components are rigorously determined. Fundamental properties—including the vertex, axis, focal length, latus rectum, and symmetry—are derived and formally proven. An important finding of this work is the demonstration of a universal property: the length of the latus rectum is invariably four times the focal length, a rule that is shown to persist within the piecewise-linear structure of M-parabolas, thereby mirroring a key characteristic of their Euclidean counterparts. Additionally, degenerate cases, where the focus lies on the directrix, are investigated and classified. To facilitate practical engagement with these theoretical constructs, a general construction algorithm applicable to all directrix types is provided, enabling visualization without prior analytical computation.

PRELIMINARIES

In this section, some definitions, concepts and theorems used throughout this work are mentioned.

Definition 2.1. The maximum distance between two points $A = (a_1, a_2)$ and $B = (b_1, b_2)$ in the analytical plane is $d_M(A, B) = \max \{|a_1 - b_1|, |a_2 - b_2|\}$.

By Definition 2.1, it is clear that the maximum distance between these points is equal to the greatest of the lengths of the line segments parallel to the coordinates axes in the right triangle with the hypotenuse AB . The maximum plane (also known as Chebyshev plane) is the analytical plane equipped with the maximum distance d_M and symbolized by \mathbb{R}_M^2 .

Theorem 2.2. Let a point $P(x_0, y_0)$ be given in the maximum plane. The maximum distance from the point P to the line d with the equation $ax + by + c = 0$ is

$$d_M(P, d) = \frac{|ax_0 + by_0 + c|}{|a| + |b|},$$

where $a, b, c \in \mathbb{R}$ and $a^2 + b^2 \neq 0$, (Salihova, 2006:76).

Krause classified lines depending on their slope as the following definition:

Definition 2.3. Let m be the slope of the line l . The line l is referred to as *the steep line*, *the gradual line* and *the separator line* in the cases where $|m| > 1$, $|m| < 1$ and $|m| = 1$, respectively. In the special cases that the line l is parallel to x-axis or y-axis, it is called *the horizontal line* or *the vertical line*, respectively, (Krause, 1975:31).

Throughout this study, Krause's classification will be utilized as a fundamental tool in examining the geometric properties in the maximum plane.

Theorem 2.4. All translations of the Euclidean plane are isometries in the maximum plane, (Salihova, 2006:55).

Theorem 2.5. The reflections in the lines of the set $\{x = 0, y = 0, y = x, y = -x\}$ are isometries in the maximum plane, (Salihova, 2006:55).

Theorem 2.6. The rotations by θ -angle in the set $\left\{ \theta \mid \theta = k \frac{\pi}{2}, k = 0, 1, 2, 3 \right\}$ are isometries in the maximum plane, (Salihova, 2006:55).

PARABOLAS IN MAXIMUM PLANE

In Euclidean geometry, a parabola is defined as the set of points equidistant from a given point and a given line. The given (fixed) point is called the *focus* of the parabola, and the given line is called the *directrix* of the parabola. This section extends this fundamental concept to the maximum

plane, where parabolas are reconstructed using the maximum distance, followed by a systematic analysis of their geometric properties.

Definition 3.1. In \mathbb{R}_M^2 , let $P = (p_1, p_2)$ and d be given as a fixed point and a fixed line with the equation $ax + by + c = 0$, where $a, b, c \in \mathbb{R}$ and $a^2 + b^2 \neq 0$. The set of points at equal maximum distance from the point P and the line d is called parabola in maximum plane and it is denoted by M-parabola. Here, given the point P and the line d is referred to as *the focus* and *the directrix* of M-parabola, (Salihova, 2006:136).

It is seen from definition 3.1 that the M-parabola with the focus P and directrix d is the set

$$\{X : d_M(X, P) = d_M(X, d)\}.$$

That is, its equation is

$$\max\{|x - p_1|, |y - p_2|\} = \frac{|ax + by + c|}{|a| + |b|}. \quad (1)$$

Definition 3.2. Let the line d and the point P be the directrix and the focus of the M-parabola, respectively. Depending on whether the directrix d is of separator, steep, or gradual type; vertical type; or horizontal type, *the vertex* V of the M-parabola is defined as the point lying on the separator line with the opposite signed slope of d ; horizontal line; or vertical line through the focus P , respectively, and satisfying the condition

$$d_M(V, P) = \frac{1}{2} d_M(P, d).$$

The axis ℓ of an M-parabola is defined as the line VP passing through its vertex and its focus. Also, the focal d_M -length of an M-parabola is the d_M distance between the vertex and the focus, measured along the axis.

In \mathbb{R}_M^2 , analogous definitions for chords, focal chords, and the latus rectum of M-parabolas are established as below.

Definition 3.3. In \mathbb{R}_M^2 , a *chord* of an M-parabola is a line segment whose endpoints are on the M-parabola. A chord that passes through the focus of an M-parabola is termed a focal chord. Among these, the specific focal chord that is parallel to the directrix of an M-parabola is designated as *the latus rectum*.

A fundamental property of parabolas in the Euclidean plane is that the latus rectum length is invariably four times the focal length. This study

investigates whether this property extends to M-parabolas defined in the maximum plane.

Theorem 3.4. Let the points P and P' be on opposite half-planes with respect to the line d in \mathbb{R}_M^2 . If the d_M distance of these points to the line are equal, then the rotation π -angle at the midpoint of the points P and P' transforms the M-parabola with focus P and the directrix d to the M-parabola is determined by the focus P' and the directrix d , and vice versa.

Proof. Let d be the line with the equation $ax+by+c=0$, where $a, b, c \in \mathbb{R}$ and $a^2+b^2 \neq 0$ and, let the points $P=(p_1, p_2)$ and $P'=(p'_1, p'_2)$ be on opposite half-planes with respect to the line d in the \mathbb{R}_M^2 . Then assume that $ap_1+bp_2+c > 0$, $ap'_1+bp'_2+c < 0$. Since the d_M distance of these points to the line d are equal, then $|ap_1+bp_2+c| = |ap'_1+bp'_2+c|$. Let φ be the rotation π -angle at the midpoint of the points P and P' . The map φ leaves the midpoint fixed, while the points P and P' transform into each other under φ . It is known that the point X on the M-parabola with focus P and the directrix d holds the equality

$$d_M(X, P) = d_M(X, d).$$

Since the map φ is an isometry, it is satisfied that

$$d_M(X, P) = d_M(\varphi(X), \varphi(P)) = d_M(X', P')$$

where $\varphi(X) = \varphi(x, y) = (-x + p_1 + p'_1, -y + p_2 + p'_2) = (x', y') = X'$.

From the definition of φ , the right-hand side of the equality

$$d_M(X, d) = \frac{|ax+by+c|}{|a|+|b|}$$

is written as

$$\frac{|ax+by+c|}{|a|+|b|} = \frac{|ax'+by'+c|}{|a|+|b|}.$$

Thus, it is clear that

$$d_M(X, d) = d_M(X', d).$$

And, it is observed that by applying the map φ to the M-parabola with focus P and the directrix d to the M-parabola is determined by the focus P' and the directrix d is immediately obtained. Conversely, the proof is similar.

Based on this theorem, when examining an M-parabola, it is sufficient to assume the focus on one of the half-planes determined by the directrix. This simplifies the analysis and does not affect the generality of the results.

The theorems that follow analyze the structures of M-parabolas based on the types of their directrices and explore some geometric properties of

them. The first theorem focuses on characterizing the geometric structures of M-parabolas whose directrices are vertical.

Theorem 3.5. The M-parabola with vertical directrix is formed by the vertical line segments and two rays on different nonparallel separator lines. Also, the axis of the M-parabola is the horizontal line at the focus and it is symmetric about its axis.

Proof. Let an M-parabola be defined by the focus $P = (p_1, p_2)$ and the vertical directrix d with the equation $ax + c = 0$, where $a, c \in \mathbb{R}$ and $a \neq 0$. Assume that $ap_1 + c > 0$. The points of the M-parabola satisfy the equation

$$\max \{|x - p_1|, |y - p_2|\} = x + \frac{c}{a}. \quad (2)$$

And from (2), it follows that the M-parabola is formed by the union of the vertical line segment

$$l_1 : x = \frac{p_1}{2} - \frac{c}{2a}, -\left(\frac{p_1}{2} + \frac{c}{2a}\right) + p_2 \leq y \leq \left(\frac{p_1}{2} + \frac{c}{2a}\right) + p_2,$$

and two rays

$$r_1 : y - p_2 = -\left(x + \frac{c}{a}\right), y \leq -\left(\frac{p_1}{2} + \frac{c}{2a}\right) + p_2,$$

$$r_2 : y - p_2 = x + \frac{c}{a}, y \geq \frac{p_1}{2} + \frac{c}{2a} + p_2.$$

It is seen that the rays are on two different separator lines and line segment is parallel to directrix. The M-parabola is opening to the right (the positive direction relative to the x-axis). The shortest distance d_M from the point P to the directrix d is attained along the horizontal line passing through P . This horizontal line meets the directrix at the point $\left(-\frac{c}{a}, p_2\right)$. From

Definition 3.2, the midpoint $\left(\frac{ap_1 - c}{2a}, p_2\right)$ of the points $\left(-\frac{c}{a}, p_2\right)$ and P is the vertex V of the M-parabola. And, its axis ℓ is the horizontal line passing through the vertex and the focus P . The latus rectum of the M-parabola is the line segment

$$x = p_1, -\left(p_1 + \frac{c}{a}\right) + p_2 \leq y \leq \left(p_1 + \frac{c}{a}\right) + p_2.$$

The d_M -length of the latus rectum is $2\left(p_1 + \frac{c}{a}\right)$ and its focal d_M -length is the value $\frac{1}{2}\left(p_1 + \frac{c}{a}\right)$. Then, it is clear that the d_M -length of the latus rectum

is four times the focal d_M -length for this case. Let φ be the reflection in the

axis such that φ transforms the point (x, y) to the point $(x, -y + 2p_2)$. Since the reflection φ leaves the line segment l_1 in M-parabola fixed and maps the rays r_1 and r_2 into each other, the M-parabola is symmetric about its axis, (Fig.1). Also, it is noted that if the rays are extended to lines, they intersect at intersection point $\left(-\frac{c}{a}, p_2\right)$. If the focus is in the other half plane ($ap_1 + c < 0$), the result is clear from Theorem 3.4.

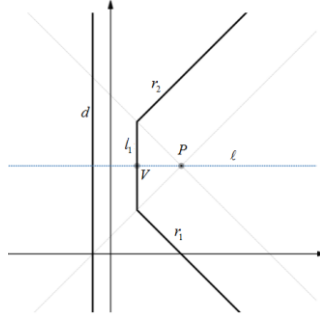


Figure 1. The M-parabolas with vertical directrix

When the directrix of the M-parabola is a horizontal line, the union of the line segment

$$l_1 : y = \frac{p_2}{2} - \frac{c}{2b}, |y - p_2| \leq \frac{p_2}{2} + \frac{c}{2b}$$

and two rays

$$|x - p_1| = y + \frac{c}{b}, y \geq \frac{p_2}{2} - \frac{c}{2b}.$$

The line segments and rays possess the specified properties in the vertical case. The vertex V and the axis ℓ of the M-parabola are $\left(p_1, \frac{bp_2 - c}{2b}\right)$ and the vertical line passing through the vertex and the focus P , respectively. M-parabola is opening to the top. Its latus rectum is the line segment

$$y = p_2, |x - p_1| \leq p_2 + \frac{c}{b}$$

and d_M -length of the latus rectum is $2\left(p_2 + \frac{c}{b}\right)$. Since its focal d_M -length is the value $\frac{1}{2}\left(p_2 + \frac{c}{b}\right)$, it is obvious that the d_M -length of the latus rectum is four times the focal d_M -length for horizontal-directrix case.

The following theorem examines M-parabolas whose directrix is a steep line.

Theorem 3.6. The M-parabola with a steep directrix is formed by two line segments and two rays such that one of the line segments is of the steep type, the other is of the gradual type, and the rays are on the separator lines parallel to its axis.

Proof. Let an M-parabola be defined by the focus $P = (p_1, p_2)$ and the steep directrix d with the equation $ax + by + c = 0$, where $a, b, c \in \mathbb{R}$ and $a^2 + b^2 \neq 0$. The points of the M-parabola satisfy the equation

$$\max \{|x - p_1|, |y - p_2|\} = \frac{|ax + by + c|}{|a| + |b|}. \quad (3)$$

Since d is the steep line, $a \neq 0$ and there is no loss of generality when $a = 1$ is taken. Then, $|b| < 1$. Assume that $p_1 + bp_2 + c > 0$. The equation (3) reduces to the equation

$$\max \{|x - p_1|, |y - p_2|\} = \frac{x + by + c}{1 + |b|}. \quad (4)$$

One can immediately deduce from the last equality that the M-parabola consists of the line segments and rays given by the following equations:

$$(2 + |b|)x + by + c - (1 + |b|)p_1 = 0, \quad (5)$$

$$|b|x - by - c - (1 + |b|)p_1 = 0, \quad (6)$$

$$x + (1 + b + |b|)y + c - (1 + |b|)p_2 = 0, \quad (7)$$

$$x + (-1 + b - |b|)y + c + (1 + |b|)p_2 = 0. \quad (8)$$

In case that the directrix d has a negative slope, the M-parabola is formed by the steep line segment with the equation (5) where $\frac{(1 - b + |b|)p_1 - bp_2 - c}{(2 - b + |b|)} \leq x \leq \frac{(1 + b + |b|)p_1 - bp_2 - c}{(2 + b + |b|)}$, the gradual line segment

with the equation (7) where

$\frac{(1 + b + |b|)p_1 - bp_2 - c}{(2 + b + |b|)} \leq x \leq \frac{(1 + b + |b|)p_1 + bp_2 + c}{b + |b|}$, the ray with the equation

(6) where $\frac{(1 + b + |b|)p_1 + bp_2 + c}{b + |b|} \leq x$ and the ray with the equation (8) where

$\frac{(1 - b + |b|)p_1 - bp_2 - c}{(2 - b + |b|)} \leq x$, (Fig. 2.a). Similarly, in case that the directrix d

has a positive slope, the M-parabola is formed by the steep line segment with the equation (5) where $\frac{(1 + b + |b|)p_1 - bp_2 - c}{(2 + b + |b|)} \leq x \leq \frac{(1 - b + |b|)p_1 - bp_2 - c}{(2 - b + |b|)}$, the gradual line segment with the equation (8) where

$\frac{(-1+b-|b|)p_1+bp_2+c}{(-2+b-|b|)} \leq x \leq \frac{(-1+b-|b|)p_1-bp_2-c}{b-|b|}$, the ray with the

equation (6) where $\frac{(1-b+|b|)p_1+bp_2+c}{-b+|b|} \leq x$ and the ray with the equation

(7) where $\frac{(1+b+|b|)p_1-bp_2-c}{(2+b+|b|)} \leq x$, (Fig. 2.b). It is clear that the rays are on

two parallel separator lines. The shortest maximum distance between the focus and the directrix d is measured along the separator line with the opposite signed slope of d and passing through P . Since the vertex V is on this line, the coordinates of V is

$$\left(\frac{(1+b+|b|)p_1-bp_2-c}{2+b+|b|}, \frac{-p_1+(2+|b|)p_2-c}{2+b+|b|} \right)$$

or

$$\left(\frac{(-1+b-|b|)p_1+bp_2+c}{-2+b-|b|}, \frac{-p_1-(2+|b|)p_2-c}{-2+b-|b|} \right)$$

depending on whether the slope of the directrix d is negative or positive, respectively. And its axis ℓ is the separator line PV . Its latus rectum is the line segment

$$x+by=p_1+bp_2, |x-p_1| \leq \frac{|b|}{1+|b|} (p_1+bp_2+c)$$

and its d_M -length is $\frac{2}{1+|b|} |p_1+bp_2+c|$.

The focal d_M -length is equal to the value of $\frac{|p_1+bp_2+c|}{|2+b+|b||}$ or $\frac{|p_1+bp_2+c|}{|-2+b-|b||}$,

depending on whether the slope of the directrix d is negative or positive, respectively. Then, it is clear that the d_M -length of the latus rectum is four times the focal d_M -length for steep-directrix case.

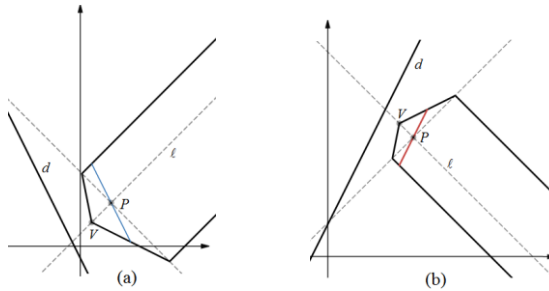


Figure 2. The M-parabolas with steep directrices

In the following theorem, M-parabolas whose directrices are the gradual lines are characterized.

Theorem 3.7. The M-parabola with a gradual directrix is formed by two line segments and two rays such that one of the line segments is of the steep type, the other is of the gradual type, and the rays are on the separator lines parallel to its axis.

Proof. Let an M-parabola be defined by the focus $P=(p_1, p_2)$ and the gradual directrix d with the equation $ax+by+c=0$, where $a, b, c \in \mathbb{R}$ and $a^2+b^2 \neq 0$. Since d is the gradual line, $b \neq 0$ and there is no loss of generality when $b=1$ is taken. Then, $|a| < 1$. Assume that $ap_1 + p_2 + c > 0$. Thus, the equation (3) reduces to the equation

$$\max \{|x - p_1|, |y - p_2|\} = \frac{ax + y + c}{|a| + 1}. \quad (9)$$

One can immediately deduce from the last equality that the M-parabola consists of the line segments and rays given by the following equations:

$$(1+a+|a|)x + y + c - (1+|a|)p_1 = 0, \quad (10)$$

$$(-1+a-|a|)x + y + c + (1+|a|)p_1 = 0. \quad (11)$$

$$ax + (2+|a|)y + c - (1+|a|)p_2 = 0, \quad (12)$$

$$ax - |a|y + c + (1+|a|)p_2 = 0, \quad (13)$$

In case that the directrix d has a negative slope, the M-parabola is formed by the steep line segment with the equation (10) where $\frac{-ap_1 + (1+a+|a|)p_2 - c}{2+a+|a|} \leq y \leq \frac{ap_1 + (1+a+|a|)p_2 + c}{a+|a|}$, the gradual line segment

with the equation (12) where

$\frac{-ap_1 + (1-a+|a|)p_2 - c}{2-a+|a|} \leq y \leq \frac{-ap_1 + (1+a+|a|)p_2 - c}{2+a+|a|}$, the ray with the

equation (11) where $\frac{-ap_1 + (1-a+|a|)p_2 - c}{2-a+|a|} \leq y$ and the ray with the

equation (13) where $\frac{ap_1 + (1+a+|a|)p_2 + c}{a+|a|} \leq y$, (Fig. 5.a). Similarly, in case

that the directrix d has a positive slope, the M-parabola is formed by the steep line segment with the equation (11) where

$\frac{-ap_1 + (1-a+|a|)p_2 - c}{2-a+|a|} \leq y \leq \frac{ap_1 + (1-a+|a|)p_2 + c}{-a+|a|}$, the gradual line segment

with the equation (12) where

$\frac{-ap_1 + (1+a+|a|)p_2 - c}{2+a+|a|} \leq y \leq \frac{-ap_1 + (1-a+|a|)p_2 - c}{2-a+|a|}$, the ray with the equation (10) where $\frac{-ap_1 + (1+a+|a|)p_2 - c}{2+a+|a|} \leq y$ and the ray with the equation (13) where $\frac{ap_1 + (1-a+|a|)p_2 + c}{-a+|a|} \leq y$, (Fig. 5.b). It is clear that the rays are on two parallel separator lines. The vertex V is the point $\left(\frac{(2+|a|)p_1 - p_2 - c}{2+a+|a|}, \frac{-ap_1 + (1+a+|a|)p_2 - c}{2+a+|a|} \right)$ or the point $\left(\frac{(2+|a|)p_1 + p_2 + c}{2-a+|a|}, \frac{-ap_1 + (1-a+|a|)p_2 - c}{2-a+|a|} \right)$ depending on whether the slope of the directrix d is negative or positive, respectively. And its axis ℓ is the separator line PV such that the signs of the slopes of the lines ℓ and d are opposite. Subsequently, the latus rectum of the M-parabola is the line segment

$$ax + y = ap_1 + p_2, |y - p_2| \leq \frac{|a|}{1+|a|} (ap_1 + p_2 + c)$$

and its d_M -length is $\frac{2}{1+|a|} |ap_1 + p_2 + c|$. The focal d_M -length is equal to the value $\frac{|ap_1 + p_2 + c|}{|2+a+|a||}$ or $\frac{|ap_1 + p_2 + c|}{|2-a+|a||}$, depending on whether the slope of the directrix d is negative or positive, respectively. Thus, it is proven that the d_M -length of the latus rectum is four times the focal d_M -length for steep-directrix case.

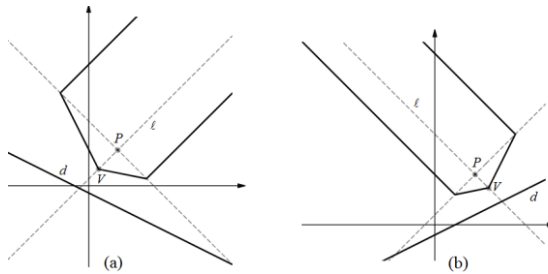


Figure 5. The M-parabolas with gradual directrices

In the next theorem, M-parabolas are discussed when the directrix is a separator line.

Theorem 3.8. The M-parabola whose directrix is a separator line is formed by two line segments and two rays such that one of the line segments is of the steep type, the other is of the gradual type, and the rays are on the separator lines parallel to its axis. Also, it is symmetric about its axis.

Proof. Let an M-parabola be defined by the focus $P=(p_1, p_2)$ and the separator directrix d with the equation $x+y+c=0$, where $c \in \mathbb{R}$. Assume that $p_1 + p_2 + c > 0$. Then, the equation (3) reduces to the equation

$$\max \{|x-p_1|, |y-p_2|\} = \frac{x+y+c}{2}. \quad (14)$$

Solving (14) reveals that the M-parabola consists of the line segments and rays given by the following equations:

$$3x+y+c-2p_1=0, \quad (15)$$

$$-x+y+c+2p_1=0, \quad (16)$$

$$x+3y+c-2p_2=0, \quad (17)$$

$$x-y+c+2p_2=0, \quad (18)$$

More clearly, the M-parabola whose the directrix d is a separator line with negative slope is formed by the steep line segment with the equation (15) where $\frac{-p_1+3p_2-c}{4} \leq y \leq \frac{p_1+3p_2+c}{2}$, the gradual line segment with the equation (17) where $\frac{-p_1+p_2-c}{2} \leq y \leq \frac{-p_1+3p_2-c}{4}$, the ray with the equation (16) where $\frac{-p_1+p_2-c}{2} \leq y$ and the ray with the equation (18) where $\frac{p_1+3p_2+c}{2} \leq y$. Its vertex V and its axis ℓ are the point $\left(\frac{3p_1-p_2-c}{4}, \frac{-p_1+3p_2-c}{4}\right)$ and the separator line with the positive slope and passing through P , respectively, (Fig. 6). The latus rectum of the M-parabola is the line segment

$$x+y=p_1+p_2, |y-p_2| \leq \frac{p_1+p_2+c}{2}$$

and its d_M -length is $|p_1+p_2+c|$. The focal d_M -length is equal to the value $\frac{|p_1+p_2+c|}{4}$. From here, it can be seen that the d_M -length of the latus

rectum is equal to four times the focal d_M -length. Let φ be the reflection in the axis ℓ such that φ transforms the point (x, y) to the point $(y-p_2+p_1, x-p_1+p_2)$. Since the reflection φ leaves the points P, V fixed

and maps line segments into each other and rays into each other, the M-parabola is symmetric about its axis ℓ .

Similarly, in case that the directrix d is a separator line $x - y + c = 0$,

By rearranging (14), it is implied that the locus consists of line segments and rays specified by the following equations:

$$3x - y + c - 2p_1 = 0, \quad (19)$$

$$-x - y + c + 2p_1 = 0, \quad (20)$$

$$x + y + c - 2p_2 = 0, \quad (21)$$

$$x - 3y + c + 2p_2 = 0. \quad (22)$$

To be more explicit, the M-parabola consists of the steep line segment with the equation (19) where $\frac{-p_1 + 3p_2 - c}{2} \leq y \leq \frac{p_1 + 3p_2 + c}{4}$; the gradual line

segment with the equation (22) where $\frac{p_1 + 3p_2 + c}{4} \leq y \leq \frac{p_1 + p_2 + c}{2}$; the ray

with the equation (20) where $y \leq \frac{p_1 + p_2 + c}{2}$ and the ray with the equation

(21) where $y \leq \frac{-p_1 + 3p_2 - c}{2}$. It is apparent that the rays are on two parallel

separator lines. Its vertex V and its axis ℓ are the point $\left(\frac{3p_1 + p_2 - c}{4}, \frac{p_1 + 3p_2 + c}{4}\right)$ and the separator line with the negative slope and passing through P , respectively. The latus rectum is the line segment

$$x - y = p_1 - p_2, |y - p_2| \leq \frac{p_1 - p_2 + c}{2}$$

and its d_M -length is $|p_1 - p_2 + c|$. The focal d_M -length is equal to the value $\frac{|p_1 - p_2 + c|}{4}$. This demonstrates that the d_M -length of the latus rectum is

equal to four times the focal d_M -length. If the map φ is the reflection in the axis ℓ such that φ transforms the point (x, y) to the point $(-y + p_1 + p_2, -x + p_1 + p_2)$, then $\varphi(V) = V$, $\varphi(P) = P$, and φ maps line segments into each other and rays into each other. So, the M-parabola is symmetric about its axis.

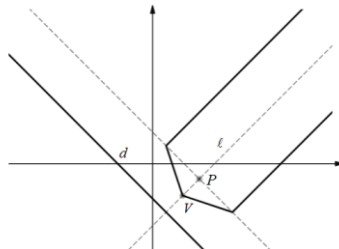


Figure 6. The M-parabola with a separator directrix

Furthermore, the aforementioned theorems yield immediately following corollary:

Corollary 3.9. The latus rectum length of any M-parabola measures four times the focal length, a property that holds independent of the directrix types.

An algorithm for the construction of the M-parabola with the focus P and the directrix d is presented in the following. This method is applicable to all directrix types and is without analysis in its approach.

- 1) The Separator lines passing through the focus are drawn.
- 2) The intersection point of the lines d and d' is found where the line d' is determined according to the type of the directrix d as follows:
 - If the directrix d belongs to either steep, gradual, or separator types,
 - (i) When the slope of d is positive, d' is the separator line with negative slope through P ;
 - (ii) When the slope of d is negative, d' is the separator line with positive slope through P .
 - If the directrix d is a vertical line, d' is the horizontal line through P .
 - If the directrix d is a horizontal line, d' is the vertical line through P .
- 3) The vertex of the M-parabola is determined by finding the midpoint of the intersection point in (2) and the focus.
- 4) The points T_1 and T_2 are:
 - a) the points that the vertical line through the vertex V intersects the lines in (1), when d is a vertical line.
 - b) the points that the horizontal line through the vertex V intersects the lines in (1), when d is a horizontal line.
 - c) the points that the lines through the vertex V with slopes $-\frac{(2+|\lambda|)}{\lambda}$ and $-\frac{1}{1+\lambda+|\lambda|}$ (or $-\frac{1}{1-\lambda+|\lambda|}$) intersect the line not passing through V stated in (1), depending on whether the steep directrix d with the equation $x+\lambda y+c=0$, $\lambda, c \in \mathbb{R}$, $|\lambda|<1$, has a negative or a positive slope, respectively.
 - d) the points that the lines through the vertex V with slopes $-\frac{\lambda}{2+|\lambda|}$ and $-(1+\lambda+|\lambda|)$ (or $-(1-\lambda+|\lambda|)$) intersect the line not passing through V stated in (1), depending on whether the gradual directrix d with the equation

$\lambda x + y + c = 0$, $\lambda, c \in \mathbb{R}$, $|\lambda| < 1$, has a negative or a positive slope, respectively.

e) the points that the lines through the vertex V with slopes $-\frac{1}{3}, -3$ (or $\frac{1}{3}, 3$) intersects the line in (1) not passing through V , depending on whether the separator directrix d is given by the equation $x + y + c = 0$ or $x - y + c = 0$, $c \in \mathbb{R}$.

5) The rays r_1 and r_2 are:

a) parallel to the lines specified in (1), with initial points T_1 and T_2 , non-intersecting the directrix, when the directrix d is a vertical line or a horizontal line.

b) parallel to the line (axis) joining the vertex and the focus, with initial points T_1 and T_2 , non-intersecting the directrix, when the directrix d is one of a separator line, a steep line or a gradual line.

6) The M-parabola is

a) the union of the line segment T_1T_2 (since the points T_1 , T_2 and V are collinear, the line segments VT_1 and VT_2 constitute the line segment T_1T_2), and the rays r_1 and r_2 when the directrix d is a vertical line or a horizontal line.

b) the union of the line segments VT_1 and VT_2 and the rays r_1 and r_2 for other types of directrix.

Up to this point, M-parabolas have been examined under the assumption that the focus is not on the directrix. The case where the focus lies on the directrix is now considered. If the focus is on the directrix, the locus is defined as a *degenerate M-parabola*. These degenerate M-parabolas are likewise classified based on the directrix types as follows:

Theorem 3.10. Let a degenerate M-parabola be defined by a focus P and a directrix d . Then, based on the type of the directrix d , its geometric structure is as follows:

i) If the directrix d is either a vertical line or a horizontal line, then degenerate M-parabola is the union of two planar regions, determined by the separator lines through P , which does not include the directrix d except at the point P .

ii) If the directrix d is either of steep, gradual or separator types, then the degenerate M-parabola is the separator line with the opposite signed slope of d and passing through P .

Proof. Let a degenerate M-parabola be defined by the focus $P = (p_1, p_2)$ and the gradual directrix d with the equation $ax + y + c = 0$, where $a, c \in \mathbb{R}$ and $|a| < 1$. The degenerate M-parabola is the set of points that satisfy the equation

$$\max \{|x - p_1|, |y - p_2|\} = \frac{|ax + y + c|}{|a| + 1}. \quad (23)$$

Substituting the equality $ap_1 + p_2 + c = 0$ into (23) and analyzing the result, it is seen that the points of degenerate M-parabola form the separator line through P , (Fig 7.a). If $0 < a < 1$, then the degenerate M-parabola is the separator line $x - y = p_1 - p_2$. If $-1 < a < 0$, then it is the separator line $x + y = p_1 + p_2$. When the directrix d is the horizontal line given by the equation $y + c = 0$, where $c \in \mathbb{R}$, taking $a = 0$ and applying the analysis above, one gets easily that the degenerate M-parabola is the region specified by the inequality $|x - p_1| \leq |y - p_2|$. When the case of the steep directrix d with the equation $x + by + c = 0$, where $b, c \in \mathbb{R}$ and $|b| < 1$ is examined similarly, it is evident that the degenerate M-parabola is the separator line $x - y = p_1 - p_2$ when $0 < b < 1$ or the separator line $x + y = p_1 + p_2$ when $-1 < b < 0$, (Fig 7.b). For the case of the vertical directrix d with the equation $x + c = 0$, where $c \in \mathbb{R}$, one gets easily that the degenerate M-parabola is the region specified by the inequality $|x - p_1| \geq |y - p_2|$, (Fig 7.c). When the directrix d is a separator line with negative slope, for the parabola, the equality

$$\max \{|x - p_1|, |y - p_2|\} = \frac{|x + y + c|}{2} \quad (24)$$

is valid where $c \in \mathbb{R}$. By substituting the equality $p_1 + p_2 + c = 0$ into (24), it is observed that the locus is the separator line $x - y = p_1 - p_2$. It is similarly seen that the degenerate M-parabola is the separator line $x + y = p_1 + p_2$ when the directrix d is taken as a separator line with positive slope.

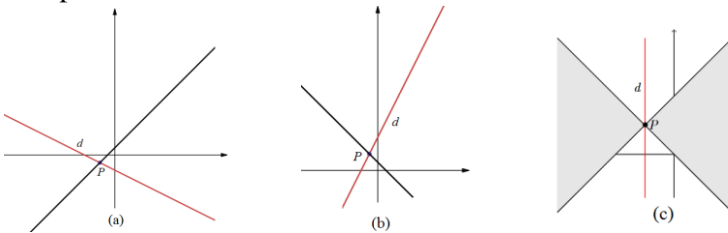


Figure 7. The degenerate M-parabolas

CONCLUSION

This study extends the existing literature on parabolas in the maximum plane (M-parabolas) and provides a thorough geometric analysis. Salihova (2006) introduced the basic definition and general equation of conics in the maximum plane. In this study, the structure of M-parabolas is fully characterized based on the type of their directrix (vertical, horizontal, steep, gradual, separator), and piecewise-linear structures consisting of line segments and rays, expressed by exact equations for each type, are presented. A key contribution not highlighted in the existing literature is the proof of the universal rule that the length of the latus rectum is four times the focal length. This rule demonstrates that a property well-known from Euclidean parabolas is preserved invariantly in the piecewise-linear geometry of M-parabolas. Furthermore, degenerate M-parabolas arising when the focus and directrix coincide are classified and their geometric behavior is described. Another novel contribution is the provision of a general construction algorithm applicable to all directrix types, which requires no analytical computation and enables practical visualization of these theoretical curves. In conclusion, this study fills the existing gaps in the literature by systematically classifying M-parabolas, rigorously establishing their properties, and providing a practical algorithm. These findings are expected to contribute to the understanding of conics in non-Euclidean geometries and to form a foundation for future studies.

REFERENCES

- Akça, Z. and Çalış, C. (2021). Voronoi diyagramı ve Taksi düzlemi üzerine. *Erzincan Üniversitesi Fen Bilimleri Enstitüsü Dergisi*, 14(1), 175–181.
- Akça, Z. and Kaya, R. (2004). On the distance formulae in three dimensional taxicab space. *Hadronic J.*, 27(5), 521–532.
- Akça, Z. and Kaya, R. (1997). On the taxicab trigonometry. *J. of Inst. Math. Comput. Sci. Math. Ser.*, 10(3), 151–159.
- Akça, Z. and Kaya, R. (2004). On the norm in higher dimensional taxicab spaces. *Hadronic J. Suppl*, 19(4), 491–501.
- Altıntaş, A. (2009). The Application of Some Geometric Problems on Euclidean Plane Using Generalized Taxicab Metric, MSc, Eskişehir Osmangazi University, Institute of Science and Technology, Turkey.
- Altıntaş, A. and Ekmekçi, S. (2025). Parabolas in generalized taxicab plane. (submitted).
- Bayar, A. and Ekmekçi, S. (2015). On complex numbers and taxicab plane. *Mathematical Sciences and Applications E-Notes*, 3(1), 58–64.
- Bayar, A. and Ekmekçi, S. (2014). On circular inversions in taxicab plane. *Journal of Advanced Research in Pure Mathematics*, 6(4), 33–39.
- Bayar, A. (2008). On the trigonometric functions in the maximum metric. *Scientific and Professional Journal of the Croatian Society for Geometry and Graphics*, 12, 45–48.

- Bayar, A., Ekmekçi, S. and Özcan, M. (2009). On trigonometric functions and cosine and sine rules in taxicab plane. *International Electronic Journal Of Geometry*, 2(1), 17–24.
- Can, Z., Çolak, Z., Gelişgen, Ö. and Yıldırım, K. (2021). A note on some distance formulae in 3-dimensional maximum space. *Journal Of Mahani Mathematical Research Center*, 10(1), 95–102.
- Gelişgen, Ö., and Kaya, R. (2008). The taxicab space group, *Acta Mathematica Hungarica*, 122(1), 187–200.
- Gelişgen, Ö. and Rüstem, K. (2015). The isometry group of Chinese Checker space. *International Electronic Journal of Geometry*, 8(2), 82–96.
- Kaya, R., Akça, Z., Özcan, M. and Günaltılı, İ. (2000). General equation for taxicab conics and their classification. *Mitt. Math. Ges. Hamburg*, 19(0), 135–148.
- Krause, E. F. (1975). *Taxicab geometry*. Menlo Park, California: Addison –Wesley Publishing Company.
- Laatsch, R. (1982) Pyramidal sections in taxicab geometry, *Math. Mag.* 55, 205–212.
- Özcan, M., Ekmekçi, S. and Bayar, A. (2002). A note on the variation of the taxicab lengths under rotations. *The Pi Mu Epsilon Journal*, 11(7), 381–384.
- Salihova, S. (2006) On the geometry of maximum metric. Doctoral dissertation, Eskişehir Osmangazi University, Institute of Science and Technology, Turkey.
- Turan, M. and Özcan, M. (2006). General equation for Chinese Checker conics and focus-directrix Chinese Checker Conics. *International Journal of Pure and Applied Mathematics*, 393–401.
- Turan, M. and Özcan, M. (2004). Two-foci Chinese Checker ellipses. *International Journal of Pure and Applied Mathematics*, 119–127.
- Turan, M. and Özcan, M. (2004). Two-foci Chinese Checker hyperbolas. *International Journal of Pure and Applied Mathematics*, 0–0.

